Nanoscale Origins of Thermal Transport Phenomena for Hybrid Layered Perovskites

By

Nabeel S. Dahod

B.S. Chemical Engineering
The Pennsylvania State University, 2013

SUBMITTED TO THE DEPARTMENT OF CHEMICAL ENGINEERING IN PARTIAL FULFILLMENT OF THE REQUIREMENTS FOR THE DEGREE OF

DOCTOR OF PHILOSOPHY IN CHEMICAL ENGINEERING

at the
MASSACHUSETTS INSTITUTE OF TECHNOLOGY
June 2019

Signature of Author:_____

Department of Chemical Engineering
May 3rd, 2019

Certified by:_____

William A. Tisdale
ARCO Career Development Professor of Chemical Engineering
Thesis Supervisor

Accepted by: _____

Patrick S. Doyle
Robert T. Haslam Professor of Chemical Engineering
Chairman, Committee for Graduate Students

Nanoscale Origins of Thermal Transport Phenomena in Hybrid Layered Perovskites

by
Nabeel S. Dahod

Submitted to the Department of Chemical Engineering on May 3rd, 2019 in partial fulfillment of the requirements for the degree of Doctor of Philosophy in Chemical Engineering

Abstract

An exciting and fundamentally powerful modern methodology for materials development is the process by which artificial solids are rationally built piece-by-piece from nanoscale "building blocks". Among the library of nanomaterials currently at the forefront of this pursuit, two-dimensional layered lead halide perovskites (2D LHPs), are of particular interest. These materials, solid crystals composed of alternating layers of atomically thin organic and inorganic subphases, possess novel optical and electronic properties that make them particularly suited for use in devices including solar cells, LEDs, flexible electronics, and even lasers. While significant early strides have been made in investigating charge carrier transport through dynamic models and sophisticated experiments, comparatively little attention has been given to understanding the manner in which the design of these nanostructured solids impacts their macroscopic thermal properties via thermal carrier (phonon) transport. This knowledge, however, is critical to addressing the thermal management constraints necessary to the design of reliable and stable devices.

To this end, this dissertation seeks to elucidate the thermal stability and fundamental pathways for heat transport within 2D LHP artificial solids. I first present an experimental investigation into the thermal and structural stability of these 2D LHPs near room temperature using differential scanning calorimetry and x-ray diffraction. This analysis reveals near-room temperature melting transitions isolated to the organic component of the nanomaterials. The existence of such an isolated phase transition indicates the

materials behave thermophysically as composites, a hypothesis that is supported by the effective use of a lever rule in estimation of the heat capacity of the materials.

I discuss the theoretical foundation and experimental construction of a frequency domain thermoreflectance technique to effectively measure the cross-plane thermal conductivity of 2D LHPs. This technique is then utilized to perform the first measurement of the thermal conductivity of 2D LHPs. This experimental study reveals that even in terms of their thermal transport pathways, 2D LHPs can be treated as composite materials. Specifically, lead bromide 2D LHPs exhibit structure-property relationships characteristic of ballistic phonon transport within isolated subphases and diffuse scattering at the organic-inorganic interfaces between layers.

Finally, I report the first measurements of the vibrational spectrum for 2D LHPs via low frequency Raman spectroscopy. This probe identifies the persistence of bulk-like phonons even in the atomically thin 2D LHPs, in addition to identifying coherent acoustic phonons in lead iodide 2D LHPs potentially capable of carrying thermal energy across the organic-inorganic interfaces without scattering. Each of the observations made throughout this dissertation suggest the thermophysical representation of 2D LHPs as composite materials is a useful framework for understanding their thermal transport properties. That so many material properties can be effectively predicted simply from the bulk properties of the component phases is surprising given both the long-range order of the artificial solids and the sub-nanometer length scale of the individual component layers, and underlines the potential for intelligent engineering of the thermal properties of 2D LHPs without deleterious influences on the sterling optoelectronic properties.

Thesis Supervisor: William A. Tisdale
Title: Associate Professor of Chemical Engineering

Acknowledgements

As my time in graduate school has drawn to a close I have spent as much time in reflection as I have frantically finishing up my research. With this dissertation I finish a process I have been building towards for as long as I can remember. When I was a child and could barely speak, my mother and I would sit in bed and watch *The Little Engine that Could*, repeating the words "I think I can" while dreaming together, something we still do to this day when times are tough. Over the course of my studies my confidence has wavered plenty, but my ability to put just one foot forward, and then the next, has never abandoned me. I owe this doggedness to my mother. In fact, I owe all of my strength to her.

A dissertation is built, first and foremost, from the motivation of the student to do more than is asked, to push the bounds of what has been done before, to find that essential spark hidden beneath a heap of acceptable answers, and to do it all while under the weighty pall of a likely failure that would be entirely one's own. I was never that kid growing up. I never did more than was asked, in fact as an elementary school student my chief source of pride was how far I could get without doing even that much. And I choked, time and again I failed on test after test and in every big game. I am no longer that person because of my father. Watching him remain intensely calm, even while failure after failure mounted and all those around him lost composure inspires me every single day. I now set goals, like my father, almost pathologically without regard for what others want or expect for me. I set the bar higher than I can hope to hit, and when I fall short, I call it a failure and move the bar higher still. I have come to love the thrill of being so close to failure. So I thank my father, for being my hero, for teaching me what greatness looks like, and for reminding me that it is by nature always just beyond my reach.

Even with these lessons, however, graduate school is a maelstrom of emotional unpredictability. Moments of euphoria and discovery quickly give way to new seemingly unanswerable questions, most of which need to be answered for the initial euphoria to bear any reward. The darkest stretches, even with the support of friends and family, are extremely isolating moments. Research forces its devotees to find a way to stay engaged, to have faith, and maintain their self-confidence. I found my way through my wife, Farah Dahod, who feels the lows with me for the sole purpose of making them less painful while never letting me forget to enjoy the good moments.

Graduate school has shown me, in so many different ways, exactly what my bandwidth is for staying motivated, self-confident, and engaged in my work. In a roundabout way this has forced me to find a balance in life that prior to this adversity I had taken for granted. Reminding myself to eat, to forget about my work for a little while, and thus to refresh has been an

essential piece of my growth during the last 5 or so years. To this end, my brother Rayhan has been my tireless companion. Whether he would spend weekends with me just to teach me how to cook, accompanying me to events he had little interest in, or sitting next to me while I dozed off during a movie, my brother has been there to help. He was an immovable object of support during a time in my life where everything else at one point or another was in flux. But more than that he teaches me how to hope when life is at its most bleak, and he keeps me humble no matter how good I think I deserve to feel.

My decision to pursue chemical engineering has been influenced by so many supportive and engaging teachers. From my 8th grade math teacher Ms. Anna Maria Licameli, who time and again went out of her way to help feed my interest in mathematics as I first became enamored with it, to my high school chemistry teacher Ms. Betty Iannuccilli, who helped a struggling chemistry student she could easily have written off as 'doing fine', I have received guidance exactly when I most needed it. I can't thank my teachers enough, but I hope this is a start.

I cannot explain my identity as a chemical engineer without first thanking my mentor Dr. Aleks Franz. Aleks gave me my first, second, and third internships in chemical engineering and over those years taught me all of my fundamentals. But more than that, he taught me what it means to be an engineer. He taught me to seek out problems that matter, that have a real impact on the lives of others, and in solving those problems to always look for the elegance in simple solutions. He taught me the hard way to question every assumption, except of course that he was always right.

My research career began, as I have come to tell myself most do, with significant floundering during my first years as an undergraduate researcher. Fortunately, I spent that time at Penn State under the advisement of Dr. Enrique Gomez. Dr. Gomez gave me freedom at a time in my life when exploration was exactly what I needed in order to find the kind of work I really loved to do. Undergraduate research can so frequently become monotonous work, but Dr. Gomez helped me use my time in his lab to experience all the various flavors of research out there. His guidance and willingness to debate with me despite how little I knew is eternally appreciated. I also would like to thank the litany of other professors at Penn State that turned my passion for chemical engineering into an education. Professors Darrell Velegol, Michael Janik and Andrew Zydney, in particular, constantly took time out of their days to meet with me to discuss my development as a student and person. To have had the attention of each of them is more than I could have asked for. The older I get, the more grateful I become to have had their guidance.

In addition to my development as a researcher during my time at Penn State, I also found my deepest and most profound enjoyment from my time studying English literature and learning

to write. For taking on a chemical engineer as an advisee, I must in particular thank Professors Heather Corbally Bryant, Elizabeth Kadetsky, and John Ballam for their tutelage. I am and will always be a writer first, and I have all of them to thank for this occasionally miserable gift.

Before I began the research that lead to this dissertation, I was a first year student trying to pull myself through a first year of courses that was equal parts humiliating and empowering. During that time, I made friendships within my cohort that not only helped me through that semester but have sustained me ever since. Whether by commiserating with me about my latest failure or by helping me expand my scientific knowledge, these friends have been an essential component of my time here. In particular, I'd like to thank Naveed Bakh, John Barton, Steven Brown, Orpheus Chatzivasileiou, Kameron Conforti, Anton Cottrill, Andrew Fiore, Jeffrey Kowalski, Troy Langford, and Dan Salem.

Since joining the Tisdale lab, I have enjoyed the company of some truly exceptional researchers, without whom none of this work would be possible. Mark Weidman taught me too many lessons to even begin listing them. Jolene Mork built the original set up of the low frequency Raman experiment used herein and mentored me through my first several years at MIT. Yunan Gao served as a post doc while I built my own laser metrology technique and took all of the anxiety out of research with his patient explanations and frequent encouragement. Watcharaphol (Oat) Paritmongkol and I have worked especially closely these past two years, and I could not be more thankful for his involvement in my work. Oat is everything I could have asked for in a co-author and leader in his own right. Much of my success within the group has been through his foundational work and constant assistance. It is a pleasure every time he taps me on the shoulder. In addition, Liza Lee, Aaron Goodman, Matthew Ashner, helped significantly at various points during my doctoral research. Every other member of the group, former and current, has helped to make it a special environment to learn in, and I thank each of them for their contributions therein. They have all treated me as a friend, colleague, and equal, regardless of the circumstance.

Doctoral studies are as much about mentorship as they are about constructing the contents of a dissertation. For me, this part of the process has been easily the most rewarding. I have had the good fortune to work with some brilliant and infectiously excited students, all of whom have in some way contributed themselves to the work herein. Thank you Jareatha Abdul Raheem, Katharine Greco, Nick Morgante, Grace Noel, and Alexia Stollmann for at least letting me pretend to be a teacher.

In terms of my own mentors during my halting march towards graduation, I must begin by thanking my committee members Martin Bazant and Michael Strano. Both of them have helped to guide the development of this thesis in a way I could never have anticipated years

ago. In truth, when assembling my committee initially, I found myself thinking of any member as an examiner first. I, of course, could not have been more wrong. My committee have been teachers and valued advisors from my thesis proposal until today. To have had their full attention and incisive thinking to push me to think bigger and broader, and push further and deeper has been exhilarating. I thank them for their diligence and their mentorship.

Fittingly, I would like to close this section by thanking the person most singularly responsible for my development as a scientist, student, and researcher: my advisor Will Tisdale. Will is without a doubt in my mind the single best teacher I have ever seen, much less had the privilege of learning under. His enthusiasm is infectious, and he has the rare ability to turn even the most complicated topics under academic study into an intuitively reasoned mental picture perfectly suited to whichever audience he happens to be speaking to. I had always thought the best form of explaining any thought is a precise representation of its formation in my own rational mind. Will taught me how to form thoughts from the perspective of others, how to learn to explain concepts through their voice and to specifically their needs. Will has taught me how to run head first, without fear, into entirely new fields of research in order to solve a problem if necessary. What's more, he taught me what it means to learn exhaustively, and how not to lose sight of my intuition even when well outside of my comfort zone. He has been unceasingly patient with me while I struggled and supportive as I have succeeded. And throughout all of this his commitment to rigorous, fully developed scientific arguments meant to inspire and teach as much as they inform is the bastion of everything that is beautiful about the scientific method. He leads by example, so I offer my gratitude in the form of a guarantee that I will carry the lessons I have learned from him wherever I go from here.

Table of Contents

Chapter 1 – Introduction

1.1 Motivation:

A cardinal objective in modern materials engineering is the development of materials with properties that are precisely tuned to be ideally suited for a given application. The concept has always been rather simple, by varying the processing of a particular material, the microstructure and thus the performance-related properties of said material can be harnessed to some degree. And yet, despite remarkable strides in the development of new technology this paradigm has brought about, perhaps the most exciting and fundamentally powerful modern methodology for materials development is the idea that artificial solids can be intelligently built piece by piece from nanoscale "building blocks". This notion of processing nanomaterials into solids, a complete shift from the usual top-down approach to materials design, is particularly appealing not only because the microstructure of the artificial solid can, in theory, be completely controlled, but also because the nanomaterials in use have a unique set of capabilities unto themselves which can be leveraged to suit a host of new applications heretofore unconsidered.

With respect to the majority of critically relevant potential/current applications for these designer semiconductor nanomaterials, such as solar cells, light emitting diodes, lasers, transistors, and photodetectors, the optical and electronic properties of these materials are central contributors to the efficacy of devices. As a result, it is no surprise that the vast majority of scientific knowledge developed in building these devices originates in fundamental insight relating to those properties. On the other hand, thermal management, or the ability of the active material in a device to efficiently dissipate heat, receives considerably less attention. And yet for nearly every new innovation in the miniaturization of electronics, poor thermal management has been a significant limiting

factor in maintaining the functionality and reliability of devices. As a result, the determination of an appropriate conceptual framework for engineering the thermal properties of nanostructured artificial solids is of the utmost importance in the effort to advance any of the technologies listed above using these materials.

1.2 Hybrid Perovskites and the Bleeding Edge of Novel Semiconductors:

Hybrid organic-inorganic perovskites (HOIPs) have emerged over the past decade as a potential candidate to supplant conventional semiconductors for use in variegated device applications, not the least of which includes efficiency-competitive solar cells[1–9], color tunable light emitting diodes (LEDs)[10,11], sensitive photodetectors[12], and even lasers[13]. These materials are denoted via the chemical formula ABX_3, and exhibit a crystal structure in which a small organic cation (A), such as methylammonium (MA), is enclosed within metal (B) halide (X) octahedra. HOIPs owe their popularity in large part to physical properties such as high optical absorption coefficients, small exciton binding energies, and long/balanced electron-hole diffusion lengths[9,14].

Despite the exceptional qualities espoused above, devices utilizing hybrid perovskites such as $MAPbI_3$ have been diminished by insufficient long-term stability that stems primarily from the complexation of water in ambient moisture with the A-site organic cation[15,16]. One solution to this problem is to stabilize atomically thin sheets of perovskite materials within an insulating secondary organic phase consisting of larger molecules than would fit within a traditional perovskite lattice[17–23]. This solution utilizes a nanostructured 2D layered architecture to effectively protect the A-site cations from external moisture. Such

2D lead halide perovskites (2D LHPs) indeed exhibit improved stability relative to their bulk counterparts and have already begun to show promising performance metrics when used in solar cells[20,24–28], LEDs[29,30], and photodetectors[31].

These periodic layered nanostructures can be easily grown as macroscopically large crystals, with long-range order and minimal grain boundaries typically elusive for nanostructures. Additionally, since the perovskite sheets are thin enough to exhibit quantum confinement, the size of this phase can be controlled independently for further tunability of the optical and electronic properties.[32] Finally, the organic subphase can be manipulated to potentially improve performance, particularly in terms of the exciton binding energy and photoluminescence quantum yield.[29] For all of the strides made in progressing the optical and electronic properties of bulk (3D) and 2D LHPs, however, engineering the thermal properties of these materials remains only sparsely addressed.

1.3 What is Thermal Transport?

Classically, thermal transport is expressed using concepts relating to how a macroscopic medium alters its temperature in relation to a heat flux. Directly, this framework defines the thermal conductivity of a material as the efficiency with which a temperature gradient is converted into a heat flux. Similarly, the heat capacity is an expression of the amount of internal energy a medium can absorb without a change in temperature. As a result, it is no exaggeration to say that temperature is a central component of any interrogation into the thermal transport characteristics of a solid. But what is temperature, physically, and how

does must this conceptual framework be adapted when considering thermal energy exchange within nanostructured solids?

The usual definition of temperature is given as an equivalence condition for thermal equilibrium between two systems. This classical thermodynamics explanation of the relative hotness of matter and the direction in which it moves is developed from first principles and an application of the extremum principle. The numerical values typically assigned to temperature, of course, come from accepted calibrations that correlate some measureable property of a material to its relative hotness. Spoken in the language of the zeroth law of thermodynamics, all diathermal walls are equivalent (or all heat is of the same kind), so if a given system (the thermometer) is independently in thermal equilibrium with two other systems, then these two systems are themselves said to be in thermal equilibrium and must have the same temperature in all calibrated scales. In this way thermometers reveal some manifold of states as being composed of subsystems all distinctly in thermal equilibrium with one another. This is all to say that by definition, temperature only has meaning at thermal equilibrium.

Thermal transport, then, is the out of equilibrium process by which heat is exchanged in order to bring about thermal equilibrium. Put differently, if two distinct equilibrium systems (at different temperatures) are instantaneously placed in thermal contact with one another, heat must move from the hotter system to the colder in order to reestablish thermal equilibrium. The characteristics of this movement of heat form the foundation of heat transport. Unfortunately, since this movement is out of equilibrium, we cannot move deeper in discussing thermal transport with classical thermodynamics alone. We can now,

however, frame the problem appropriately by asking the question: what are the underlying processes that physically move heat from one location to another, and how do those dynamic processes conspire to establish thermal equilibrium? In answering these questions, we will see that what we lose in universality by leaving equilibrium thermodynamics behind, we gain in microscopic insights.

1.4 Origins of Thermal Conductivity

Since this dissertation is exclusively concerned with the thermal properties of solids, we will restrict our discussion of thermal transport to heat conduction. In order to answer the questions posed at the end of the previous section for conduction in solids, we begin by considering the microscopic heat carriers responsible for establishing thermal equilibrium in condensed phases. Since solids are comprised of an organized array of atoms with strong interactions between them, we need only consider two moving objects as potential heat carriers. Firstly, the electrons within the solid can move around and conduct heat via scattering (collisions). For metals wherein electrons are delocalized throughout the entire solid and capable of moving freely, these are the majority heat carriers. For semiconductors, however, wherein the mobility/free carrier concentration of electrons is comparatively low, we must consider another carrier. The second set of moving objects are the atoms themselves, which propagate heat by limited movements in space. During these movements, since each atom is highly coupled with its nearest neighbors, collections of atoms exhibit vibrations that propagate thermal energy as mechanical energy waves throughout the solid. These vibrational excitations of solids are called phonons, and they are indeed the dominant thermal energy carrier for semiconductors.

Now that we have established that phonons are the relevant thermal energy carrier, we can discuss the dynamics by which they interact and exchange heat. Surprisingly, a reasonably effective picture can be obtained from treating the phonons within a solid at any given moment as particles within an ideal gas. This analogy has proven useful for bulk semiconductors, and expresses the thermal conductivity as

$$k = \frac{1}{3} C v \Lambda \quad \text{(Eq. 1.1)}$$

where C is the heat capacity of the average phonon, v is the average velocity of the phonon, and Λ is the average mean free path of a phonon (average distance between collision events). Solids can, of course, support many different vibrations, and not all of them necessarily carry heat at anywhere near the average velocity. Additionally, the mean free path of these different phonons can vary considerably due to the various scattering processes occurring within the solid. As a result, even when using the simple expression given in Eq. 1.1, significant insight into the properties of the material are necessary. For nanostructured materials, this becomes even more important, as such materials by definition introduce interfaces and physical boundaries at the length scales at which phonons typically scatter.

1.5 Heat Transport in Multilayered Nanostructures

Unlike the bulk crystals discussed in the previous section, in which the primary mechanism responsible for thermal energy conduction is phonon-phonon scattering, layered materials typically exhibit decreased cross-plane thermal conductivity due to increased phonon-

boundary scattering at the interfaces between layers[33]. Since the layers are frequently shorter than the mean free path of a bulk phonon, these interfaces give rise to a classical size effect in the material that suppresses longer range phonon conduction. Essentially, phonons that are in the bulk capable of moving greater distances before scattering off of other phonons, instead scatter at interfaces at relatively short distances, reducing the effective thermal conductivity. This is not to say that long-range coherent phonons do not exist in layered materials. On the contrary, as is observed in inorganic superlattices, alternating extremely thin film layers of distinct semiconductors with atomically flat interfaces, long-range phonon conduction not only exists in these materials but also gives rise to exotic properties such as wave-like thermal conduction[34,35] in which phonons move without regard for the boundaries between layers. In superlattices, modulation of the thermal conductivity is implemented via control of both the constituent materials within each film and the interfaces between films[36–38]. Increased interface roughness, for instance, can exchange specular (wave-like) reflection/transmission of phonons for diffuse reflection/transmission (particle-like), which reduces the thermal conductivity by effectively reducing the quantity of coherently propagating phonons.

While thermal transport mechanisms in periodic layered inorganic structures such as superlattices have been extensively studied, the same type of understanding is less clear in hybrid organic-inorganic layered structures such as hybrid organic-inorganic perovskites. Although some preliminary studies have shown potential wave-like thermal transport in hybrid zincone organic-inorganic alternating films[39], the poor vibrational coupling across organic-inorganic interfaces adds an additional constraint to the interfaces described above[40,41]. Whereas organic molecules typically support vibrational modes in the 500-

3,000 cm^{-1}, inorganic crystals exhibit characteristically lower frequency modes (typically less than 500 cm^{-1}) owing to their heavier constituent atomic masses.

1.6 Thesis Overview:

The purpose of this thesis is to develop an understanding of the microscopic origins underlying the macroscopic thermal properties of 2D LHP crystals. To this end, chapter 2 will discuss the microscopic crystal structure and thermal stability of 2D LHPs. Chapter 3 will then highlight the building of an instrument for monitoring the thermal transport efficacy of macroscopic 2D LHP solids, specifically discussing the calculation of an effective thermal conductivity for the purposes of metering thermal conductivity suppression in these nanomaterials. Chapter 4 will provide the first measurements of thermal conductivities for 2D LHPs, in addition to discussing potential pathways for enhancing/suppressing the conductivity without impacting the desirable optical/electronic properties of the perovskites. Chapter 5 will probe the low frequency Raman spectrum of 2D LHPs for the purpose of outlining materials engineering avenues through which the fundamental pathways underlying the behavior provided in chapter 4 can be affected. In all cases, we will show that although 2D LHPs are nanostructured solids with long-range crystalline order and component domains as small as a single unit cell thick, they behave thermophysically as composite materials. As a result, future thermal engineering of these materials may only require a priori knowledge for the bulk phases of which they are comprised.

1.7 References

(1) Liu, M.; Johnston, M. B.; Snaith, H. J. Efficient Planar Heterojunction Perovskite Solar Cells by Vapour Deposition. *Nature* 2013, *501* (7467), 395–398. https://doi.org/10.1038/nature12509.

(2) Lee, M. M.; Teuscher, J.; Miyasaka, T.; Murakami, T. N.; Snaith, H. J. Efficient Hybrid Solar Cells Based on Meso-Superstructured Organometal Halide Perovskites. *Science.* 2012, *338* (6107), 643–647. https://doi.org/10.1126/science.1228604.

(3) Chen, Q.; Zhou, H.; Hong, Z.; Luo, S.; Duan, H.-S.; Wang, H.-H.; Liu, Y.; Li, G.; Yang, Y. Planar Heterojunction Perovskite Solar Cells via Vapor-Assisted Solution Process. *J. Am. Chem. Soc.* 2014, *136* (2), 622–625. https://doi.org/10.1021/ja411509g.

(4) Green, M. A.; Ho-Baillie, A.; Snaith, H. J. The Emergence of Perovskite Solar Cells. *Nat. Photonics* 2014, *8* (7), 506–514. https://doi.org/10.1038/nphoton.2014.134.

(5) Tan, H.; Jain, A.; Voznyy, O.; Lan, X.; García de Arquer, F. P.; Fan, J. Z.; Quintero-Bermudez, R.; Yuan, M.; Zhang, B.; Zhao, Y.; Fan, F.; Li, P.; Quan, L. N.; Zhao, Y.; Lu, Z.-H.; Yang, Z.; Hoogland, S.; Sargent, E. H. Efficient and Stable Solution-Processed Planar Perovskite Solar Cells via Contact Passivation. *Science.* 2017, *355* (6326), 722–726. https://doi.org/10.1126/science.aai9081.

(6) Burschka, J.; Pellet, N.; Moon, S.-J.; Humphry-Baker, R.; Gao, P.; Nazeeruddin, M. K.; Grätzel, M. Sequential Deposition as a Route to High-Performance Perovskite-Sensitized Solar Cells. *Nature* 2013, *499* (7458), 316–319. https://doi.org/10.1038/nature12340.

(7) Saliba, M.; Matsui, T.; Seo, J.-Y.; Domanski, K.; Correa-Baena, J.-P.; Nazeeruddin, M. K.; Zakeeruddin, S. M.; Tress, W.; Abate, A.; Hagfeldt, A.; Grätzel, M. Cesium-Containing Triple Cation Perovskite Solar Cells: Improved Stability, Reproducibility and High Efficiency. *Energy Environ. Sci.* 2016, *9* (6), 1989–1997. https://doi.org/10.1039/C5EE03874J.

(8) Zhou, H.; Chen, Q.; Li, G.; Luo, S.; Song, T. -b.; Duan, H.-S.; Hong, Z.; You, J.; Liu, Y.; Yang, Y. Interface Engineering of Highly Efficient Perovskite Solar Cells. *Science.* 2014, *345* (6196), 542–546. https://doi.org/10.1126/science.1254050.

(9) Mei, A.; Li, X.; Liu, L.; Ku, Z.; Liu, T.; Rong, Y.; Xu, M.; Hu, M.; Chen, J.; Yang, Y.; Grätzel, M.; Han, H. A Hole-Conductor–free, Fully Printable Mesoscopic Perovskite Solar Cell with High Stability. *Science.* 2014, *345* (6194), 295–298. https://doi.org/10.1126/science.1254763.

(10) Kim, Y. H.; Cho, H.; Heo, J. H.; Kim, T. S.; Myoung, N. S.; Lee, C. L.; Im, S. H.; Lee, T. W. Multicolored Organic/Inorganic Hybrid Perovskite Light-Emitting Diodes. *Adv. Mater.* 2015, *27* (7), 1248–1254. https://doi.org/10.1002/adma.201403751.

(11) Yuan, M.; Quan, L. N.; Comin, R.; Walters, G.; Sabatini, R.; Voznyy, O.; Hoogland, S.;

Zhao, Y.; Beauregard, E. M.; Kanjanaboos, P.; Lu, Z.; Kim, D. H.; Sargent, E. H. Perovskite Energy Funnels for Efficient Light-Emitting Diodes. *Nat. Nanotechnol.* 2016, *11* (10), 872–877. https://doi.org/10.1038/nnano.2016.110.

(12) Zhang, M.; Zhang, F.; Wang, Y.; Zhu, L.; Hu, Y.; Lou, Z.; Hou, Y.; Teng, F. High-Performance Photodiode-Type Photodetectors Based on Polycrystalline Formamidinium Lead Iodide Perovskite Thin Films. *Sci. Rep.* 2018, *8* (1), 11157. https://doi.org/10.1038/s41598-018-29147-6.

(13) Jia, Y.; Kerner, R. A.; Grede, A. J.; Rand, B. P.; Giebink, N. C. Continuous-Wave Lasing in an Organic-Inorganic Lead Halide Perovskite Semiconductor. *Nat. Photonics* 2017, *11* (12), 784–788. https://doi.org/10.1038/s41566-017-0047-6.

(14) Miyata, A.; Mitioglu, A.; Plochocka, P.; Portugall, O.; Wang, J. T. W.; Stranks, S. D.; Snaith, H. J.; Nicholas, R. J. Direct Measurement of the Exciton Binding Energy and Effective Masses for Charge Carriers in Organic-Inorganic Tri-Halide Perovskites. *Nat. Phys.* 2015, *11* (7), 582–587. https://doi.org/10.1038/nphys3357.

(15) Nie, W.; Blancon, J. C.; Neukirch, A. J.; Appavoo, K.; Tsai, H.; Chhowalla, M.; Alam, M. A.; Sfeir, M. Y.; Katan, C.; Even, J.; Tretiak, S.; Crochet, J. J.; Gupta, G.; Mohite, A. D. Light-Activated Photocurrent Degradation and Self-Healing in Perovskite Solar Cells. *Nat. Commun.* 2016, *7*, 11574. https://doi.org/10.1038/ncomms11574.

(16) Huang, W.; Manser, J. S.; Kamat, P. V.; Ptasinska, S. Evolution of Chemical Composition, Morphology, and Photovoltaic Efficiency of CH3NH3PbI3 Perovskite under Ambient Conditions. *Chem. Mater.* 2016, *28* (1), 303–311. https://doi.org/10.1021/acs.chemmater.5b04122.

(17) Mitzi, D. B.; Wang, S.; Feild, C. A.; Chess, C. A.; Guloy, A. M. Conducting Layered Organic-Inorganic Halides Containing <110>-Oriented Perovskite Sheets. *Science.* 1995, *267* (5203), 1473–1476. https://doi.org/10.1126/science.267.5203.1473.

(18) Mitzi, D. B. Synthesis, Crystal Structure, and Optical and Thermal Properties of (C4H9NH3)2MI4 (M = Ge, Sn, Pb). *Chem. Mater.* 1996, *8* (3), 791–800. https://doi.org/10.1021/cm9505097.

(19) Mitzi, D. B.; Dimitrakopoulos, C. D.; Kosbar, L. L. Structurally Tailored Organic–Inorganic Perovskites: Optical Properties and Solution-Processed Channel Materials for Thin-Film Transistors. *Chem. Mater.* 2001, *13* (10), 3728–3740. https://doi.org/10.1021/cm010105g.

(20) Smith, I. C.; Hoke, E. T.; Solis-Ibarra, D.; McGehee, M. D.; Karunadasa, H. I. A Layered Hybrid Perovskite Solar-Cell Absorber with Enhanced Moisture Stability. *Angew. Chemie Int. Ed.* 2014, *53* (42), 11232–11235. https://doi.org/10.1002/anie.201406466.

(21) Blancon, J.-C.; Tsai, H.; Nie, W.; Stoumpos, C. C.; Pedesseau, L.; Katan, C.; Kepenekian, M.; Soe, C. M. M.; Appavoo, K.; Sfeir, M. Y.; Tretiak, S.; Ajayan, P. M.;

Kanatzidis, M. G.; Even, J.; Crochet, J. J.; Mohite, A. D. Extremely Efficient Internal Exciton Dissociation through Edge States in Layered 2D Perovskites. *Science.* 2017, *355* (6331), 1288–1292. https://doi.org/10.1126/science.aal4211.

(22) Smith, M. D.; Pedesseau, L.; Kepenekian, M.; Smith, I. C.; Katan, C.; Even, J.; Karunadasa, H. I. Decreasing the Electronic Confinement in Layered Perovskites through Intercalation. *Chem. Sci.* 2017, *8* (3), 1960–1968. https://doi.org/10.1039/C6SC02848A.

(23) Smith, M. D.; Crace, E. J.; Jaffe, A.; Karunadasa, H. I. The Diversity of Layered Halide Perovskites. *Annu. Rev. Mater. Res.* 2018, *48* (1), 111–136. https://doi.org/10.1146/annurev-matsci-070317-124406.

(24) Cao, D. H.; Stoumpos, C. C.; Farha, O. K.; Hupp, J. T.; Kanatzidis, M. G. Two-Dimensional Homologous Perovskites as Light Absorbing Materials for Solar Cell Applications. *J. Am. Chem. Soc.* 2015, *137* (24), 7843–7850. https://doi.org/10.1021/jacs.5b03796.

(25) Tsai, H.; Nie, W.; Blancon, J.-C.; Stoumpos, C. C.; Asadpour, R.; Harutyunyan, B.; Neukirch, A. J.; Verduzco, R.; Crochet, J. J.; Tretiak, S.; et al. High-Efficiency Two-Dimensional Ruddlesden–Popper Perovskite Solar Cells. *Nature* 2016, *536* (7616), 312–316. https://doi.org/10.1038/nature18306.

(26) Wang, Z.; Lin, Q.; Chmiel, F. P.; Sakai, N.; Herz, L. M.; Snaith, H. J. Efficient Ambient-Air-Stable Solar Cells with 2D–3D Heterostructured Butylammonium-Caesium-Formamidinium Lead Halide Perovskites. *Nat. Energy* 2017, *2* (9), 17135. https://doi.org/10.1038/nenergy.2017.135.

(27) Grancini, G.; Roldán-Carmona, C.; Zimmermann, I.; Mosconi, E.; Lee, X.; Martineau, D.; Narbey, S.; Oswald, F.; De Angelis, F.; Graetzel, M.; Nazeeruddin, M. K. One-Year Stable Perovskite Solar Cells by 2D/3D Interface Engineering. *Nat. Commun.* 2017, *8*, 15684. https://doi.org/10.1038/ncomms15684.

(28) Li, P.; Zhang, Y.; Liang, C.; Xing, G.; Liu, X.; Li, F.; Liu, X.; Hu, X.; Shao, G.; Song, Y. Phase Pure 2D Perovskite for High-Performance 2D-3D Heterostructured Perovskite Solar Cells. *Adv. Mater.* 2018, 1805323. https://doi.org/10.1002/adma.201805323.

(29) Yang, X.; Zhang, X.; Deng, J.; Chu, Z.; Jiang, Q.; Meng, J.; Wang, P.; Zhang, L.; Yin, Z.; You, J. Efficient Green Light-Emitting Diodes Based on Quasi-Two-Dimensional Composition and Phase Engineered Perovskite with Surface Passivation. *Nat. Commun.* 2018, *9* (1), 570. https://doi.org/10.1038/s41467-018-02978-7.

(30) Liang, D.; Peng, Y.; Fu, Y.; Shearer, M. J.; Zhang, J.; Zhai, J.; Zhang, Y.; Hamers, R. J.; Andrew, T. L.; Jin, S. Color-Pure Violet-Light-Emitting Diodes Based on Layered Lead Halide Perovskite Nanoplates. *ACS Nano* 2016, *10* (7), 6897–6904. https://doi.org/10.1021/acsnano.6b02683.

(31) Tan, Z.; Wu, Y.; Hong, H.; Yin, J.; Zhang, J.; Lin, L.; Wang, M.; Sun, X.; Sun, L.; Huang, Y.; Liu, K.; Liu, Z.; Peng, H. Two-Dimensional (C 4 H 9 NH 3) 2 PbBr 4 Perovskite Crystals for High-Performance Photodetector. *J. Am. Chem. Soc.* 2016, *138* (51), 16612–16615. https://doi.org/10.1021/jacs.6b11683.

(32) Stoumpos, C. C.; Cao, D. H.; Clark, D. J.; Young, J.; Rondinelli, J. M.; Jang, J. I.; Hupp, J. T.; Kanatzidis, M. G. Ruddlesden-Popper Hybrid Lead Iodide Perovskite 2D Homologous Semiconductors. *Chem. Mater.* 2016, *28* (8), 2852–2867. https://doi.org/10.1021/acs.chemmater.6b00847.

(33) Chen, G. Size and Interface Effects on Thermal Conductivity of Superlattices and Periodic Thin-Film Structures. *J. Heat Transfer* 2016, *119* (May 1997), 220–229.

(34) Garg, J.; Chen, G. Minimum Thermal Conductivity in Superlattices: A First-Principles Formalism. *Phys. Rev. B - Condens. Matter Mater. Phys.* 2013, *87* (14), 1–5. https://doi.org/10.1103/PhysRevB.87.140302.

(35) Yang, B.; Chen, G. Partially Coherent Phonon Heat Conduction in Superlattices. *Phys. Rev. B* 2003, *67* (19), 1–4. https://doi.org/10.1103/PhysRevB.67.195311.

(36) Maris, H. J. Phonon Group Velocity and Thermal Conduction in Superlattices. *Phys. Rev. B* 1999, *60* (4), 2627–2630.

(37) Liang, Z.; Sasikumar, K.; Keblinski, P. Thermal Transport across a Substrate-Thin-Film Interface: Effects of Film Thickness and Surface Roughness. *Phys. Rev. Lett.* 2014, *113* (6), 1–5. https://doi.org/10.1103/PhysRevLett.113.065901.

(38) Giri, A.; Braun, J. L.; Hopkins, P. E. Effect of Crystalline/Amorphous Interfaces on Thermal Transport across Confined Thin Films and Superlattices. *J. Appl. Phys.* 2016, *119* (23). https://doi.org/10.1063/1.4953683.

(39) Liu, J.; Yoon, B.; Kuhlmann, E.; Tian, M.; Zhu, J.; George, S. M.; Lee, Y.; Yang, R. Ultralow Thermal Conductivity of Atomic/Molecular Layer-Deposited Hybrid Organic − Inorganic Zincone Thin Films. *Nano Lett.* 2013, *13*, 5594–5599.

(40) Majumdar, S.; Sierra-Suarez, J. a.; Schiffres, S. N.; Ong, W.-L.; Higgs, C. F.; McGaughey, A. J. H.; Malen, J. a. Vibrational Mismatch of Metal Leads Controls Thermal Conductance of Self-Assembled Monolayer Junctions. *Nano Lett.* 2015. https://doi.org/10.1021/nl504844d.

(41) Losego, M. D.; Grady, M. E.; Sottos, N. R.; Cahill, D. G.; Braun, P. V. Effects of Chemical Bonding on Heat Transport across Interfaces. *Nat. Mater.* 2012, *11* (6), 502–506. https://doi.org/10.1038/nmat3303.

(42) Qian, X.; Gu, X.; Yang, R. Lattice Thermal Conductivity of Organic-Inorganic Hybrid Perovskite CH3NH3PbI3. *Appl. Phys. Lett.* 2016, *108* (6). https://doi.org/10.1063/1.4941921.

(43) Pisoni, A.; Baris, O. S.; Spina, M.; Gaa, R. Ultra-Low Thermal Conductivity in Organic

– Inorganic Hybrid Perovskite CH3NH3PbI3. *J. Phys. Chem. Lett.* 2014, *5*, 2488–2492.

(44) Guo, Z.; Yoon, S. J.; Manser, J. S.; Kamat, P. V.; Luo, T. Structural Phase- and Degradation-Dependent Thermal Conductivity of CH3NH3PbI3 Perovskite Thin Films. *J. Phys. Chem. C* 2016, *120* (12), 6394–6401. https://doi.org/10.1021/acs.jpcc.6b00513.

(45) Hata, T.; Giorgi, G.; Yamashita, K. The Effects of the Organic-Inorganic Interactions on the Thermal Transport Properties of CH3NH3PbI3. *Nano Lett.* 2016, *16* (4), 2749–2753. https://doi.org/10.1021/acs.nanolett.6b00457.

Chapter 2 – Thermal Energy Storage in 2D Lead Halide Perovskites Near Room Temperature

The basis of this chapter has been submitted as:

N. S. Dahod, W. Paritmongkol, A. Stollmann, C. Settens, S-L. Zheng, W. A. Tisdale, "Melting Transitions of the Organic Subphase in Layered Two-Dimensional Alkylammonium Lead Halide Perovskites"

2.1 Introduction

In the bulk, organic-inorganic hybrid halide perovskites exhibit interesting temperature-dependent structural transformations[1–4]. At high temperatures, $MAPbI_3$ perovskites (MA = methylammonium) are observed in the cubic phase with the tilt angles of all octahedra minimized. In this phase, the octahedra readily rotate with respect to one another, and it is only their average positions which remain the same. At intermediate temperatures, one dimension of this rotational freedom is eliminated and the crystal structure is observed as tetragonal. At the lowest temperatures, yet another degree of freedom is eliminated and the observed crystal phase is orthorhombic, with fixed tilt angles across two dimensions[1]. These transitions are solid-solid phase transitions, also referred to as second-order phase transitions, which are marked by continuous transformations from one crystalline solid phase to another. These transitions have been linked to electronic property variations that impact device performance[5].

Like their bulk counterparts, 2D lead halide perovskites (2D LHPs) also exhibit a range of complicated temperature-dependent structural behavior[6–8]. 2D LHPs of the Ruddlesden-Popper type usually exist in orthorhombic crystal structures at room temperature[9]. In other low dimensional perovskite-type materials in which an orthorhombic room temperature phase also exists, a variety of novel transitions that are unique to the 2D material have been observed[8,10]. In particular, structural deformations of the octahedral layer – induced by changes to the packing geometry of the large organic cations separating these layers – strongly affect the energy, lifetime, and localization of the band-edge exciton[7,11–18]. As is the case for bulk perovskite materials, understanding these phase transitions is paramount to interpreting temperature-dependent electrical and optical

property measurements, as well as understanding the impact of 2D LHP structure on device performance.

In addition, melting transitions within the organic subphase of perovskite-like alkylammonium lead iodides (noted here as n=1 2D LHPs) have been previously identified.[8,19,20] These melting transitions are understood as order-disorder transformations confined to the organic sublayer, and serve to emphasize the hybrid nature of 2D layered perovskite-like materials. The transformations are typically characterized by tilting of the organic chains, contraction of the unit cell, and a discontinuous release of latent heat, as is also observed for other 2D molecular systems such as Langmuir-Blodgett Films[21] and self-assembled monolayers (SAMs) on metal surfaces.[22–24]

Herein, we investigate the phase behavior of 2D $(C_xH_{2x+1}NH_3)_2[(MA,FA)PbI_3]_{n-1}PbI_4$ layered perovskites near room temperature (-20ºC to +100ºC) as a function of the octahedral layer thickness (*n* = 1,2,3,4), the organic spacer chain length (BA = butylammonium, PA = pentylammonium, HA = hexylammonium), and the identity of the small organic cation (MA = methylammonium, FA = formamidinium). Using differential scanning calorimetry (DSC) and X-ray diffraction, we observe a single first-order phase transition in each 2D LHP corresponding to a melting transition in the organic spacer layer. The organic subphase transition temperature monotonically increases from 10ºC to 95.9ºC as the carbon chain length increases from C_4 to C_6, but is insensitive to the octahedral layer thickness, *n*. The latent heat of melting, ΔH_m, is found to be in the range 3–5 kJ/mol-spacer, indicating only partial disordering of the carbon chain. We discuss these findings in the context of melting

in other 2D molecular systems, and the implications for tuning properties of 2D layered perovskites through molecular engineering of the organic subphase.

2.2 Results & Discussion:

2.2.1 Lead Iodide 2D LHP Synthesis and Preliminary Characterization

2D lead halide perovskite (2D LHP) crystals were made *via* a modification of the cooling-induced crystallization method reported by Stoumpos *et al* (see Methods).[9] Successful synthesis was confirmed by the photoluminescence spectrum, with single peaks at known wavelengths indicating pure growth of 2D LHPs of a given octahedral layer thickness (Figure 2.1). Crystal structures were confirmed by single crystal and powder X-ray diffraction (XRD).

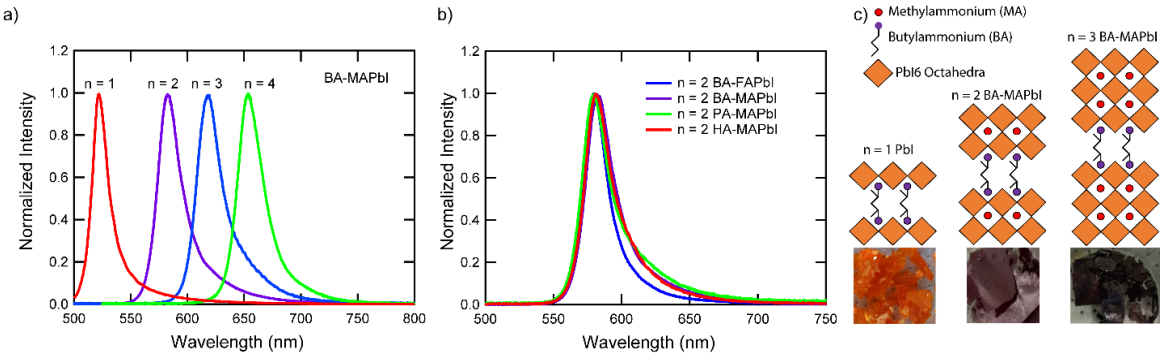

Figure 2.1. (a) Normalized room temperature photoluminescence spectra of butylammonium-MAPbI 2D LHPs with varying octahedral thickness, *n*. (b) Normalized room temperature photoluminescence spectra of n = 2 lead iodide 2D LHPs with varying spacer chain length (BA = butylammonium, PA = pentylammonium, HA = hexylammonium) and perovskite central cation (MA = methylammonium, FA = formamidinium). (c) Schematic illustration and corresponding photos of 2D LHP crystals.

2.2.2 Phase Transitions of the Organic Subphase in n=2 BA:MAPbI 2D LHPs

Differential scanning calorimetry (DSC) measurements of these 2D LHPs revealed characteristic phase transitions unlike those observed in the bulk. In particular, for n = 2 BA-MAPbI, a reversible phase transition was observed just below room temperature at 10 ºC (Figure 2.2a). Unlike the solid-solid phase transitions observed in bulk MAPbI3 perovskite[1,4], wherein the line-shape of the transition measured *via* DSC is characterized by a broad linewidth (>5 ºC) and low peak enthalpy deviation, the transition measured for n = 2 BA-MAPbI is sharp and accompanied by a large release of latent heat. This behavior is characteristic of a first-order transition, such as melting/freezing.

Single crystal and powder X-ray diffraction (XRD) measurements below and above the phase transition temperature, T_m, were used to identify the associated crystallographic transformations in the 2D LHPs studied. Above T_m, the crystal structure of n = 2 BA-MAPbI was confirmed to be in the Ruddlesden-Popper phase, with comparable crystal structures to those previously reported at similar temperatures[9]. Confirmation was reached by comparison of both powder diffraction data (Figure 2.2b) and structure solution from single crystal diffraction (Figure 2.2c). Below T_m, powder XRD suggests a uniaxial contraction of approximately 0.4 Å (calculated using Bragg's law) *via* uniform peak shifts with respect to the {h00} interlayer reflections of the high temperature structure (Figure 2.2b inset). It should be emphasized that the spacing between these planes is directly influenced by the thickness of the organic spacer layer, which is parallel to the organic-perovskite interface. The majority of the other peaks in the diffraction pattern, specifically

those that are nearly perpendicular to the {h00} planes (such as the {111} plane, which is 81º relative to the {h00} planes), display minimal change in peak position but exhibit significant inflation in peak linewidth (Figure 2.2b inset), the extent of which increases as a function of 2-theta. The deviation in peak linewidth suggests the presence of non-uniform strain along those crystallographic planes, which is known to cause such 2-theta dependent broadening.[25] In such cases, non-uniform deformations of the lattice lead to a broader distribution of Bragg diffractions for the same spacings, resulting in broader observed XRD peaks at the same positions.

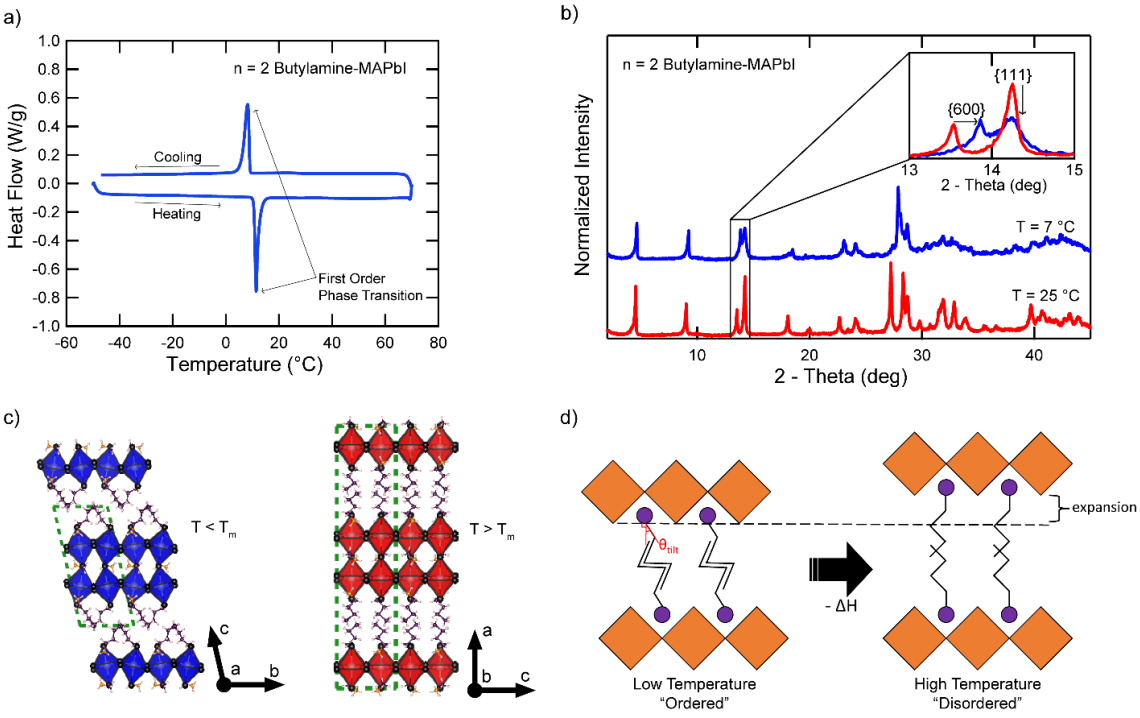

Figure 2.2. (a) Differential scanning calorimetry heating/cooling curve revealing reversible first order phase transition. (b) Powder X-ray diffraction above (red) and below (blue) the phase transition temperature, T_m. Inset shows contraction of {600} inter-sheet spacing and broadening of {111} quasi-vertical plane. (c) Space filling model obtained from single crystal X-ray diffraction data below (left) and above (right) the phase transition temperature, T_m. (d) Schematic illustration of the observed phase transition. Corrugation tilt angle is shown schematically (red) as the angle between the organic chains and the normal vector of the inorganic sheet.

Single crystal X-ray diffraction at 250 K (-23 ºC) confirmed the behavior deduced from powder XRD and DSC for the n = 2 BA-MAPbI layered perovskite. At this temperature, a uniaxial contraction of the sheet-to-sheet distance between inorganic planes by 0.52 Å was determined. Additionally, with respect to the organic spacer molecules themselves, the alkylammonium chains are tilted and intercalated with respect to their room temperature average positions in order to facilitate the contraction observed. This variation is quantified *via* the corrugation tilt of the chains, which measures the angle between the spacer molecule (line of best fit drawn from nitrogen to the terminal carbon atom) and the normal vector of the mean crystallographic plane of Pb atoms in the inorganic layer. The corrugation tilt (Figure 2.2d) of the organic spacers changed from approximately 21.4° in the high temperature phase to 36.75° after the transition (for a net tilt of 15.35°). At 250 K, the crystal structure of the composite organic-inorganic lattice is determined to be triclinic, with space group P-1 indicating the lowest possible symmetry. The loss of symmetry below T_m arises from a contraction within the organic layer and what appears to be a shearing of the inorganic layer by the newly ordered organic subphase. This shear stress is likely the origin of the broadened linewidths observed in the powder diffractograms.

2.2.3 Insensitivity of Organic Phase Transition to Inorganic Layer Thickness

Further confidence in the assignment of the first-order phase transition can be obtained by analyzing its dependence on the octahedral layer thickness (Figure 2.3). DSC heating curves of n = 3 & 4 BA-MAPbI show phase transitions of the same line-shape as for n = 2 BA-MAPbI, and at nearly identical temperatures (Figure 2.3a). Additionally, the latent heat (ΔH_m) obtained from these measurements shows similar consistency. When calculated

with respect to the total mass of the 2D material, there is a monotonic decrease in ΔH_m as the octahedral layer thickness increases (Figure 2.3b). If, however, ΔH_m is normalized by the mass of the alkyl chain spacer – rather than the entire 2D LHP – then the three ΔH_m values collapse to within 3% of the same value (Fig. 3b, right axis). This suggests that 1) the organic spacer phase is independently responsible for the phase transition observed and that 2) this phase transition is in fact the same regardless of the octahedral layer thickness. The observed variation in ΔH_m normalized by the total mass of the material simply reflects the changing mass ratio between the organic and inorganic subphases of the material as the octahedral layer thickness increases.

The conclusions drawn from analysis of the thickness-dependent DSC data are corroborated by X-ray diffraction. Powder XRD shows similar phase transitions in all three materials, characterized by uniaxial contraction between the {h00} planes of the high temperature phase, and the onset of nonuniform strain between vertical planes. Single crystal XRD of n = 3 & 4 BA-MAPbI confirms that the structural changes observed as a function of temperature are exactly as observed for the n = 2 analog. The low temperature structure is triclinic with P-1 symmetry, as for n = 2 BA-MAPbI, with an observed uniaxial lattice contraction of 0.54 Å & 0.48 Å, respectively, perpendicular to the inorganic sheet.

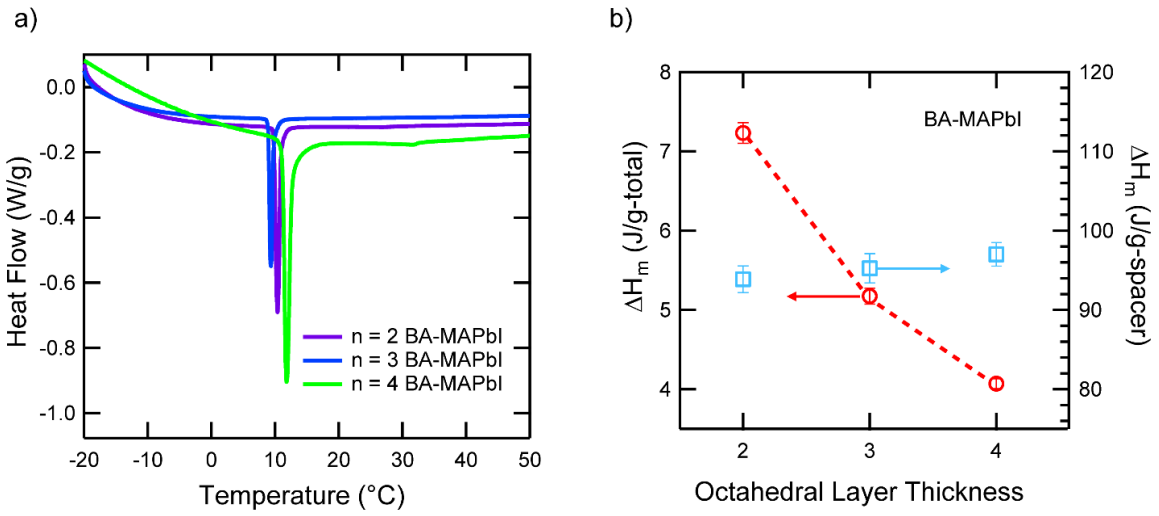

Figure 2.3. (a) Differential scanning calorimetry heating curves for BA-MAPbI 2D LHPs with varying octahedral thickness. A constant offset was added to the n = 4 data for visual clarity. Raw scans are provided in the supporting information. (b) Measured latent heat, ΔH_m, of the phase transition normalized either by total 2D LHP mass (red) or by mass of the organic subphase (blue).

The phase transition behavior shown in Figs. 2 and 3 is similar to melting transitions observed in other 2D alkane chain layers, such as alkylammonium lead iodides[19], alkanethiol self-assembled monolayers (SAMs) on Au surfaces[22–24] or Langmuir-Blodgett films of surfactants self-organized at liquid interfaces[21]. Unlike bulk alkanes, order-disorder transitions of tethered molecular layers are characterized by higher melting temperatures, T_m, due to fewer degrees of freedom in the bound state. In the case of 2D LHPs, the ammonium head group anchors the alkane chain to a fixed translational position with respect to the inorganic octahedral layer. Consequently, the frozen/ordered state can persist to higher temperature due to lower entropy of the 2D melt as compared to the 3D melt. The lower temperature "solid" phase shows tilted ordering of the organic chains, denser packing within the phase, and an exerted stress on the inorganic lattice. The inorganic subphase of the material, however, remains crystalline throughout the temperature range studied and experiences no uniform changes to its crystal structure.

2.2.4 Organic Spacer Chemistry Controls Organic Phase Transition

When the butylammonium (C_4) spacer was replaced by pentyl- (C_5) or hexylammonium (C_6), the phase transition shifted to higher temperature (Fig. 4a). The trend observed for melting temperature matches general melting trends expected as a function of alkyl chain length. The melting point of alkanes and alkylamines increases as a function of chain length, as do melting temperatures for alkylammonium lead iodides and SAMs[19,22]. For the 2D LHPs studied here, T_m increased from 10ºC to 77.9ºC to 95.9ºC as the spacer increased from C_4 to C_5 to C_6. As expected for a 2D molecular system, these melting temperatures are significantly higher than the bulk melting temperatures of butane, pentane, and hexane (-140º, -130ºC, and -95ºC, respectively).

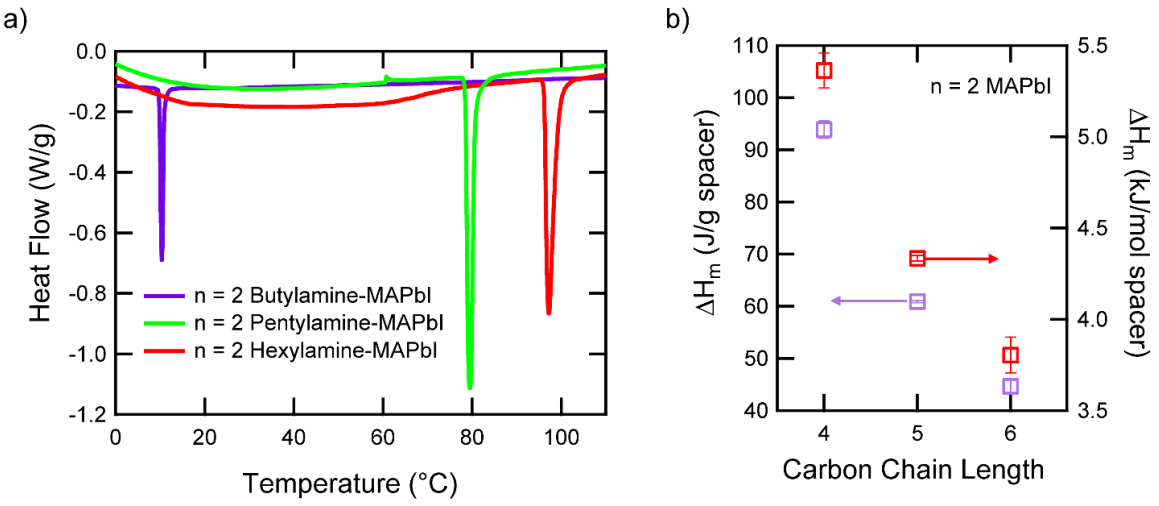

Figure 2.4. (a) Differential scanning calorimetry heating curves for n = 2 MAPbI with varying organic spacer chain length. A constant offset was added to the pentyl- and hexyl- data for visual clarity. (b) Measured latent heat, ΔH_m, of the phase transition normalized by mass of the organic subphase.

Somewhat surprisingly, ΔH_m decreased from 5.36 ±0.10 kJ/mol-spacer to 4.33 ±0.02 kJ/mol-spacer to 3.80 ±0.09 kJ/mol-spacer as the spacer chain length increased from C_4 to

C_5 to C_6 (Fig. 4b). By contrast, the corresponding latent heat of melting for butane, pentane, and hexane increases from 4.7 kJ/mol to 8.4 kJ/mol to 13 kJ/mol as the chain length increases. The latent heat of melting is often lower in 2D molecular systems than in 3D, especially for long-chain alkanes[26], because complete conformational freedom of the molecule is never achieved in 2D. A common way of interpreting this trend is that only a portion (presumably the end) of the alkane chain is melting. However, the decreasing trend of ΔH_m with increasing spacer chain length in our 2D LHPs is unexpected. A potential explanation is that some of the latent heat is associated with strain in the inorganic octahedral layer, and that the longer-chain C_5 and C_6 spacers are better able to absorb that strain within the organic layer. As observed for the butylammonium-spaced 2D LHPs, the melting transitions for the pentyl- and hexyl-spaced 2D LHPs are accompanied by uniaxial lattice contractions and no uniform change to the perovskite octahedra. The corrugation tilt of the organic chains also becomes more pronounced to accommodate the contraction. Unlike the butyl spacer, however, the pentyl and hexyl spacers do not show the same low symmetry high strain crystal structure at lower temperatures. The lower temperature space group (C2/c) is lower symmetry than the high temperature space group (Cmcm), but not to the same extreme as in BA-MAPbI. An additional, perhaps more likely explanation for this trend in the enthalpy of melting may be that the melting of longer chains is less complete than for shorter ones, which is supported by the calculated entropy of melting ($\Delta S_m = \Delta H_m / T_m$). As this parameter decreases concurrent with the decrease in enthalpy, the measured latent heat of melting is likely not due to other enthalpic contributions.

2.2.5 Influence of A-site Perovskite Cation on Organic Phase Transition

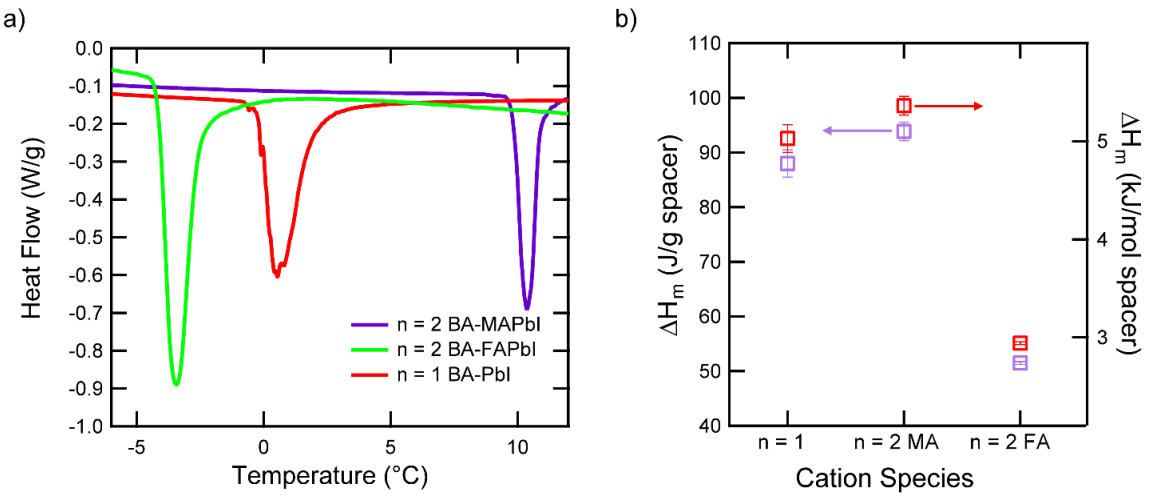

Figure 2.5. (a) Differential scanning calorimetry heating curves for butylamine-spaced lead iodide 2D LHPs with varying organic cation conditions. A constant offset was added to the n=2 BA-FAPbI data for visual clarity. Raw scans are provided in the supporting information. (b) Measured latent heat, ΔH_m, of the phase transition normalized by mass of the organic subphase.

If the methylammonium (MA) cation used within the perovskite octahedral subphase is replaced by formamidinium (FA) a phase transition with a significantly lower heat of melting per unit mass of organic spacer is observed *via* DSC, and with a melting temperature at -4.9 ºC instead of 10 ºC (Figure 2.5a). The phase transition is confirmed *via* powder and single crystal XRD to be identical to that observed for the MA-containing 2D LHPs (details summarized in Table 1). The decrease in ΔH_m is most likely attributed, as for the longer alkyl-chain spacers, to a decrease in the extent of melting for these materials, as a decrease in the melting entropy is measured alongside a decrease in the measured contraction of the organic subphase relative to n=2 BA-MAPbI.

For the n=1 BA-PbI 2D LHP, where no central cation is needed, the ligand melting transition is observed at 0 ºC. The latent heat of melting for the n=1 material, though, is 5-10% smaller than the other C_4-spaced 2D LHPs. The phase transition in n=1 BA-PbI at 0 ºC has been studied previously[8,19]. The smaller observed ΔH_m is most likely attributed to the change in melting temperature, as the entropy of melting remains essentially the same as for n=2 BA:MAPbI.

Table 2.1. Thermophysical properties of the alkyl chain melting transition in 2D LHPs. Lattice contractions marked by an asterisk were determined from Bragg's law; all others were measured *via* single crystal XRD.

Material	T_m (ºC)	ΔH_m (J/g)	ΔH_m (J/g-spacer)	ΔH_m (kJ/mol-spacer)	Contraction (Å)	Net corrugation tilt (deg.)	ΔS_m (J/K mol-spacer)
BA-MAPbI n = 2	10.0	7.23 ±0.13	93.9 ±1.7	5.36 ±0.10	0.52	15.35	18.9±0.4
BA-MAPbI n = 3	9.1	5.18 ±0.10	95.3 ±1.9	5.44 ±0.11	0.54	17.05	19.3±0.4
BA-MAPbI n = 4	10.5	4.07 ±0.06	97.0 ±1.5	5.54 ±0.09	0.48	7.35	19.5±0.3
BA-MAPbI n = 2	10.0	7.23 ±0.13	93.9 ±1.7	5.36 ±0.10	0.52	15.35	18.9±0.4
PA-MAPbI n = 2	77.9	5.74 ±0.02	60.9 ±0.2	4.33 ±0.02	0.55	13.9	12.3±0.6
HA-MAPbI n = 2	95.9	4.94 ±0.13	44.7 ±1.2	3.8 ±0.09	0.93	4.3	10.3±0.2
BA-MAPbI n = 2	10.0	7.23 ±0.13	93.9 ±1.7	5.36 ±0.10	0.52	15.35	18.9±0.4
BA-FAPbI n = 2	-4.9	3.93 ±0.02	51.5 ±0.2	2.94 ±0.01	0.43	14.03	11.0±0.1
BA-PbI n = 1	0.0	11.65 ±0.33	88.0 ±2.5	5.03 ±0.14	0.49*	N/A	18.4±0.5

2.3 Conclusions:

In summary, we have identified near-room-temperature phase transitions within a series of alkylammonium 2D LHPs. We have shown that these phase transitions are due to an ordering of the organic spacer phase, and that they are the same across all materials with the same organic spacer. Additionally, we have identified how choice of central cation within the perovskite phase can be used to subtly tune the temperature at which this transition occurs. Finally, we demonstrate that analogous transitions are observed when changing the alkyl chain length. Further work could be done, however, to more precisely catalog the structural variations of the organic molecules using techniques such as neutron scattering that are especially sensitive to such materials.

This work further motivates the need for rational design of the organic spacer phase in 2D LHPs, as the phase behavior therein may have implications for charge/heat transport or even device performance/stability at operating temperatures. The presence of near-room-temperature phase transitions within the organic phase of alkylammonium 2D LHPs could also provide an opportunity for future devices that utilize these phase changes for energy storage or thermal actuation.

2.4 Methods:

2.4.1 Synthesis of 2D LHP crystals.

2D lead halide perovskite (2D LHP) crystals were made *via* a modification of the cooling-induced crystallization method reported by Stoumpos *et al*.[9] A large volume of lead (II) iodide (PbI_2) was prepared by dissolving lead (II) oxide (PbO) in a hydriodic acid (HI) solution under reflux at 130 °C. After 15 mins, the solution was then cooled down to room temperature, before a small volume of it was transferred into a vial containing hypophosphorus acid (H_3PO_2). H_3PO_2 acts as a strong reducing agent, converting any residual I_2 to HI, yielding a bright yellow solution. The long-chain aklyamine (butylamine [BA], pentylamine [PA], or hexylamine [HA]), which will ultimately form the organic spacer layer within the 2D LHP, was then added dropwise into the acidic solution in an ice bath, forming an orange precipitate of n = 1 $(BA,PA,HA)_2PbI_4$ 2D LHP. In a separate vial, methylammonium iodide (or formamidinium iodide) salt was dissolved in an HI solution and subsequently added to the solution containing the n = 1 precipitate. The combined solution was heated on a hotplate at 130 °C for 4 minutes, until the solution turned clear,. Crystals were then grown by storing the clear solution in a thermos filled with hot sand at 110 °C overnight. Crystals were isolated by suction filtration and dried under reduced pressure for at least 12 hours.

2.4.2 Differential scanning calorimetry (DSC).

A Q2000 instrument from TA instruments was used for the DSC analysis. Inert atmosphere environment was maintained in the sample chamber using a nitrogen gas cylinder set to a flow rate of 50 mL/min. An extra refrigerated cooling system (RCS 40, TA Instruments) was used to widen the available temperature range to between −40 and 400 °C. Tzero® pans and lids were used with ~5-8 mg of sample. A heating rate of 10 °C/min was applied and the samples were scanned from −40 to 120 °C. When determining the enthalpy of fusion for a given sample, the DSC curve was integrated for 10 °C centered on the transition temperature. All measurements were taken in triplicate to determine uncertainty. Calculation of the melting temperature and the enthalpy of fusion was done using TA Universal Analysis software.

2.4.3 Photoluminescence.

Steady-state photoluminescence measurements were performed on an inverted microscope (Nikon, Ti-U Eclipse). The samples were excited by focusing the output of a 405 nm pulsed laser diode (LDHDC-405M, Picoquant, 2.5 MHz repetition rate) by an objective lens (Nikon, CFI S Plan Fluor ELWD, 40x, 0.6 NA) to <1 µm spot. The photoluminescence was collected in the epi configuration, and passed through a dichroic mirror and a long-pass filter. Then, it was directed into a spectrograph (SP-2500, Princeton Instruments) mounted with a cooled charge-coupled detector (Princeton Instruments, Pixis). Laser power was kept below ~125 nW throughout the measurements.

2.4.4 Powder X-ray diffraction (XRD)

Powder XRD data was taken using a PANalytical X'Pert Pro MPD X-ray diffractometer (Cu Kα radiation, $\lambda = 1.54184$ Å) with High-Speed Bragg-Brentano Optics. A 0.04 rad soller slit, a $1°$ anti-scatter slit, a 10mm mask and a programmable divergence slit with an illuminated length of 6mm were used in the incident beam path. The diffracted beam optics included a 0.04 rad soller slit, a Ni Filter and an automatic receiving slit. The detector was an ultra-fast X'Celerator RTMS detector. The angular step in 2θ was $0.04°$. Two different stages were used in the PANalytical to take temperature dependent measurements; the Oxford Cryosystems PheniX cooler, and an Anton Paar HTK-1200N heating stage. All measurements were taken during heating, with room temperature data taken at the beginning and end of the experiment to ensure reversibility.

2.4.5 Single-Crystal X-ray Crystallography

A crystal was mounted on a diffractometer at 300 K. The temperature was raised/lowered down to measurement temperatures at a rate of 5K/h, then data sets were collected. The intensities of the reflections were collected by means of a Bruker APEX II CCD diffractometer ($Mo_{K\alpha}$ radiation, λ=0.71073 Å), and equipped with an Oxford Cryosystems nitrogen flow apparatus. The collection method involved 0.5° scans in ω at 28° in 2θ.

2.5 References

(1) Whitfield, P. S.; Herron, N.; Guise, W. E.; Page, K.; Cheng, Y. Q.; Milas, I.; Crawford, M. K. Structures, Phase Transitions and Tricritical Behavior of the Hybrid Perovskite Methyl Ammonium Lead Iodide. *Sci. Rep.* 2016, *6* (1), 35685. https://doi.org/10.1038/srep35685.

(2) Stoumpos, C. C.; Malliakas, C. D.; Kanatzidis, M. G. Semiconducting Tin and Lead Iodide Perovskites with Organic Cations: Phase Transitions, High Mobilities, and near-Infrared Photoluminescent Properties. *Inorg. Chem.* 2013, *52* (15), 9019–9038. https://doi.org/10.1021/ic401215x.

(3) Maughan, A. E.; Ganose, A. M.; Candia, A. M.; Granger, J. T.; Scanlon, D. O.; Neilson, J. R. Anharmonicity and Octahedral Tilting in Hybrid Vacancy-Ordered Double Perovskites. *Chem. Mater.* 2018, *30* (2), 472–483. https://doi.org/10.1021/acs.chemmater.7b04516.

(4) Harwell, J. R.; Payne, J. L.; Sajjad, M. T.; Heutz, F. J. L.; Dawson, D. M.; Whitfield, P. S.; Irvine, J. T. S.; Samuel, I. D. W.; Carpenter, M. A. Role of Lattice Distortion and A Site Cation in the Phase Transitions of Methylammonium Lead Halide Perovskites. *Phys. Rev. Mater.* 2018, *2* (6), 065404. https://doi.org/10.1103/PhysRevMaterials.2.065404.

(5) Quarti, C.; Mosconi, E.; Ball, J. M.; D'Innocenzo, V.; Tao, C.; Pathak, S.; Snaith, H. J.; Petrozza, A.; De Angelis, F. Structural and Optical Properties of Methylammonium Lead Iodide across the Tetragonal to Cubic Phase Transition: Implications for Perovskite Solar Cells. *Energy Environ. Sci.* 2016, *9* (1), 155–163. https://doi.org/10.1039/c5ee02925b.

(6) Saparov, B.; Mitzi, D. B. Organic–Inorganic Perovskites: Structural Versatility for Functional Materials Design. *Chem. Rev.* 2016, *116* (7), 4558–4596. https://doi.org/10.1021/acs.chemrev.5b00715.

(7) Smith, M. D.; Jaffe, A.; Dohner, E. R.; Lindenberg, A. M.; Karunadasa, H. I. Structural Origins of Broadband Emission from Layered Pb–Br Hybrid Perovskites. *Chem. Sci.* 2017, *8* (6), 4497–4504. https://doi.org/10.1039/C7SC01590A.

(8) Billing, D. G.; Lemmerer, A. Synthesis, Characterization and Phase Transitions in the Inorganic–organic Layered Perovskite-Type Hybrids [(CnH2n+1NH3)2PbI4], n = 4, 5 and 6. *Acta Crystallogr. Sect. B Struct. Sci.* 2007, *63* (5), 735–747. https://doi.org/10.1107/S0108768107031758.

(9) Stoumpos, C. C.; Cao, D. H.; Clark, D. J.; Young, J.; Rondinelli, J. M.; Jang, J. I.; Hupp, J. T.; Kanatzidis, M. G. Ruddlesden-Popper Hybrid Lead Iodide Perovskite 2D Homologous Semiconductors. *Chem. Mater.* 2016, *28* (8), 2852–2867. https://doi.org/10.1021/acs.chemmater.6b00847.

(10) Liao, W. Q.; Mei, G. Q.; Ye, H. Y.; Mei, Y. X.; Zhang, Y. Structural Phase Transitions of a Layered Organic-Inorganic Hybrid Compound: Tetra(Cyclopentylammonium) Decachlorotricadmate(II), [C5H9NH3]4Cd3Cl10. *Inorg. Chem.* 2014, *53* (17), 8913–8918. https://doi.org/10.1021/ic500554z.

(11) Cortecchia, D.; Neutzner, S.; Srimath Kandada, A. R.; Mosconi, E.; Meggiolaro, D.; De Angelis, F.; Soci, C.; Petrozza, A. Broadband Emission in Two-Dimensional Hybrid Perovskites: The Role of Structural Deformation. *J. Am. Chem. Soc.* 2017, *139* (1), 39–42. https://doi.org/10.1021/jacs.6b10390.

(12) Passarelli, J. V; Fairfield, D. J.; Sather, N. A.; Hendricks, M. P.; Sai, H.; Stern, C. L.; Stupp, S. I. Enhanced Out-of-Plane Conductivity and Photovoltaic Performance in n = 1 Layered Perovskites through Organic Cation Design. *J. Am. Chem. Soc.* 2018, *140* (23), 7313–7323. https://doi.org/10.1021/jacs.8b03659.

(13) Hautzinger, M. P.; Dai, J.; Ji, Y.; Fu, Y.; Chen, J.; Guzei, I. A.; Wright, J. C.; Li, Y.; Jin, S. Two-Dimensional Lead Halide Perovskites Templated by a Conjugated Asymmetric Diammonium. *Inorg. Chem.* 2017, *56* (24), 14991–14998. https://doi.org/10.1021/acs.inorgchem.7b02285.

(14) Takeoka, Y.; Asai, K.; Rikukawa, M.; Sanui, K. Systematic Studies on Chain Lengths, Halide Species, and Well Thicknesses for Lead Halide Layered Perovskite Thin Films. *Bull. Chem. Soc. Jpn.* 2006, *79* (10), 1607–1613. https://doi.org/10.1246/bcsj.79.1607.

(15) Mao, L.; Wu, Y.; Stoumpos, C. C.; Wasielewski, M. R.; Kanatzidis, M. G. White-Light Emission and Structural Distortion in New Corrugated Two-Dimensional Lead Bromide Perovskites. *J. Am. Chem. Soc.* 2017, *139* (14), 5210–5215. https://doi.org/10.1021/jacs.7b01312.

(16) Nazarenko, O.; Kotyrba, M. R.; Yakunin, S.; Aebli, M.; Rainò, G.; Benin, B. M.; Wörle, M.; Kovalenko, M. V. Guanidinium-Formamidinium Lead Iodide: A Layered Perovskite-Related Compound with Red Luminescence at Room Temperature. *J. Am. Chem. Soc.* 2018, *140* (11), 3850–3853. https://doi.org/10.1021/jacs.8b00194.

(17) Kamminga, M. E.; de Wijs, G. A.; Havenith, R. W. A.; Blake, G. R.; Palstra, T. T. M. The Role of Connectivity on Electronic Properties of Lead Iodide Perovskite-Derived Compounds. *Inorg. Chem.* 2017, *56* (14), 8408–8414. https://doi.org/10.1021/acs.inorgchem.7b01096.

(18) Du, K.; Tu, Q.; Zhang, X.; Han, Q.; Liu, J.; Zauscher, S.; Mitzi, D. B. Two-Dimensional Lead(II) Halide-Based Hybrid Perovskites Templated by Acene Alkylamines: Crystal Structures, Optical Properties, and Piezoelectricity. *Inorg. Chem.* 2017, *56* (15), 9291–9302. https://doi.org/10.1021/acs.inorgchem.7b01094.

(19) Barman, S.; Venkataraman, N. V; Vasudevan, S.; Seshadri, R. Phase Transitions in the Anchored Organic Bilayers of Long-Chain Alkylammonium Lead Iodides (CnH2n+1NH3)2PbI4; n = 12, 16, 18. *J. Phys. Chem. B* 2003, *107* (8), 1875–1883.

https://doi.org/10.1021/jp026879h.

(20) Mao, L.; Stoumpos, C. C.; Kanatzidis, M. G. Two-Dimensional Hybrid Halide Perovskites: Principles and Promises. *J. Am. Chem. Soc.* 2018. https://doi.org/10.1021/jacs.8b10851.

(21) Naselli, C.; Rabolt, J. F.; Swalen, J. D. Order–disorder Transitions in Langmuir–Blodgett Monolayers. I. Studies of Two-dimensional Melting by Infrared Spectroscopy. *J. Chem. Phys.* 1985, *82* (4), 2136–2140. https://doi.org/10.1063/1.448351.

(22) Fenter, P.; Eisenberger, P.; Liang, K. S. Chain-Length Dependence of the Structures and Phases of CH3(CH2)n-1SH Self-Assembled on Au(111). *Phys. Rev. Lett.* 1993, *70* (16), 2447–2450. https://doi.org/10.1103/PhysRevLett.70.2447.

(23) Hostetler, M. J.; Manner, W. L.; Nuzzo, R. G.; Girolami, G. S. Two-Dimensional Melting Transitions of Rod-like Molecules Analyzed by Reflection-Absorption Infrared Spectroscopy. *J. Phys. Chem.* 1995, *99* (41), 15269–15278. https://doi.org/10.1021/j100041a050.

(24) Badia, A.; Lennox, R. B.; Back, R. Phase Transitions in Self-Assembled Monolayers Detected by Electrochemistry. *Angew. Chemie Int. Ed. English* 2018, *33* (22), 2332–2335. https://doi.org/10.1002/anie.199423321.

(25) Rivnay, J.; Noriega, R.; Kline, R. J.; Salleo, A.; Toney, M. F. Quantitative Analysis of Lattice Disorder and Crystallite Size in Organic Semiconductor Thin Films. *Phys. Rev. B* 2011, *84* (4), 045203. https://doi.org/10.1103/PhysRevB.84.045203.

(26) Zhang, Z. S.; Wilson, O. M.; Efremov, M. Y.; Olson, E. A.; Braun, P. V; Senaratne, W.; Ober, C. K.; Zhang, M.; Allen, L. H. Heat Capacity Measurements of Two-Dimensional Self-Assembled Hexadecanethiol Monolayers on Polycrystalline Gold. *Appl. Phys. Lett.* 2004, *84* (25), 5198–5200. https://doi.org/10.1063/1.1764938.

Chapter 3 – Building a Frequency Domain Thermoreflectance Technique for Nanoscale Thermal Transport Metrology

3.1 Introduction

In this chapter we discuss the experimental technique, Frequency Domain Thermoreflectance (FDTR), as built and used by the author for the thermal transport measurements central to this dissertation. We begin with a brief perspective on the history of this and analogous techniques used for thermal metrology. Following this, the essential theory is presented and used to develop an intuition for conceptualizing experimental results. Finally, the experimental details for building, aligning, and operating the instrument itself are provided as a means to discuss the strengths and limitations of its operation. It should be noted that this is not the first report nor dissertation discussing the subject of FDTR. Although the prominence of this technique has only recently arisen, several other wonderful papers and reports are recommended reading for the interested reader. The following discussion of both the experiment and the underlying theory used for analysis is meant as an explanation of useful context, relevant experimental considerations, and where applicable the (to our knowledge) original insights used by the author in building/using this technique.

3.2 A Brief History of Thermal Wave Measurement

In simplest terms, when thinking about designing an experiment to measure the thermal conductivity of a macroscopic solid, one might intuitively begin by inspection of Fourier's law and the diffusion equation. From such a perspective, the most obvious tautological representation of the thermal conductivity is that of a proportionality constant between the heat flux perturbing the solid and the spatial temperature gradient established within the solid in response. The smaller the gradient for a given heating input, the larger the

conductivity, and vice versa. In thinking of thermal conductivity from this empirical formulation, as the relative resistance of a material in forming a temperature gradient when absorbing/emitting heat, an experiment that isolates the conductivity becomes pellucid. Such a technique might carefully apply and measure a heat flux to the solid in question, whilst measuring the change in temperature at some other point on the solid a known distance from the heating input. This experimental technique is of course well known as Searle's bar method, and allows for extraction of the thermal conductivity through simplification of Fourier's law as in Eq 3.1 below:

$$k = \frac{q}{\nabla T} = \frac{Q/A}{\Delta T/L} [=] \frac{W/m^2}{K/m} \qquad (Eq. 3.1)$$

Where k represents the thermal conductivity (W/mK), q is the heat flux (W/m^2), T is the temperature (K), A is the cross-sectional area of the solid that is being heated (m^2), and L is the distance between the heat source and the temperature measurement (typically the end of the "bar" of solid). While such an experimental formalism is useful conceptually and practically for very large solids, it relies on several key assumptions that limit its use. Specifically, the entire bar must be completely isolated from the environment in order to minimize heat losses to the surroundings. Additionally, the heating flux must be measured with high accuracy in order to obtain a similarly accurate measurement of the thermal conductivity.

Nanomaterials, of course, are not typically synthesized as macroscopic bars. Rather, they are deposited as films, small crystals, or even single atomic-layer junctions. Furthermore, by definition any microelectronic device involves the heating of materials on much smaller length scales than those at which "classical" techniques such as Searle's method can be

used. Many sophisticated techniques have been developed to meet this challenge.[1,2] As above, two key elements are typically required for any heat transport measurement: a heater and a thermometer. That is, something that applies heat in a known and measureable way and something that measures exchange of heat in a known and measureable way. The heater and thermometer must each be designed so as to operate with a high degree of sensitivity within the relevant length-scale of the sample (in this case the through-plane thickness of a thin film). Thus, in designing nanoscale thermal measurement techniques, implementation of a heater that will provide a meaningful gradient of heat over the depth of the sample and a thermometer that can measure temperature fluctuations of this necessarily lesser magnitude with a spatial resolution appropriate for the system under study are required. In this spirit, a number of various heating/thermometry techniques have been developed for use in nanoscale systems and thin films[2–4]. One increasingly utilized technique for measuring the temperature of small systems is time/frequency domain thermoreflectance[5–7].

Time and frequency domain thermoreflectance (TDTR and FDTR respectively), both follow a long lineage of techniques that measure thermal properties of solids using the diffusion of thermal waves. First developed by Rosenwaig et al. and advanced by others since such as Cahill, Chen and Schmidt, these techniques represent a rich history of research in sensitively measuring the thermal transport in small systems.[6–9] The thermal wave measurement concept answers the need for increased sensitivity raised in departing from classical techniques. In the context of this dissertation, a thermal wave is a temperature modulation that propagates through a solid of interest. For instance, oscillatory heating of a surface launches a thermal wave into the underlying solid, dispersing as it does so. This dispersion is captured by the Fourier transform of the diffusion equation for temperature,

$$\frac{\partial^2\theta(\omega,x)}{\partial x^2} = \frac{i\omega}{\alpha}\theta(\omega,x) \qquad (3.2)$$

Expressed in one dimension for simplicity, in which x is the spatial coordinate, θ is the temperature represented in Fourier space, ω is frequency, and α is the thermal diffusivity. In order to see how the use of thermal waves provide spatial sensitivity in experiments, we can scale the above equation. For the case where a surface temperature modulation at frequency ω_o is the source of the thermal wave, the characteristic length scale of the experiment (δ_p), intuitively termed the penetration depth is seen to be

$$\frac{1}{{\delta_p}^2} \sim \frac{i\omega_o}{\alpha} \qquad (3.3)$$

$$\delta_p \sim \sqrt{\frac{\alpha}{i\omega_o}} \qquad (3.4)$$

This expression reveals the key advantage of using temperature modulations to monitor thermal transport, as the frequency directly controls the penetration depth of the experiment. Furthermore, this relationship clarifies that more insulating samples such as perovskites require higher heating frequencies to compensate for their low diffusivities.

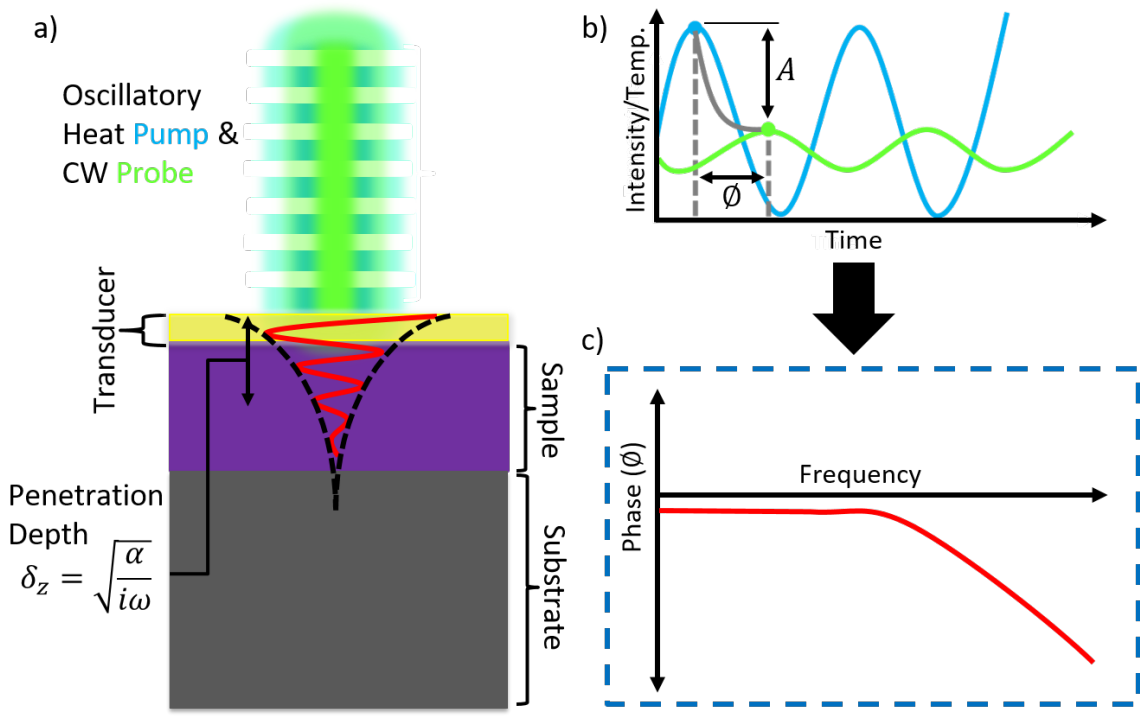

Figure 3.1. Overview of the FDTR experiment, a) Typical sample preparation is shown, wherein a sample of interest is attached to some substrate with known thermal properties and an exogenous transducer is deposited on the sample surface. The pump and probe lasers are reflected collinearly off of the surface of the sample, with only the pump intensity modulated before reflection. The red line shows the attenuation of the thermal wave as it penetrates into the sample, revealing the sensitivity of the measurement. For large enough samples (>2 µm), the experiment is insensitive to even the substrate. B) Shows the characteristics of the thermal waves measured to extract thermal transport properties. Due to thermal transport, the modulation of the reflected probe light (green) must exhibit some phase lag from that of the pump. C) By sweeping over a range of frequencies, the enough data can be collected to compare to a thermal model (derived from a heat equation) for extraction of relevant thermal parameters.

FDTR (shown schematically in Figure 3.1) sensitively measures the thermal response of a sample by using a pump-probe laser apparatus to sinusoidally heat a surface while also measuring the evolution of the surface temperature of this same surface. To do this reliably, this technique makes use of an exogenous metal (gold, herein) transducer to act as the physical heater and thermometer in contact with the sample. An intensity

modulated pump laser is reflected off of the surface of this transducer, creating the thermal wave (surface temperature oscillation). This oscillation is at the same frequency as the pump laser, but, since the sample is not a perfect conductor, the phase and amplitude of the surface temperature are shifted from that of the pump, as if by a thermal impedance.

In order to measure the surface temperature of the transducer, the property of thermoreflectance is leveraged. When the temperature of the metal transducer is varied, its index of refraction and thus its reflectivity also vary. So, in response to the surface temperature oscillation induced by the pump, the transducer reflectivity also oscillates. To measure this, a probe beam collinear with the pump laser is simultaneously reflected off of the transducer surface. The probe beam is initially unmodulated (continuous wave), but upon reflection from the metal surface is modulated according to the thermoreflectance and thus the surface temperature. The relative phase of the pump (reference) and probe (signal) beams can then be compared to map extract meaningful information about thermal transport in the sample.

This extraction is typically carried out by numerical fitting of the relative phase response of the probe (phase vs. modulation frequency) to a solution of the diffusion equation for the sample geometry, a process which will be exhaustively discussed below. The implementation of Fourier's law implies naturally that the films under study exhibit effectively diffusive transport throughout the penetration depth of heating; an assumption that breaks down for a variety of nanoscale systems.[10,11] Since the materials studied in this dissertation all form macroscopic solids in the form of small crystals (~1mm thick), the

Fourier law analysis will be preserved as a measure of the effective thermal conductivity of the solid, a distinction previously explained in chapter 2.

3.3 Fourier's Law Description of a FDTR Experiment

It is not immediately intuitive to think of transport in the frequency domain. Specifically, inspection of the phase response (relative phase lag vs. modulation frequency) of an FDTR experiment does not offer the same clarity that a temporal decay curve does, wherein parameters such as faster decay times are easily visualized. What does a large phase lag imply about thermal transport? What shape should such a curve take? Although much of this theory is likely more digestible by those familiar with measurements of electrical impedances and AC circuits, in which Bode plots intuitively describe analogous phenomena, such a conceptual basis is not necessarily as familiar to a chemical engineer. More importantly, this behavior is highly dependent on many more parameters than may be inferred from the simplicity of the shape of the response. Thus, in order to extract relevant parameters such as the thermal conductivity, heat capacity, or a boundary conductance from the results of an FDTR experiment, a thermal model based on Fourier's law and the diffusion equation (or alternatively nondiffusive heat transport equations where applicable) is required.

3.3.1 Analytical Solution of the Heat Diffusion Equation for FDTR

The typical system geometry studied in this dissertation, shown in Figure 3.2, consists of a metal (gold) transducer atop a solid sample that was previously mounted on a substrate. In practice, the sample is large enough relative to the penetration depth of the measurement that the substrate can be ignored during analysis. As shown in Figure 3.2, however, the forthcoming derivations will remain generalized for an arbitrary number of thin films layered between the substrate (layer S) and the transducer (layer 1).

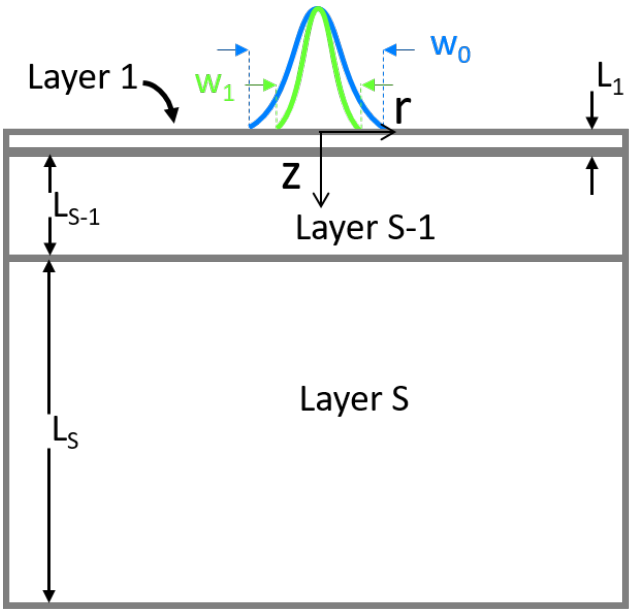

Figure 3.2. Representation of sample geometry for analysis of FDTR experiment. L is layer thickness, w is the $1/e^2$ beam waist of the pump (0) and probe (1). Each layer has its own set of thermal properties (volumetric heat capacity, thermal conductivity).

As stated previously, the FDTR technique uses a periodic heat flux from the pump laser at the surface of the transducer (z=0, r=0) and a thermometric probe laser that measures the

temperature of the surface. Thus, we must solve the heat equation (Eq. 3.5) for the surface temperature.

$$\frac{\sigma_r}{r}\frac{\partial}{\partial r}\left(r\frac{\partial T}{\partial r}\right)+\sigma_z\frac{\partial^2 T}{\partial z^2}=\rho c\frac{\partial T}{\partial t} \qquad (3.5)$$

In the above 2D+t heat diffusion equation, r is the radial coordinate and z is the axial coordinate, as defined in Figure 3.2, T is the temperature, t is time, ρ is the mas density, c is the specific heat, and $\sigma_{z,r}$ is the conductivity in either the z or r direction. Because we are interested in the frequency response of the surface temperature, and because of the corresponding time-harmonic behavior of the system, we begin by applying the Fourier transform to Eq. 3.5. This yields,

$$\frac{\sigma_r}{r}\frac{\partial}{\partial r}\left(r\frac{\partial \theta(\omega,r)}{\partial r}\right)+\sigma_z\frac{\partial^2 \theta(\omega,r)}{\partial z^2}=\rho ci\omega\theta(\omega,r) \qquad (3.6)$$

Where $\theta(\omega,r)$ represents the temperature in the frequency domain and ω represents the angular frequency. Note that although we do not note it, $\theta(\omega,r)$ remains a function of z. We will use this notation throughout the forthcoming derivation. Next, using the cylindrical symmetry of the experiment, we use the zero order Hankel transform to reduce the radial component. The zero order Hankel transform is defined as,

$$\Theta(k)=\mathcal{H}_0\{\theta(r)\}=\int_0^\infty \theta(r)\,J_o(kr)\,r\,dr \qquad (3.7)$$

Where k is the transform variable (not to be confused with the thermal conductivity), J_o is the Bessel function of the first kind of order 0, and Θ is the temperature in Hankel (and in our case also Fourier) space. Applying this transform to Eq, 3.6 and using integration by parts on the transform of the left hand term yields

$$-\sigma_r k^2\Theta(k,\omega)+\sigma_z\frac{\partial^2\Theta(k,\omega)}{\partial z^2}=\rho ci\omega\Theta(k,\omega) \qquad (3.8)$$

Which can be further rearranged to obtain,

$$\frac{\partial^2 \Theta(k,\omega)}{\partial z^2} = q^2 \Theta(k,\omega) \quad with, \;\; q^2 \equiv \frac{\sigma_r k^2 + \rho c i\omega}{\sigma_z} \qquad (3.9)$$

Where q is the inverse penetration depth for the 2D problem. Eq. 3.9 is an ordinary differential equation and is easily solved as:

$$\Theta(k,\omega) = C_1 \, sinh(qz) + C_2 \, cosh(qz) \qquad (3.10)$$

$$f(k,\omega,z) \equiv -\sigma_z \frac{\partial \Theta(k,\omega)}{\partial z} = -C_1 q \sigma_z cosh(qz) - \sigma_z C_2 q \, sinh(qz) \qquad (3.11)$$

Where f is the heat flux in Hankel-Fourier space in the z direction, and C_1 and C_2 are constants. In order to solve for these constants, we begin with the top surface (transducer). Here we define the function we are measuring in our experiment, the surface temperature, which in Hankel-Fourier space is $\Theta(k,\omega,z=0) = \Theta_{z=0,layer\,1}(k,\omega) = \Theta_{0,1}(k,\omega)$. We also define the function corresponding to our known pump heating input, $f(k,\omega,z=0) = f_{0,1}(k,\omega)$. Using these definitions, we solve for the constants in Eq. 3.10 and Eq. 3.11 at the top surface (z=0) to find,

$$C_1 = \Theta_0(k,\omega) \qquad (3.12)$$

$$C_2 = \frac{-f_0(k,\omega)}{q\sigma_z} \qquad (3.13)$$

We can now reformulate the problem within the transducer layer as the following eigenvalue problem

$$\begin{bmatrix} \Theta_{L_1,1} \\ f_{L_1,1} \end{bmatrix} = M_1 \begin{bmatrix} \Theta_{0,1} \\ f_{0,1} \end{bmatrix} \qquad (3.14)$$

$$M_1 = \begin{bmatrix} cosh(qL_1) & -\frac{1}{q\sigma_z} sinh(qL_1) \\ -\sigma_z q \, sinh(qL_1) & cosh(qL_1) \end{bmatrix} \qquad (3.15)$$

Where L_1 is the thickness of the transducer as defined in Figure 3.2. This formulation of the problem remains unbounded, however, as we do not have an expression for the flux and temperature at the bottom of layer 1 (the transducer). We must require, however, that the heat flux at the bottom of layer 1 must be equivalent to the heat flux at the top of layer 2 (the sample). The boundary conductance between the two layers can then be added to relate the two temperatures across the interface to one another. This is to say,

$$f_{L_1,1} = f_{L_1,2} = G(\Theta_{L,1} - \Theta_{L,2}) \qquad (3.16)$$

or,

$$\begin{bmatrix} \Theta_{L_1,2} \\ f_{L_1,2} \end{bmatrix} = \begin{bmatrix} 1 & 1/G \\ 0 & 1 \end{bmatrix} \begin{bmatrix} \Theta_{L_1,1} \\ f_{L_1,1} \end{bmatrix} \qquad (3.17)$$

Additionally, we know that the eigenvalue problem for layer 2 (the sample) can be formulated identically to that for layer 1, such that

$$\begin{bmatrix} \Theta_{L_1+L_2,3} \\ f_{L_1+L_2,3} \end{bmatrix} = M_2 \begin{bmatrix} \Theta_{L_1,2} \\ f_{L_1,2} \end{bmatrix} \quad (3.18)$$

$$M_2 = \begin{bmatrix} cosh(qL_2) & -\frac{1}{q\sigma_z} sinh(qL_2) \\ -\sigma_z q\, sinh(qL_2) & cosh(qL_2) \end{bmatrix} \qquad (3.19)$$

Where the material properties in M_2 now correspond to those for the sample. This can be repeated for any number of layers in the experimental sample geometry, until the heat flux and temperature at the bottom of the last layer is compared to those at the top of the transducer as follows:

$$\begin{bmatrix} \Theta_S \\ f_S \end{bmatrix} = M_S M_{S-1} \cdots M_1 \begin{bmatrix} \Theta_{0,1} \\ f_{0,1} \end{bmatrix} = \begin{bmatrix} A & B \\ C & D \end{bmatrix} \begin{bmatrix} \Theta_{0,1} \\ f_{0,1} \end{bmatrix} \quad (3.20)$$

Where the subscript S denotes the bottom of the last layer (either the substrate or the sample if it is much thicker than the penetration depth), and A, B, C, and D contain all of the thermal properties for the materials in the sample.

In the FDTR experiment, the surface temperature is measured and the surface heat flux is known to be

$$I(r) = \frac{2A_o}{\pi w_0^2} e^{\frac{-2r^2}{w_0^2}} \qquad (3.21)$$

where A_0 is the absorbed power from the laser pump and I is the radiant flux from the laser. This assumes a Gaussian laser spot on the transducer surface. In Hankel-Fourier space Eq. 3.21 is:

$$f_{0,1} = I(k) = \mathcal{H}_0\{I(r)\} = \frac{A_o}{2\pi} e^{\frac{-k^2 w_0^2}{8}} \qquad (3.22)$$

Finally, since the thermal wave incident on the surface decays rapidly within the sample/substrate, we can assume that the bottom layer is semi-infinite, or that $f_S = 0$. This yields the following solution of Eq. 3.20 for the surface temperature in Hankel-Fourier space:

$$C\Theta_{0,1} + Df_{0,1} = f_S = 0 \Rightarrow \Theta_{0,1} = -\frac{D}{C} f_{0,1} \qquad (3.23)$$

Taking the inverse Hankel transform of Eq. 3.23 returns the surface temperature in Fourier space (the frequency domain).

$$\theta(r) = \int_0^\infty k\, J_0(kr) \left(-\frac{D}{C}\right) \left(\frac{A_o}{2\pi}\right) e^{\frac{-k^2 w_0^2}{8}} dk \qquad (3.24)$$

In order to express this surface temperature in an equivalent fashion as is measured by the Gaussian probe beam sampling the surface, we take the weighted average of the surface temperature with the probe lineshape:

$$H(\omega) = \int_0^\infty \frac{2}{\pi w_1^2} e^{\frac{-2r^2}{w_1^2}} 2\pi r\theta(r)\, dr = \frac{A_o}{2\pi}\int_0^\infty k\left(-\frac{D}{C}\right) e^{\frac{-k^2(w_0^2+w_1^2)}{8}}\, dk \qquad (3.25)$$

where $H(\omega)$ is the frequency response of the sample as measured by the probe. The simplification provided is accomplished by switching the order of integration and invoking the definition of a Hankel transform as provided in Eq. 3.7. It is worth noting that all of the thermal properties of the materials in the sample are isolated within $(-D/C)$ in Eq. 3.25.

Experimentally, we measure the thermoreflectance of the transducer rather than the actual surface temperature, so the real frequency response differs somewhat from the measured frequency response. Fortunately, as has been discussed in depth elsewhere, the thermal system that describes FDTR can be treated as a linear and time invariant system as long as the power input remains relatively low and the transducer exhibits thermoreflectance (temperature and reflectivity are directly proportional to one another)[12]. Assessing the validity of this assumption is addressed in the following sections, but as long as this assumption holds the connection between the measured and real frequency responses is simply,

$$Z(\omega) = \beta Q_{pump} Q_{probe} H(\omega) \quad (3.26)$$

where $Z(\omega)$ is called the transfer function, β is the coefficient of thermoreflectance of the transducer, and Q is the absorbed laser power of the sample by the pump/probe lasers. $H(\omega)$ represents the complex temperature response of the sample to the modulated heat flux. Therefore, the phase response discussed above is simply the argument of the

frequency response. Assessment of the phase response removes the need to precisely measure the coefficient of thermoreflectance and the absorbed pump/probe powers, simplifying the analysis considerably.

3.3.2 Developing an in intuition for thermal phase response

Although it is not necessarily intuitive from Eqs. 3.25 & 3.26 what form the phase response of the surface temperature should take, or how changes in the thermal properties of the sample influence it, some intuition can be drawn from consideration of several simple limiting cases. For simplicity, we consider the case of a single-layered system in which the pump and probe beams are approximately equal. For such a case it is instructive to think of the experiment as probing the competition between two diffusive processes, the dissipation of the thermal wave in the solid (governed by the thermal diffusivity, α) and the effective diffusivity imposed by the surface heat flux. The latter can be defined via the characteristic length of the heat flux (the heater size, w_0) and the characteristic timescale of the modulation ($1/\omega$), yielding ${w_0}^2\omega$ as the diffusivity corresponding to the surface heat flux. This can be thought of as an expression of the thermal stress placed on the material by the surface modulation. The ratio between these two diffusivities then describes the sample's ability to mitigate said stress:

$$B_T \equiv \frac{{w_0}^2\omega}{\alpha} \qquad (3.27)$$

where B_T is an arbitrarily named dimensionless number describing this ratio. It should be noted that although this description has been developed with FDTR in mind, it is applicable when describing any 1D experiment with a finite heater sinusoidally modulating the

surface temperature of a solid. Furthermore, it should be noted that we could have arrived at the same expression by recognizing that when B_T=1 Eq. 3.27 is analogous to Eq. 3.4, with the natural length scale of the system defined so as to isolate a characteristic frequency.

We see from Eq. 3.27 that when the thermal properties of the solid and geometry of the heater are constant, B_T is essentially a measure of how high the frequency is for the experiment. Thus, we can use Eq. 3.27 to define limits for the solutions given in the preceding section.

At the limit of large and small B_T (and thus, frequency), the expression given for the surface temperature in the frequency domain (Eq. 3.25) reduces to:

$$H(\omega) = \frac{A_o}{2\sqrt{\pi} w_0 \sigma_z} \qquad \omega \sim B_T \ll 1 \qquad (3.28)$$

$$H(\omega) = \frac{A_o}{\pi {w_0}^2 \sqrt{i\omega} \sqrt{\rho c \sigma_z}} \qquad \omega \sim B_T \gg 1 \qquad (3.29)$$

Eq. 3.28 is essentially the DC limit of the frequency response, and as a result it is intuitive that $H(\omega)$ is independent of ω at this limit. Additionally, since in the limit of low frequency B_T is also necessarily small, we can say that this behavior results from the thermal dissipation within the sample being extremely fast relative to the heating input. It is intuitive, then, that the argument of Eq. 3.28 is 0º, as an effectively instantaneous sample response should correspond to 0º phase lag. Similarly, it is intuitive that solids with larger thermal diffusivities reach this DC limit at higher frequencies. Finally, it should be noted that the constant value associated with Eq. 3.28 is physically an estimation of the steady state (DC) temperature rise due to the heating input. This estimation will be used

throughout the subsequent sections of the dissertation to confirm minimal sample heating during data acquisition.

Eq. 3.29 represents the high frequency limit of the response function, wherein the thermal dissipation within the solid is much slower than the heating input. At this limit we see that the surface temperature is solely dependent on the thermal effusivity ($\sqrt{\rho c \sigma_z}$) of the sample. At such high heating frequencies, the sample is effectively nondissipative, and thus we expect that the phase lag should no longer be changing as a function of frequency. Indeed, the argument of Eq. 3.29 is constant at 45º, a result that is directly analogous to the well-known Warburg impedance.

Although none of the experimental data collected through this dissertation behaves precisely according to the limits described above for a 1-D single layer system, as boundary conductances and multilayer thin film geometries complicate the analysis, the driving principles that shift relative phase lag for more or less diffusive samples as a function of frequency remain crudely true, and serve as a useful tool for conceptualizing collected data.

3.4 Finite Element Solution for the Frequency Response in FDTR

In the previous section the link between thermal waves and thermal properties were established via an established heat transfer model. This model will be critical later when fitting experimental results, and is fairly routine to implement via numerical integration. In order to better understand the model, however, we utilized COMSOL Multiphysics

software to numerically solve the partial differential equation given in Eq. 3.5 directly, subject to the same boundary conditions and symmetry considerations as provided in section 3.4. While solutions for large equilibration times (> 5 pump heating/cooling cycles) were not computationally feasible, early time results are useful in aiding the development of a conceptual representation of the experiment.

A semi-infinite slab of fused silica was used as the substrate in the COMSOL simulation, with a thin (200 nm) gold transducer atop it as in a typical experimental sample. Given the mesh size, such a thin transducer is effectively just a boundary conductance in the simulation. The simulations provided real space 3D temperature distributions at each time point. The time steps taken by the software are in dimensionless time, scaled such that 10 data points are obtained per heating cycle of the pump. The results of this simulation are, naturally, exactly as expected from the relationships given in the previous section. Axial temperature, shown in Figure 3.3, tapers off as predicted by Eq. 3.4.

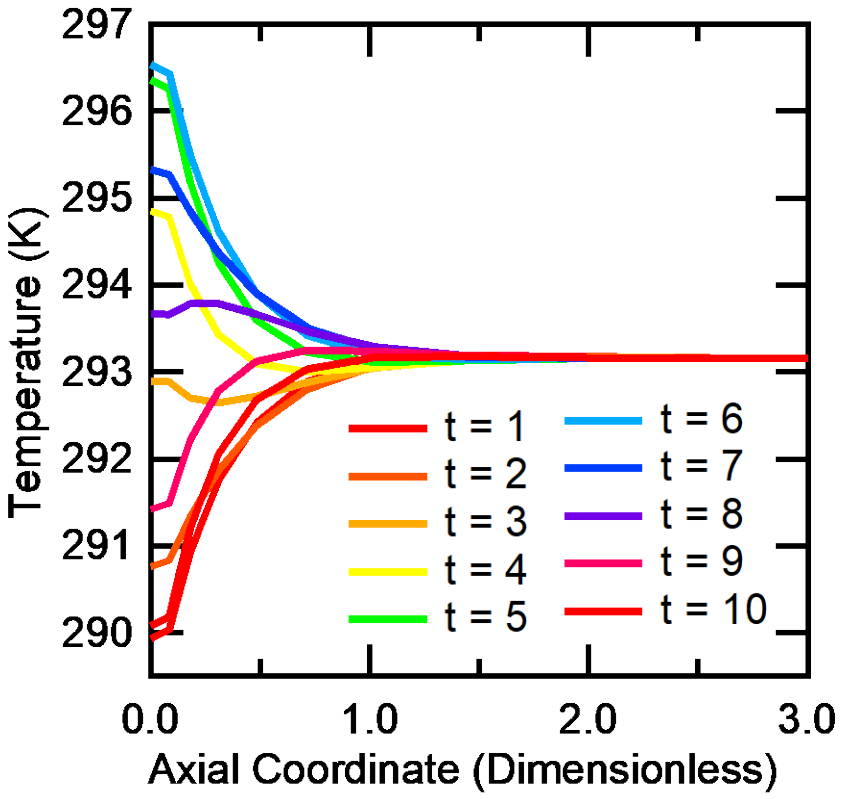

Figure 3.3 Axial temperature (r=0) as a function of dimensionless depth. The real space coordinate is normalized by the penetration depth calculated by Eq. 3.4 for fused silica at the simulation frequency (10 kHz). Time coordinate is scaled such that 10 temperature points constitutes one complete heating cycle.

As expected, as the thermal wave penetrates into the solid the temperature modulations decrease in magnitude. The heating envelope is almost completely bound within a single penetration depth, highlighting the sensitivity of the measurement to the sample of interest. Additionally, we see that throughout the heating cycle the axial coordinate also oscillates around the steady state temperature (here very near room temperature), as is intuitive.

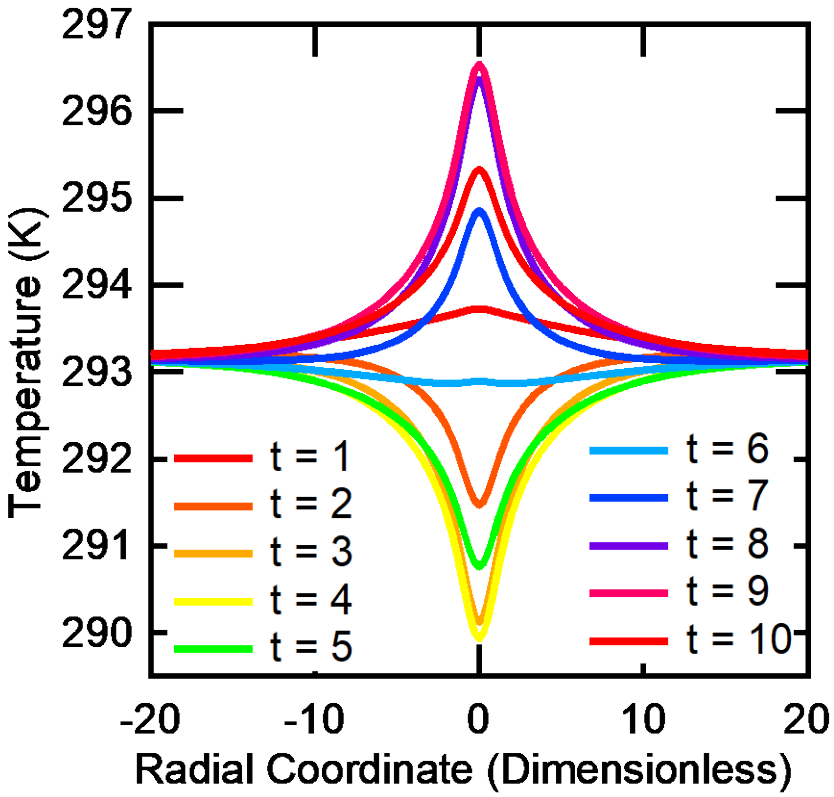

Figure 3.4 Radial surface temperature (z=0) distribution. The real space coordinate is normalized by the pump spot size typical to the experimental apparatus used. Simulation frequency is 10 kHz. Time coordinate is scaled such that 10 temperature points constitutes one complete heating cycle. A higher frequencies or sample thermal conductivities, this distribution tightens in space.

At the transducer surface, the temperature is also seen to oscillate as expected (Figure 3.4), with lateral spread directly proportional to the thermal conductivity of the sample also as is readily expected. Monitoring the temperature at the center of the coordinate system r=0, z=0, sheds light on the relationship between this intuitive behavior and the FDTR measurement, which is directly cataloging the frequency response that corresponds to this very oscillation. Figure 3.5 shows how the surface temperature oscillates in time at different heating frequencies. It is readily apparent that both the amplitude and the

relative phase of the surface temperature oscillations change as a function of frequency. In fact, both of these values decrease as a function of frequency. At very low heating frequencies, the phase of the response is almost identical to that of the heater. We see now that this intuitively results from the difference in the length of dimensionless time corresponding to a given frequency. At 10 kHz, the time for a full oscillation is a full order of magnitude longer than for 100 kHz, effectively allowing the sample more time at lower frequencies to respond to the incident heating flux without as significant a phase penalty. This also explains why more conductive samples tend to have lower phase lag at comparable frequencies, as these materials have a faster response time (a lower thermal impedance) than more insulating materials.

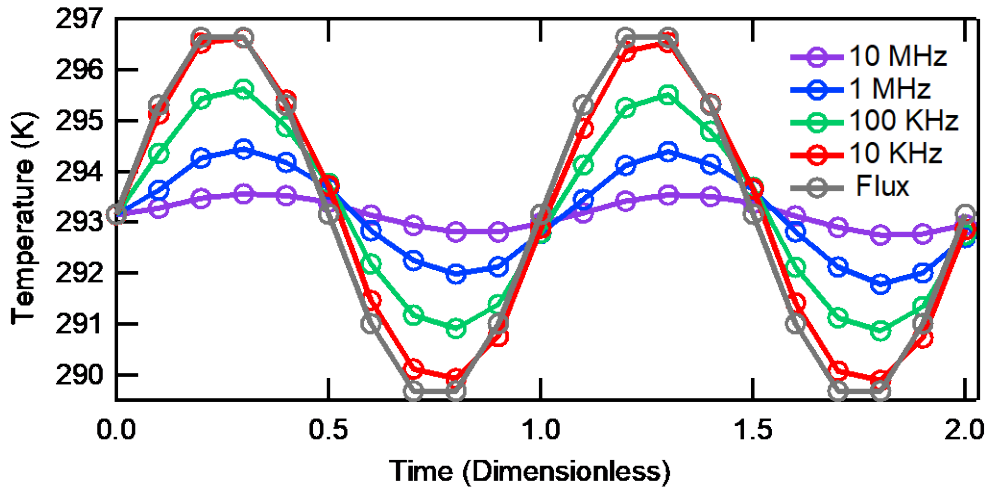

Figure 3.5 COMSOL calculated surface temperature oscillations (at z = 0, r = 0) as a function of dimensionless time. The flux is plotted on a different axis as it has no meaningful temperature associated with it. Its presence is entirely for comparison of the relative phase of the frequency response at different heating fluxes

3.5 Experimental Implementation

3.5.1 Optical Layout

The FDTR experimental setup built for carrying out the work presented in this dissertation is illustrated schematically in Figure 3.6. Low noise continuous wave 488 nm and 532 nm diode lasers (both Coherent Sapphire 200 CDRH laser systems) are employed as the pump and probe, respectively. The latter was chosen to optimally leverage the high coefficient of thermoreflectance of the gold transducer at 532 nm. Wavelength-specific optical isolators are used to prevent backscattered light from entering the laser cavities. The intensity modulation of the pump beam required for the experiment is achieved using an electro-optic modulator (EOM), which is driven by an electronic signal amplified from an arbitrary waveform generator. For experimental simplicity and minimal harmonic noise, sine waves with 1 Vpp are fed via the signal generator to the EOM driver. The now-modulated pump beam is then split via a 10:90 non-polarizing cube beam splitter. The lesser portion of the split pump is sent along a path including a micrometer driven translation stage to a Si fixed gain detector. This signal is sent to the lock-in amplifier as the reference waveform. The larger portion of the split pump is reflected off of a dichroic and sent through the microscope objective to be reflected off of the sample (coated with a Au transducer). The laser spot is Gaussian and oscillates in intensity according to the waveform driving the EOM, successfully implementing the periodic heat flux necessary for the technique.

The probe light is sent through a half waveplate into a polarizing beam splitter (PBS). The reflected light is sent through a quarter waveplate before passing through the dichroic.

The use of the PBS and the waveplates allows for efficient separation of the modulated and unmodulated probe light, since light that has reflected off of the sample surface will have a different polarization from that just downstream of the optical isolator. The waveplates can be fin adjusted to optimize reflection of light heading to the sample and signal passed through the PBS post-sample. The laser spots are aligned collinearly following the dichroic, such that the probe monitors the thermoreflectance of roughly the same area that is heated by the pump. After reflection from the sample, the now modulated probe light is collected by the objective and sent back down its original laser path to the PBS. Due to the polarization shift mentioned above the modulated probe light now passes through the PBS before being aligned into a Si fixed gain detector. The signal measured by this photodetector is sent to the signal input on the lock-in amplifier, which then determines the relative phase lag of the signal modulation from the reference. Importantly, the reference and signal arms must be as nearly matched in path length as possible, so as to avoid an absolute phase lag between the sample and the reference line regardless of the sample.

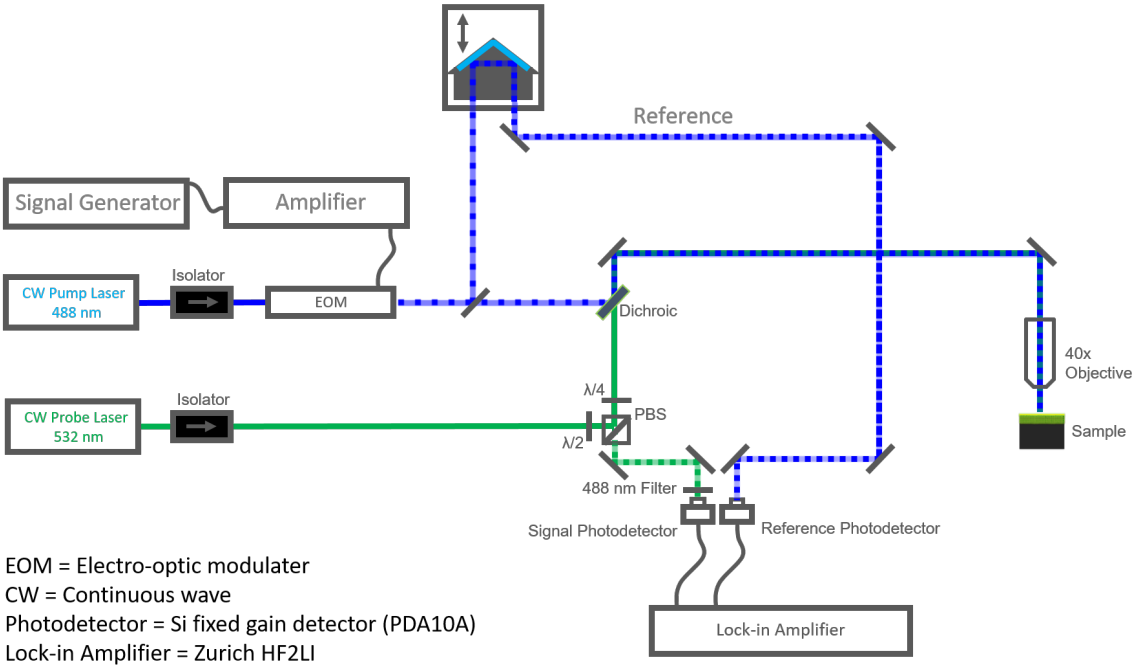

Figure 3.6 Schematic of the optical table layout for FDTR as built by the author. Colored lines indicate the path of the laser light, with the colors corresponding to those of the pump (blue) and probe (green). When dashed, the lines represent intensity modulated light. Isolators are wavelength specific optical isolators. EOM is a Conoptics model 350 EOM that modulates the intensity of the pump laser light. Amplifier is an analog Conoptics model 25A EOM driver that amplifies a 1 Vpp signal from the signal generator and sends it to the EOM to drive operation. PBS = polarizing beam splitter cube. λ/2 and λ/4 are half and quarter wave plates. 488 nm filter selectively blocks stray pump laser light. Dichroic passes 532 nm laser light and reflects 488 nm light, 40x objective (Nikon 40x S Plan Flour) focuses and collects collinear pump/probe laser light to/from sample in backscattering geometry. Si fixed gain detectors measure path-matched reference and signal modulations, which are detected via Lock-in detection and sent to a personal computer via USB.

3.5.2 Alignment of the setup

Facile alignment of the FDTR setup described in section 3.3.1 is aided by several key considerations, each of which affects the quality/reliability of the data obtained in the experiment. First is alignment into the microscope objective, misalignment of which will lead to lower signal collection, misshapen laser spots, and frequently noncollinear beams. It is recommended that during alignment, of the system, the pump and probe laser are separately aligned to be collinear *before* being aligned into the objective. Then, two additional mirrors along the laser path following the mirrors used to separately adjust the pump and probe laser positions can be used to precisely align the combined beam into the microscope objective. Care must be made here to ensure that the lasers are entering the objective at normal incidence. This can be easily tested by rotating the microscope focus through the focal plane to see if there is asymmetry or drift in the center of the laser spots during the movement of the objective. As is usually the case, iterative alignment is typically necessary to obtain optimal spot quality.

As mentioned in the previous section, a significant consideration when setting up the instrument is maintaining matched path lengths between the reference and signal arms of the layout. Specifically, the path traveled by the reference portion of the pump beam must be equivalent to the path length that the pump travels from the nonpolarizing beam splitter cube to the sample in addition to the path traversed by the probe light after reflecting off of the sample. Since the waves are finally mixed in the lock-in amplifier, even the phase lag induced by the detectors and the length of the BNC cables used to send the signal/reference waves to the lock-in must be included in this measurement. Any delay between these two paths will lead to an additional fixed relative time lag for the signal

measured during the experiment. This time delay corresponds to successively larger measured phase lag at higher pump modulation frequencies, which would have to be measured and subtracted as a linear background from all data collected.

Instead, the path signal and reference path lengths were matched by a temporary adjustment of the FDTR layout, the result of which is shown schematically in Figure 3.7. The probe laser is turned off and the dichroic is replaced with a partial mirror (80:20) and a mirror is placed on the sample stage. When the path lengths are perfectly matched, such an arrangement should lead to a measured phase lag of < 0.01º at 1 MHz. In principle this alignment now only needs to be done once when the layout is established.

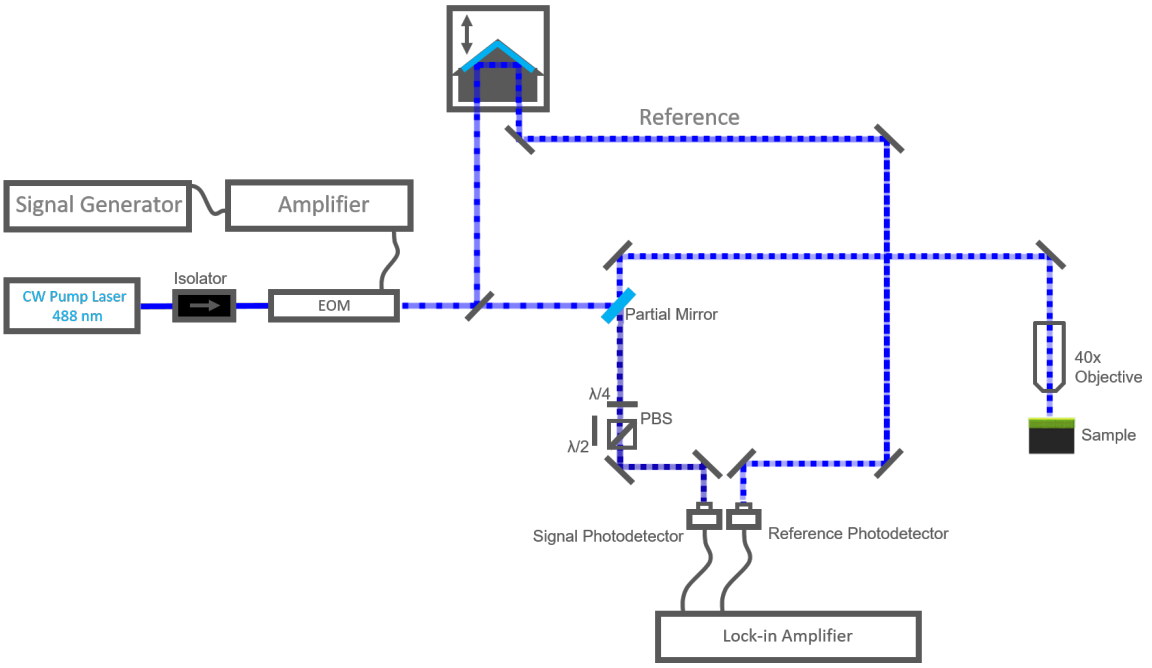

Figure 3.7 Layout of the optical table when the probe laser is turned off and the dichroic is replaced with a partial mirror for absolute phase calibration. All other optics/equipment are as defined previously.

3.5.3 Data Acquisition

Although the operating power for the lasers used is relatively high (200 mW), the surface temperature oscillation required for a reliable/physically meaningful must be relatively small. Additionally, the steady state temperature rise of the sample should be minimized as much as possible to avoid beam damage and maintain experimental integrity. To this end, a variety of neutral density filters are used to control the power of the reference, pump, and probe beam lines. Typical laser powers (as measured by a power meter at the sample stage) are ~250-300 μW, but higher powers can and typically must be used for more conductive samples (> 1 W/mK).

Similarly, the spot sizes of the pump/probe lasers must be carefully controlled to maximize signal while also probing the dynamics of interest. The spot sizes represent the relevant length scale for the radial component of heat transfer during an FDTR measurement, and as a result control of the spot size can sensitively probe axial, radial, or mixed transport. For instance, if the spot size is larger than the axial penetration depth at a given frequency, then the pump laser can be treated as a 1D plane heating source and the axial component can be ignored. Similarly, when the radial length scale is much smaller than the axial penetration depth, the radial component of heat transport plays a significant role and cannot be ignored. For our experiments, typical spot sizes of ~1.2 μm were found to maximize signal at the laser powers while remaining within the axial (1D) transport regime. In practice, the spot size must be measured during each individual data acquisition run, which is accomplished through the use of a CCD camera.

The phase response of the sample was measured using a Zurich HF2LI lock-in amplifier. This instrument sensitively detects small harmonic oscillations in electrical signals (in this case provided from the signal collected at the photodetectors). Operation was frequency locked using the output from the reference photodetector, but not phase-locked of course as this is the parameter we expect to monitor. During a data acquisition run, a Labview vi on a personal computer connected to both the lock-in amplifier and the signal generator was implemented. This vi was used to control both the lock-in detection settings and the signal generator waveform settings. In a typical instance of data acquisition, the phase response is measured by sweeping the modulation frequency fed to the EOM from 100 kHz – 1 MHz and cataloging the measured phase lag at each frequency. This frequency range was chosen due to both the lock-in/EOM operating windows and a relevant span of penetration depths for sensitive thermal property measurement (submicron penetration depths for all perovskite samples).

3.5.4 Lock-in Detection and Measurement of Phase Response

As mentioned previously, a Lock-in amplifier was used to experimentally measure the frequency response via the transfer function, $Z(\omega)$ as in Eq. 3.26, corresponding to the small sample-induced modulation within the probe laser. To accomplish this the lock-in amplifier mixes the collected signal with two reference waves that are 90 out of phase with one another, yielding an in-phase (X) and out-of-phase (Y) voltage that correspond to the real and imaginary components of $Z(\omega)$. Typical data for this raw measurement is shown below in Figure 3.8. The real and imaginary components are then easily converted to relative phase lag ($\emptyset$) via

$$\emptyset = \tan^{-1}\frac{Im\{Z(\omega)\}}{Re\{Z(\omega)\}} = \tan^{-1}\frac{Y}{X}$$

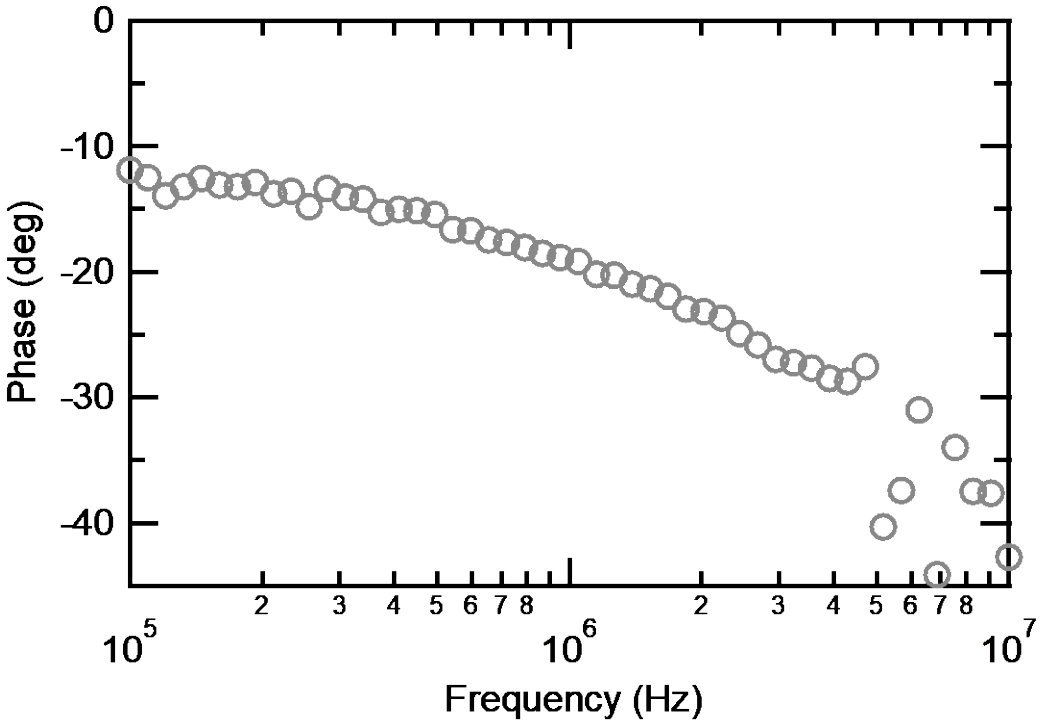

Figure 3.8. An example dataset collected for a fused silica sample, showing a typical phase response The singular outliers are resonances corresponding to the photodetectors used, and do not typically affect the results of a measurement, especially when at high frequencies.

3.5.4 External Measurement of Relevant Parameters

Since the measured phase response is sensitive to so many external parameters, such as the laser spot sizes, material thermal properties and transducer thickness, reliable extraction of the sample thermal conductivity is most easily obtained by measurement of as many of these other parameters as possible. To this end, we measure all external parameters pertaining to the heat transfer analysis of the experiment when not known. The thickness of the transducer was measured with stylus profilometry, and when necessary thin films of sample material were measured using AFM. Both of these

techniques offer precision (~ 1 nm) such that their uncertainty need not be considered in the heat transfer analysis. The heat capacity of the sample, when not previously measured, was separately measured with differential scanning calorimetry (DSC), a standard technique for such a measurement and frequently used in conjunction with FDTR. The sample mass density is also readily measured with x-ray diffraction for all 2D lead halide perovskites. The spot size of the lasers remains as the most sensitive complicating factor in analyzing our data. To best address this, we measured the spot size before each acquisition using a CCD camera. As can be seen in Figure 3.8, the spots are well fit by Gaussian lineshapes, so extraction of the beam waist is uncomplicated. The resolution of the CCD, however, limits the resolution of spot and places an inherent uncertainty on all measurements that is the largest source of error in the measurement.

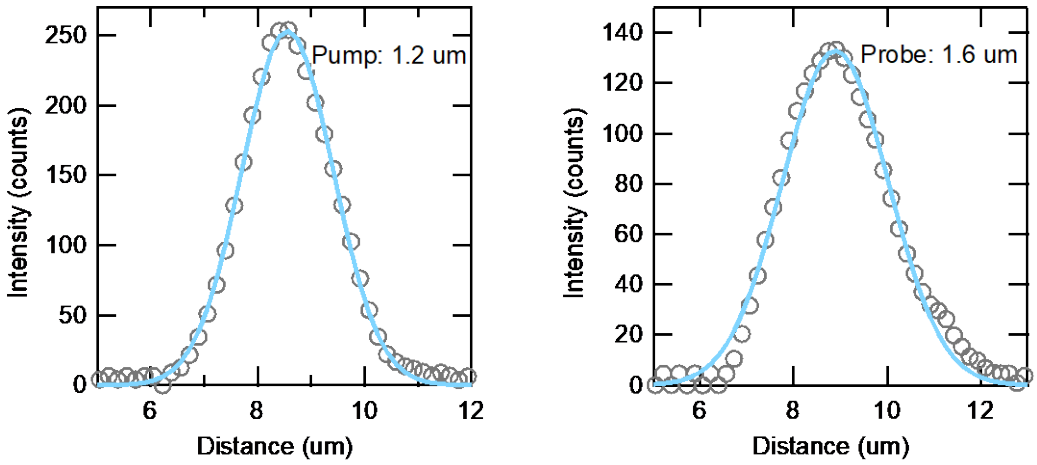

Figure 3.8 Pump (left) and probe (right) laser spots as measured by CCD (grey markers) and fit by a Gaussian lineshape (blue). Images collected by CCD are isotropic, thus a line scan as above is sufficient to measure the spot size within the resolution of the camera.

3.5.5 Data fitting procedure and parameter extraction

The analytical representation of the FDTR experiment reviewed in section 3.3 is based on the same heat transfer model for analysis posed originally by Cahill, and used ubiquitously since then with respect to TDTR/FDTR measurements of effective/diffusive thermal conductivities[6,7,9,12]. Many other models have been posed as potentially superior in directly capturing nonequilibrium transport behavior evident in FDTR experiments without the use of an effective thermal conductivity, but such models typically apply to much higher heating frequencies and with respect to far more conductive samples, and so fall outside the scope of this dissertation.[10,11] In order to extract an effective thermal conductivity of a macroscopic solid such as a 2D lead halide perovskite crystal, Fourier's law and thus the Cahill model remain sufficient. This model was fit to the experimentally measured phase response (phase lag vs. frequency) using a nonlinear least squares Levenberg-Marquardt algorithm. During fitting, the laser spot size was allowed to vary within experimental error and the thermal conductivity was allowed to vary by an order of magnitude from an initial guess. Convergence was repeatable and only sensitive to the initial guess when such a guess was much lower or higher (>80%) than the measured value for the conductivity. In these instances, the residual of the fit was much worse and so the algorithm was re-run with more stringent bounds on the conductivity. The uncertainty of the measurement was determined by evaluating the absolute change in measured thermal conductivity for the maximum variance of the spot size within the resolution of the CCD. Typical uncertainties are ~ 10 %, in line with other FDTR measurements previously reported.[13,14]

3.5.6 Demonstration of Instrument Capability

Using the fitting procedure described in the previous section to fit data collected using the setup and acquisition settings given in the preceding sections, data was obtained for several thermal conductivity standards as a means of assessing the capabilities of the system. Standards were bulk solids purchased from MTI with known thermal and material properties. Thermal evaporation was used to apply the gold transducer film (~100 nm thick). Figure 3.9 and Table 3.1 show the results of our system match up extremely well with the known properties of these materials. Furthermore, the efficacy of FDTR in measuring the thermal conductivity of these solids enumerates the usefulness of the technique across a broad range of variously conducting samples.

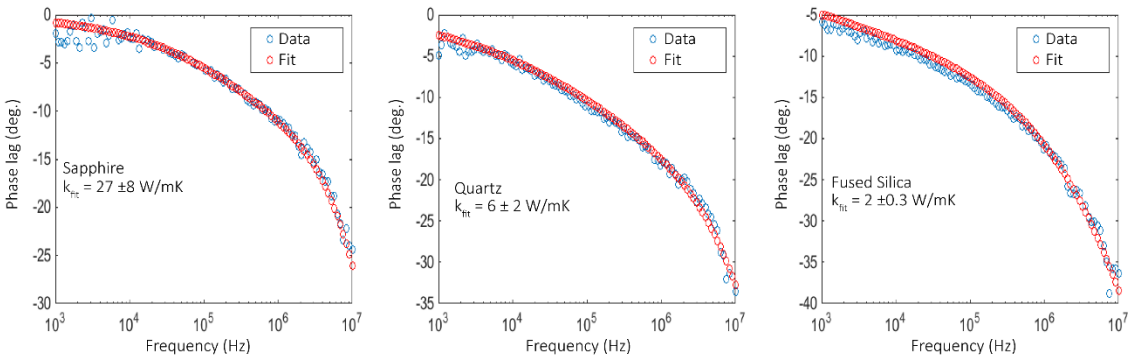

Figure 3.9. Data and numerical fits for three standard solid materials. Reported values for the thermal conductivity each of these standards is: Sapphire (25.1 W/mk), Quartz (6.1 W/mK) and Fused Silica (1.84 W/mK). Spot sizes were all ~ 1 µm, the tranducer thickness was measured to be 113 nm.

As an additional check on the capabilities of the system, we measured the thermal conductivity of lead sulfide (PbS) quantum dot (QD) thin films, a well-studied nanomaterial

whose thermal conductivity is well established[13,15]. We synthesized the PbS QDs via a previously established method from our research group, identical to those used by Liu et al[15,16]. The density and heat capacity of the QD solid was assumed to be consistent with that previously reported, as the QD preparation is the same and these properties both depend exclusively on the relative mass fractions of the organic and inorganic components within the thin film, which is well controlled by synthesis.[17] The thickness of the QD films was measured via AFM. From these results, as seen in Figure 3.10a, the established trend of increasing thermal conductivity as a function of QD diameter in addition to the absolute values of the thermal conductivities themselves are as measured previously (Figure 3.10b).

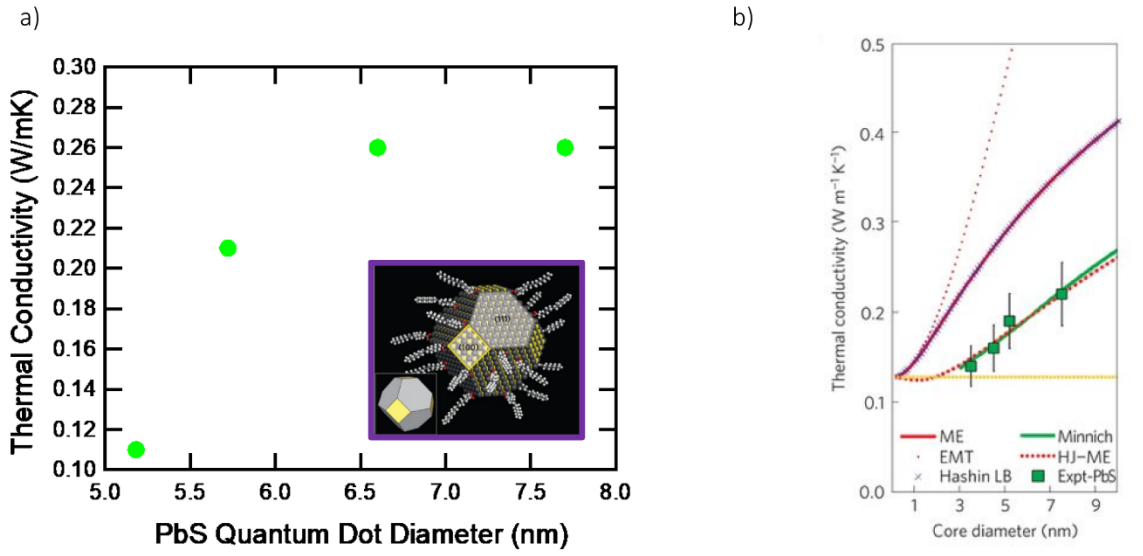

Figure 3.10. Thermal conductivity of PbS QD thin films. (a) measured thermal conductivity of quantum dot thin films with varying diameter. Inset, model of a single PbS QD, reproduced from[18]. (b) Previously measured thermal conductivity of PbS QD thin films (green squares) by Ong, et al. Reproduced from[13].

3.6 References

(1) Cahill, D. G.; Ford, W. K.; Goodson, K. E.; Mahan, G. D.; Majumdar, A.; Maris, H. J.; Merlin, R.; Phillpot, S. R. Nanoscale Thermal Transport. *J. Appl. Phys.* 2003, *93* (2), 793. https://doi.org/10.1063/1.1524305.

(2) Cahill, D. G.; Braun, P. V.; Chen, G.; Clarke, D. R.; Fan, S.; Goodson, K. E.; Keblinski, P.; King, W. P.; Mahan, G. D.; Majumdar, A.; Maris, H. J.; Phillpot, S. R.; Pop, E.; Shi, L. Nanoscale Thermal Transport. II. 2003–2012. *Appl. Phys. Rev.* 2014, *1* (1), 011305. https://doi.org/10.1063/1.4832615.

(3) Cahill, D. G. Thermal Conductivity Measurement from 30 to 750 K: The 3ω Method. *Rev. Sci. Instrum.* 1990, *61* (2), 802. https://doi.org/10.1063/1.1141498.

(4) Brites, C. D. S.; Lima, P. P.; Silva, N. J. O.; Millán, A.; Amaral, V. S.; Palacio, F.; Carlos, L. D. Thermometry at the Nanoscale. *Nanoscale* 2012, *4*, 4799. https://doi.org/10.1039/c2nr30663h.

(5) Capinski, W. S.; Maris, H. J.; Ruf, T.; Cardona, M.; Ploog, K.; Katzer, D. S. Thermal-Conductivity Measurements of GaAs/AlAs Superlattices Using a Picosecond Optical Pump-and-Probe Technique. *Phys. Rev. B* 1999, *59* (12), 8105–8113. https://doi.org/10.1103/PhysRevB.59.8105.

(6) Cahill, D. G. Analysis of Heat Flow in Layered Structures for Time-Domain Thermoreflectance. *Rev. Sci. Instrum.* 2004, *75* (12), 5119–5122. https://doi.org/10.1063/1.1819431.

(7) Schmidt, A. J.; Cheaito, R.; Chiesa, M. A Frequency-Domain Thermoreflectance Method for the Characterization of Thermal Properties. *Rev. Sci. Instrum.* 2009, *80*, 3–8. https://doi.org/10.1063/1.3212673.

(8) Rosencwaig, A.; Opsal, J.; Smith, W. L.; Willenborg, D. L. Detection of Thermal Waves through Optical Reflectance. *Appl. Phys. Lett.* 1985, *46* (11), 1013–1015. https://doi.org/10.1063/1.95794.

(9) Yang, J.; Maragliano, C.; Schmidt, A. J. Thermal Property Microscopy with Frequency Domain Thermoreflectance. *Rev. Sci. Instrum.* 2013, *84* (May 2015). https://doi.org/10.1063/1.4824143.

(10) Wilson, R. B.; Cahill, D. G. Anisotropic Failure of Fourier Theory in Time-Domain Thermoreflectance Experiments. *Nat. Commun.* 2014, *5*, 5075. https://doi.org/10.1038/ncomms6075.

(11) Regner, K. T.; McGaughey, a. J. H.; Malen, J. a. Analytical Interpretation of Nondiffusive Phonon Transport in Thermoreflectance Thermal Conductivity Measurements. *Phys. Rev. B* 2014, *90*, 064302. https://doi.org/10.1103/PhysRevB.90.064302.

(12) Schmidt, A. J.; Chen, X.; Chen, G. Pulse Accumulation, Radial Heat Conduction, and Anisotropic Thermal Conductivity in Pump-Probe Transient Thermoreflectance. *Rev. Sci. Instrum.* 2008, *79* (11), 114902. https://doi.org/10.1063/1.3006335.

(13) Ong, W.; Rupich, S. M.; Talapin, D. V; McGaughey, A. J. H.; Malen, J. a. Surface Chemistry Mediates Thermal Transport in Three-Dimensional Nanocrystal Arrays. *Nat. Mater.* 2013, *12* (5), 410–415. https://doi.org/10.1038/nmat3596.

(14) Elbaz, G. A.; Ong, W.-L.; Doud, E. A.; Kim, P.; Paley, D. W.; Roy, X.; Malen, J. A. Phonon Speed, Not Scattering, Differentiates Thermal Transport in Lead Halide Perovskites. *Nano Lett.* 2017, *17* (9), 5734–5739. https://doi.org/10.1021/acs.nanolett.7b02696.

(15) Liu, M.; Ma, Y.; Wang, R. Y. Modifying Thermal Transport in Colloidal Nanocrystal Solids with Surface Chemistry. *ACS Nano* 2015, *9* (12), 12079–12087. https://doi.org/10.1021/acsnano.5b05085.

(16) Weidman, M. C.; Beck, M. E.; Hoffman, R. S.; Prins, F.; Tisdale, W. a. Monodisperse, Air-Stable PbS Nanocrystals via Precursor Stoichiometry Control. *ACS Nano* 2014, *8* (6), 6363–6371. https://doi.org/10.1021/nn5018654.

(17) Weidman, M. C.; Yager, K. G.; Tisdale, W. A. Interparticle Spacing and Structural Ordering in Superlattice PbS Nanocrystal Solids Undergoing Ligand Exchange. *Chem. Mater.* 2015, *27*, 474–482.

(18) Weidman, M. C.; Smilgies, D. M.; Tisdale, W. A. Kinetics of the Self-Assembly of Nanocrystal Superlattices Measured by Real-Time in Situ X-Ray Scattering. *Nat. Mater.* 2016. https://doi.org/10.1038/nmat4600.

Chapter 4 – Ballistic Phonon Transport and Diffuse Interface Scattering in 2D Lead Bromide Perovskites

The basis of this chapter has been submitted as:

N. S. Dahod, W. Paritmongkol, W. A. Tisdale, “Tunable Ballistic Transport and Diffuse Interface Scattering Drive Thermal Transport in Hybrid Layered Two-Dimensional Lead Bromide Perovskites”

4.1 Introduction

Unlike the conventional semiconductors they seek to replace, bulk HOIPs are characterized by ultralow thermal conductivities (0.34-0.73 W/mK), which are up to two orders of magnitude lower than those for traditional semiconductors.[1–4] The thermal conductivity of a solid is a macroscopic property defining the spatial temperature gradient developed in a material in response to the absorption of a heat flux. Thus, a lower thermal conductivity implies a larger temperature gradient is produced in a material for a unit of absorbed heat. Put differently, a solid with a large thermal conductivity can dissipate a relatively large quantity of heat without a significant rise in temperature. The microscopic mechanism by which this macroscopic temperature gradient is established poses a deeper question, one that can only be understood by careful analysis of the heat carriers in the material.

While in metals and other semiconductors with relatively large electron mobilities and free-carrier concentrations electrons can help establish thermal equilibrium, in bulk HOIP solids phonons (quantized lattice vibrational waves) are exclusively responsible for the measured thermal conductivities.[1] From kinetic theory, the phonon thermal conductivity can be expressed in terms of the product of the mean-free path (Λ, MFP), group velocity (v), in addition to the heat capacity (C) of the phonons responsible for heat transport ($k = \frac{1}{3}Cv\Lambda$). Preliminary reports have identified that the ultralow measured thermal conductivities likely stem from a combination of factors such as low phonon group velocities and high anharmonic scattering between phonon modes associated with the lead-halide lattice and the small organic cation enclosed within it.[2,5–9] The elastic softness of HOIPs corresponds to lower sound speeds of acoustic phonons, the longer wavelength

vibrations responsible for thermal conductivity in conventional semiconductors.[10] Additionally, the presence of a high density of low frequency optical phonons that couple anharmonically with these acoustic modes via multiphonon scattering processes leads to very short estimated MFPs in HOIP solids (~1 nm).[5] Other studies, however, suggest that the MFP of phonons may be much longer and contend that the phonon speeds are exclusively responsible for the ultralow thermal conductivities of HOIPs.[2]

Although 2D LHPs are derived from their bulk counterparts, their natural structure more closely resembles that of inorganic superlattices, multilayer periodic stacks of ultrathin bulk semiconductor films. In many ways, 2D LHPs present as idealized superlattices, with atomically abrupt interfaces between layers, minimal thickness variation throughout the structure, and exceptional long-range order. In contrast, unlike all inorganic superlattices 2D LHPs are composed of phases with a large acoustic impedance mismatch and which are bound to one another by weaker hydrogen bonding interactions. It should be noted, however, that the impedance mismatch in 2D LHPs is far lower than for other organic-inorganic hybrids, due to the relative softness of the perovskite subphase. Inorganic superlattices showcase a variety of unique phenomena related to phonon transport, such as extreme suppression of thermal conductivity due to the added thermal boundary resistance between each film in addition to wave-like phonon transport in which collective vibrations of the entire superlattice structure are largely responsible for thermal energy transport.[11–16] In the latter scenario, the wave nature of bulk phonons is maintained and the material can be treated as its own bulk solid with distinct diffusive phonons, whereas for the former the transport behaves as described by ballistic (minimally scattered) phonons within each sub-layer that scatter exclusively with the boundaries between layers.

To our knowledge, only one early study of phonon transport properties of 2D LHPs exists at present. Guo et al. probed the existence and coherence time of coherent longitudinal acoustic phonons of the entire 2D LHP multi-layer structure, determining that for MAPbI-based 2D LHPs such modes exist but travel much slower and with far shorter coherence times than observed for the bulk perovskite.[17] These results suggest the possibility that such modes may contribute to thermal conductivity in much the same way as observed in inorganic superlattices. But, due to the likely significant anharmonic interaction between the organic and inorganic subphases this contribution may be weak or altogether negligible, a crossover well established for a variety of inorganic superlattices.[14,18–20]

In pursuit of clarifying these questions as to how thermal energy is dissipated in 2D LHPs and how suppressed the thermal conductivity is relative to the already ultralow value measured for bulk HOIPs, we investigate the thermal transport properties of a variety of PbBr based 2D LHPs. We report measurements of the heat capacity and thermal conductivity of 2D $(C_xH_{2x+1}NH_3)_2[MAPbBr_3]_{n-1}PbBr_4$ perovskites at room temperature as a function of both the octahedral layer thickness of the perovskite layer (n = 1,2,3) and the organic spacer chain length (x=4,5,6,7,8) using differential scanning calorimetry (DSC) and frequency domain thermoreflectance (FDTR) respectively. We observe ultralow thermal conductivities (0.18 – 0.51 W/mK) for all 2D LHPs studied, which corresponds to minimal suppression of thermal conductivity with respect to the bulk. The thermal conductivity is found to increase monotonically as a function of both the octahedral layer thickness and the organic chain length. We invoke a thermal conductivity model derived using the Boltzmann transport equation for multilayer structures that exhibit ballistic transport with diffuse interface scattering to understand the origins of these trends, and suggest that thermal transport in the 2D LHPs studied is determined by interface scattering and the

periodicity of the nanostructure rather than the thermal conductivity within either bulk phase. Our results indicate the potential for independently tuning the thermal conductivity to be higher than that observed in the bulk via organic spacer chemistry while also shedding light on relevant phonon transport pathways in 2D LHPs.

4.2 Results and Discussion

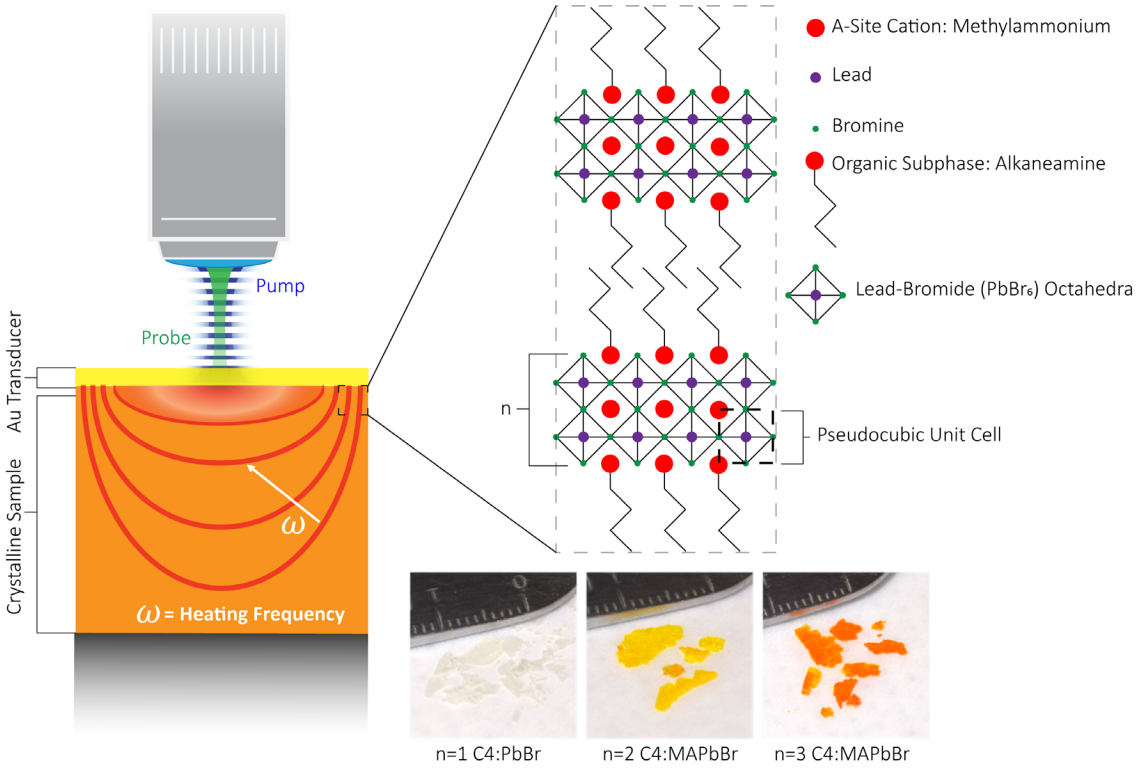

Figure 4.1. *Left*: Schematic of Frequency Domain Thermoreflectance (FDTR) measurement, in which two coaxially aligned lasers are focused through a microscope objective and reflected off of a gold (Au) thin film transducer, which has been exogenously deposited atop a solid sample of interest (here small 2D LHP crystals). The pump laser sinusoidally heats the transducer and thus the sample, and the corresponding modulations in the reflected probe intensity inform on heat transport in the sample. The pump modulation frequency, ω, directly determines the penetration depth (δ) of the heating in the measurement according to the scaling relationship $\delta \sim \sqrt{\alpha/\omega}$ where α is the thermal diffusivity of the solid. Thus higher modulation frequencies correspond to shallower heating depths. These frequencies are controlled in the experiment to maximize sensitivity

of the signal to the sample of interest rather than the transducer or the substrate (black). *Right (top)*: Schematic of a typical n=2 2D LHP. The octahedral layer thickness, n, corresponds to the number of pseudocubic unit cells within the inorganic subphase. *Right (bottom)*: Pictures of n = 1,2,3 PbBr 2D LHPs. Although these are nanostructured materials, their macroscopic composition is as solid crystals.

FDTR is a widely utilized optical metrology technique for monitoring thermal transport in solids, small crystals, thin films, and even across molecular junctions such as self-assembled monolayers.[21–24] Herein, FDTR was implemented to analyze macroscopic 2D LHP crystals synthesized using a method published previously (Figure 4.1). All crystals were adhered to a glass substrate and coated with a thin Au film (100 nm). Briefly, two coaxially aligned lasers are focused on the sample of interest through an objective lens, one of which (pump) is intensity modulated while the other (probe) is not. Since the transducer used exhibits linear thermoreflectance at the laser wavelengths/powers employed, the intensity of the reflected probe light is modulated as the surface is heated by the oscillating pump. The reflected probe light is separated from the pump and its phase lag across a range of pump frequencies is catalogued using a lock-in detection scheme. This frequency response is fit to a solution of the diffusion equation for the system geometry in order to extract the thermal conductivity.[25] In order to obtain reliable measurements of the thermal conductivity, the transducer thickness, laser spot size, and heat capacity are measured separately using profilometry, a CCD camera, and DSC respectively.

4.2.1 Quasi-Ballistic Thermal Transport in 2D LHPs

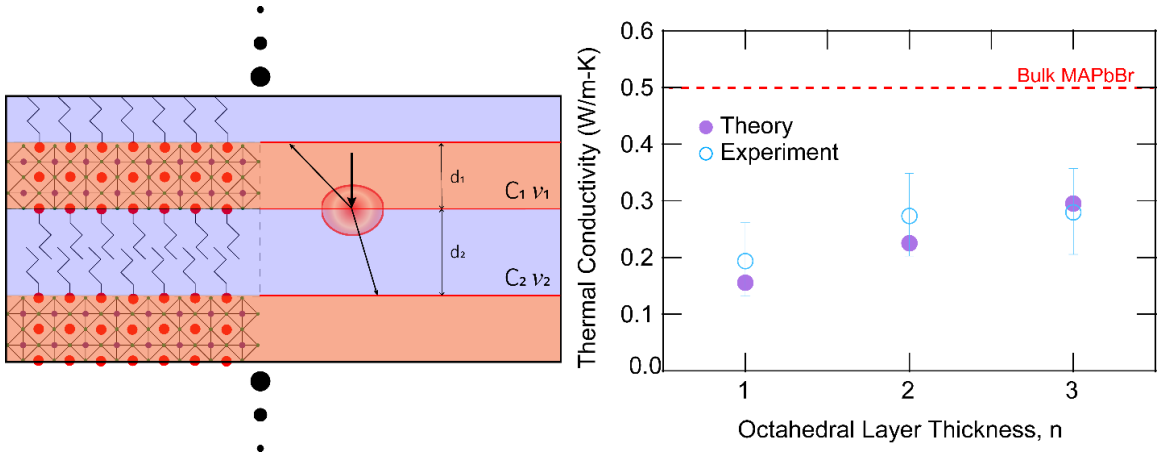

Figure 4.2. *Left*: Schematic of 2D LHP and approximation of it as a periodic multilayered nanostructure. Parameters used to approximate each layer are shown within their respective shaded region, and correspond to the layer thickness (d), volumetric heat capacity (C) and sound velocity (v). Black arrows show phonon transport as represented by model in Eq. 4.1. Phonons move via ballistic transport through each layer and scatter diffusely (without memory) at the interfaces. *Right*: Measured thermal conductivity using FDTR for n = 1 BAPbBr and n = 2,3 BA:MAPbBr 2D LHPs at room temperature (open circles) and via the theoretical model in Eq. 4.1.

At room temperature, the thermal conductivity of PbBr 2D LHPs utilizing butylamine as an organic spacer (n=1 C4:PbBr and n=2,3 C4:MAPbBr) increases monotonically with octahedral layer thickness from 0.18 to 0.26 W/mK (Figure 4.2). These values represent an approximately 50% reduction in the thermal conductivity from that measured for the bulk (0.45 W/mK) both herein and reported elsewhere in the literature.[2] While suppression of phonon transport is well documented for larger nanostructures[26], stemming from the introduction of a classical size effect limiting phonon propagation as the system boundaries approach the same length scale to the average phonon MFP, given that the layers in 2D LHPs are only several unit cells thick at most such a moderate reduction is surprising. For

instance, even if no reduction in the thermal conductivity within each subphase is assumed and a simple series-resistance model ($\frac{L_{inorganic}}{k_{inorganic}} + \frac{L_{organic}}{k_{organic}} = \frac{L_{2DLHP}}{k_{2DLHP}}$) is used to estimate the "upper limit" of the thermal conductivity for the 2D LHP in the diffusive transport regime, the low thermal conductivity of the organic subphase (~0.1 W/mK for most short-chain alkanes) actually predicts a lower thermal conductivity than measured (~0.15-0.21 W/mK for n=1-3 C4 PbBr 2D LHPs). This is especially surprising given that this representation does not account for *any* phonon scattering at the organic-inorganic interfaces between layers. Semiconducting nanocrystal arrays, as an example, show a thermal conductivity reduction of two orders of magnitude relative to their bulk values, due largely to the organic-inorganic interfaces between the semiconductor crystallites and the passivating surface ligands bound to their surface.[23]

This suggests that unlike solids composed of nanocrystal arrays and nanoscale films made from traditional semiconductors, the natural length scale of these 2D LHPs is not appreciably smaller than the average MFP of heat carrying phonons within the semiconductor phase. This is largely in agreement with several computational and experimental studies in the literature, and reinforces the contention that thermal transport in bulk HOIPs is limited by extremely short MFP phonons.[5–7] Additionally, and more importantly, since the thermal conductivity is actually higher than that predicted from traditional composite theory (even when neglecting interface resistances), the dominant phonon scattering mechanisms within the material are likely fundamentally different than in the bulk.

In order to understand the monotonic increase observed as a function of the octahedral layer thickness, we utilize an expression for the cross-plane thermal conductivity, k, of

periodic multilayer solids derived from the Boltzmann transport equation (BTE) and first reported by Chen et al. for use with all-inorganic superlattices (Eq. 4.1):

$$k = \frac{1}{2}\left(\frac{1}{C_1 v_1} + \frac{1}{C_2 v_2}\right)^{-1} \frac{(d_1 + d_2)}{2} \qquad (Eq. 4.1)$$

Where the subscripts denote the layer material, C_i is the volumetric heat capacity, v_i is the sound velocity, and d_i is the layer thickness.[11] This equation, as may be expected intuitively, bears much similarity both to the expression from kinetic theory as well as that for thermal resistors in series. Specifically, this model suggests phonons that travel an average MFP corresponding to the layer thicknesses and which experience resistance at those distances (the organic-inorganic interfaces) equal to the sum of the resistances $\left(\frac{1}{Cv}\right)$ in each layer. This precise expression is obtained for a periodic structure under the relaxation time approximation, and examines the limiting case in which layers are very thin (with periodicity comparable to the MFP of phonons within either film) and exhibit infinite long-range order with minimal defects or heterogeneities in the layers. As a result, the transport within each layer is ballistic and scattering only occurs at the interfaces, hence the series representation of the resistances. Precisely, it should be noted that this representation of the scattering at the interlayer interfaces describes fully diffuse inelastic phonon scattering, meaning that phonons scattered at an interface share no phase relationship with their previous state. This is to say, phonons leaving an interface are indistinguishable regardless of whether they are propelled by reflection or transmission. This is in contrast to specularly scattered phonons, which obey laws such as variants of Snell's law upon interaction with an interface. The diffuse scattering limit is then a very strong assumption, in that it eliminates coherent phonon transport across interfaces. Accordingly, this

assumption reflects the lowest predicted thermal conductivities for a model invoking ballistic transport and appropriately fits inorganic superlattices in which diffuse scattering is dominant at interlayer interfaces.[11]

Each of these assumptions, while limiting for most inorganic superlattices, are actually rather appropriate for 2D LHPs as described above. Importantly, as stated the assumption of very thin layers necessitates that phonon transport within each layer is completely ballistic. Given the extremely short MFPs of bulk HOIPs this seems an appropriate assumption for the inorganic phase. [5–7] Although, it should be stressed that owing to this extremely short MFP and the especially thin inorganic layer thicknesses employed by 2D LHPs, addition of another in series resistance corresponding to the diffusive $\left(\frac{d_{inorganic}}{k_{MAPbBr,bulk}}\right)$ contribution would minimally impact the predicted conductivity. Most significantly, this assumption completely replaces the ultralow thermal conductivities of liquid alkanes with significantly faster ballistic thermal transport across the molecular junctions that comprise the organic subphase. Such behavior has been observed elsewhere as ballistic heat transport across the molecular junctions within self-assembled monolayers[27,28].

We find reasonable agreement between the diffuse inelastic superlattice (DIS) model in Eq 1 and our data when using bulk values for the heat capacity and sound speed within the perovskite layers, sound speeds for bound alkanes extracted from previous studies on SAMs[29] and CdSe quantum dots[30], and heat capacities for liquid alkanes (which have comparable densities to the organic subphase in 2D LHPs). While it is routine to approximate the phonon group velocity as the sound speed, using the volumetric heat capacity can become tenuous when optical phonons that contribute significantly to the heat capacity do not contribute to thermal transport. This, however, does not seem to be the case for HOIPs since optical phonons contribute heavily to thermal conductivity.[5]

Additionally, we find that measurements of the 2D LHP heat capacity are consistent with those estimated from mass-weighted averages using these bulk values (Figure 4.3), suggesting the assumption that the nanoscale subphases retain their bulk heat capacities/sound velocities is reasonable. Such observations have been observed for other composite nanomaterials such as quantum dots, wherein the vibrational density of states (vDOS) of the nanomaterial is simply the sum of the vDOS of the organic (ligand) and inorganic components.[23]

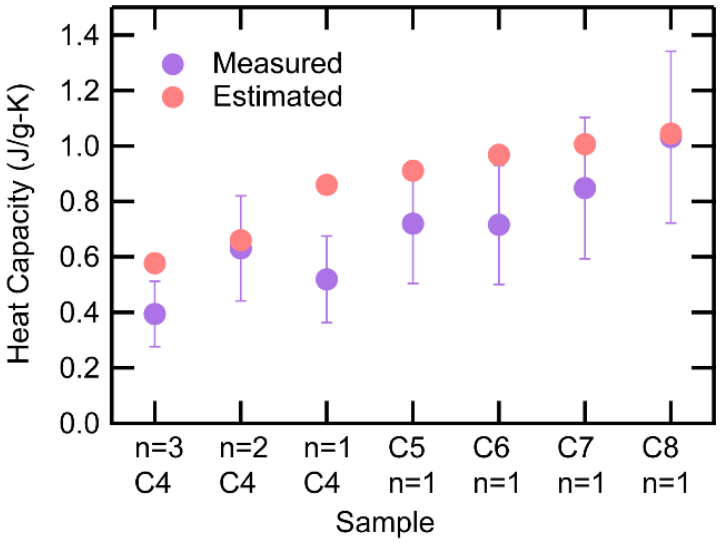

Figure 3. Experimentally (via DSC) measured (purple) values for the specific heat of 2D LHPs with various organic spacer molecules (chain length C) and octahedral layer thicknesses (n) roughly agree with those predicted (red) with a mass-weighted average from bulk heat capacities ($C_{2DLHP} = xC_{MAPbBr,bulk} + (1-x)C_{Alkane,bulk}$).

Increasing the octahedral layer thickness of 2D LHPs, using the DIS model, should lead to an increase in the thermal conductivity solely from the increase in the period thickness, as we observe. This is the case since the interfaces provide the same thermal resistance regardless of the octahedral layer thickness, and the phonon transport within the perovskite layer is ballistic. The latter directly requires that a thicker layer lead to a larger thermal conductivity as phonons can transport thermal energy further before scattering at

the interfaces. This also potentially explains why the increase in thermal conductivity for n=3 C4:MAPbBr is less than predicted by the DIS model, because for 2D LHPs with n>2 the perovskite layer thickness is potentially longer than the MFP of phonons moving within this phase. As a result, the decrease in measured thermal conductivity for n=3 C4:MAPbBr with respect to theory may be due to phonon-phonon scattering within the perovskite layers.

4.2.2 Engineering the Organic Spacer for Enhanced Transport

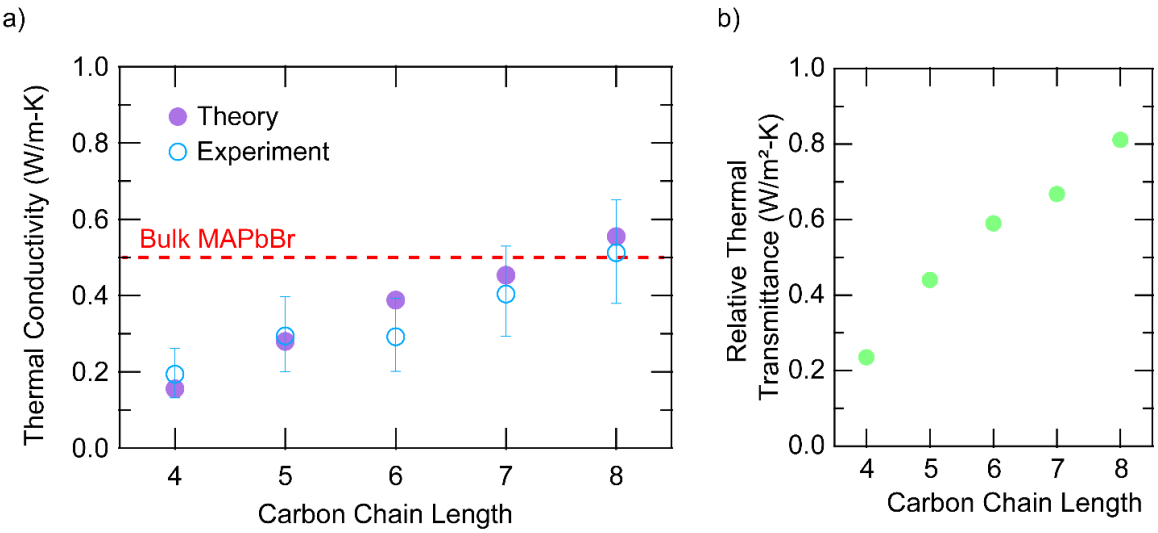

Figure 4.4. a) Measured thermal conductivity using FDTR for n = 1 PbBr 2D LHPs at room temperature (open circles) and via the theoretical model in Eq. 1 as a function of the chain length of the organic spacer subphase. b) Calculated relative thermal transmittance ratio $\left(\frac{C_2 v_2}{C_1 v_1}\right)$ for the organic spacers used in (a) based on bulk heat capacities and sound speeds measured from SAMs & alkyl ligands bound to quantum dot surfaces.

In order to probe this behavior further we measured room temperature thermal conductivities for n=1 PbBr 2D LHPs with varying organic spacer chain lengths (butylamine-octylamine). Increasing the length of the carbon chain for the organic spacers used actually

influences the thermal conductivity through several channels (Figure 4.4). Firstly, the period thickness of the organic layer naturally increases consistently with the length of the carbon chain. The sound speed through the bound organic molecule increases by a factor of three, which is much faster than the modest (< 10%) decrease in the heat capacity. Thus, the thermal transmittance ($C_2 v_2$) and the period thickness both increase with the length of the organic spacer molecule, without affecting the perovskite layer (Figure 4.4b). As before, the measured thermal conductivity is well-approximated by the DIS model, within instrumental error. Consequently, increasing the carbon chain length of the organic spacer leads to a monotonic increase in the thermal conductivity of the 2D LHP to 0.51 W/mK for n=1 C8:PbBr. That the thermal conductivity of this 2D LHP actually meets that of bulk MAPbBr, while striking, is consistent with expectations from the DIS model. In fact, this behavior highlights an interesting consequence of the DIS model, that the thermal conductivity of 2D LHPs are, in principle, not influenced by any of the mechanisms that lead to the ultralow thermal conductivity of bulk perovskites. As long as the transport within both sub-phases remains ballistic, the only determinants for thermal conductivity are the thermal transmittance ratio $\left(\frac{C_2 v_2}{C_1 v_1}\right)$ and the period thickness. Thus, for relatively large thermal transmittance of the organic sub-phase the thermal conductivity will reach a theoretical maximum dependent solely on the period thickness and the thermal transmittance of the perovskite layer. It must be stressed that such a maximum is actually far above what we probe herein, and would actually significantly exceed the thermal conductivity of bulk MAPbBr.

4.3 Conclusions

In summary, we have measured the thermal conductivity of a series of alkylammonium lead bromide 2D LHPs. We have observed ultralow thermal conductivities ranging from 0.18 – 0.51 W/mK, revealing minimal thermal conductivity suppression relative to bulk MAPbBr perovskites. The thermal conductivity is found to increase monotonically as a function of both the octahedral layer thickness and the organic chain length. Using a thermal conductivity model derived using the Boltzmann transport equation for multilayer structures that exhibit ballistic transport with diffuse interface scattering to understand the origins of these trends, we suggest that thermal transport in the 2D LHPs studied is determined by interface scattering and ballistic transport across the organic subphase rather than phonon scattering within either bulk phase. The efficacy of this model suggests that the unexpectedly high thermal conductivities of 2D LHPs relative to other hybrids and nanomaterials stem from several unique facets of this material. First, the short MFPs of bulk MAPbBr perovskites allow for atomically thin inorganic layers that do not exhibit significant suppression of phonon transport. Second, the use of molecular junctions as organic spacers incorporates a subphase that, owing to the unique ballistic transport across these junctions, is actually *more* conductive that the perovskite layer. Thus, 2D LHPs discard the phonon-scattering pathways that limit bulk perovskites in exchange for interface scattering that can be dexterously controlled via the chemistry of the organic subphase. As a result, 2D LHPs can in principle support thermal conductivities an order of magnitude higher than bulk perovskites. Or, since they may be designed to have bulk-like thermal properties as nanocomposites where advantageous and deviant behavior where bulk properties would be deleterious, these materials can be engineered to have even lower thermal conductivities (as for thermoelectric devices). Most critically, since the

thermal transport in these materials is driven by ballistic phonon conduction across the organic subphase, the inorganic subphase, and thus the prodigious optoelectronic properties of 2D LHPs, will be largely uncoupled from these pursuits in thermal engineering.

4.4 References

(1) Pisoni, A.; Jaćimović, J.; Barišić, O. S.; Spina, M.; Gaál, R.; Forró, L.; Horváth, E. Ultra-Low Thermal Conductivity in Organic–Inorganic Hybrid Perovskite CH 3 NH 3 PbI 3. *J. Phys. Chem. Lett.* 2014, *5* (14), 2488–2492. https://doi.org/10.1021/jz5012109.

(2) Elbaz, G. A.; Ong, W.-L.; Doud, E. A.; Kim, P.; Paley, D. W.; Roy, X.; Malen, J. A. Phonon Speed, Not Scattering, Differentiates Thermal Transport in Lead Halide Perovskites. *Nano Lett.* 2017, *17* (9), 5734–5739. https://doi.org/10.1021/acs.nanolett.7b02696.

(3) Heiderhoff, R.; Haeger, T.; Pourdavoud, N.; Hu, T.; Al-Khafaji, M.; Mayer, A.; Chen, Y.; Scheer, H.-C.; Riedl, T. Thermal Conductivity of Methylammonium Lead Halide Perovskite Single Crystals and Thin Films: A Comparative Study. *J. Phys. Chem. C* 2017, *121* (51), 28306–28311. https://doi.org/10.1021/acs.jpcc.7b11495.

(4) Ge, C.; Hu, M.; Wu, P.; Tan, Q.; Chen, Z.; Wang, Y.; Shi, J.; Feng, J. Ultralow Thermal Conductivity and Ultrahigh Thermal Expansion of Single-Crystal Organic–Inorganic Hybrid Perovskite CH 3 NH 3 PbX 3 (X = Cl, Br, I). *J. Phys. Chem. C* 2018, *122* (28), 15973–15978. https://doi.org/10.1021/acs.jpcc.8b05919.

(5) Gold-Parker, A.; Gehring, P. M.; Skelton, J. M.; Smith, I. C.; Parshall, D.; Frost, J. M.; Karunadasa, H. I.; Walsh, A.; Toney, M. F. Acoustic Phonon Lifetimes Limit Thermal Transport in Methylammonium Lead Iodide. *Proc. Natl. Acad. Sci.* 2018, *115* (47), 11905–11910. https://doi.org/10.1073/pnas.1812227115.

(6) Lee, W.; Li, H.; Wong, A. B.; Zhang, D.; Lai, M.; Yu, Y.; Kong, Q.; Lin, E.; Urban, J. J.; Grossman, J. C.; Yang, P. Ultralow Thermal Conductivity in All-Inorganic Halide Perovskites. *Proc. Natl. Acad. Sci.* 2017, *114* (33), 8693–8697. https://doi.org/10.1073/pnas.1711744114.

(7) Yue, S.-Y.; Zhang, X.; Qin, G.; Yang, J.; Hu, M. Insight into the Collective Vibrational Modes Driving Ultralow Thermal Conductivity of Perovskite Solar Cells. *Phys. Rev. B* 2016, *94* (11), 115427. https://doi.org/10.1103/PhysRevB.94.115427.

(8) Qian, X.; Gu, X.; Yang, R. Lattice Thermal Conductivity of Organic-Inorganic Hybrid Perovskite CH 3 NH 3 PbI 3. *Appl. Phys. Lett.* 2016, *108* (6), 063902. https://doi.org/10.1063/1.4941921.

(9) Hata, T.; Giorgi, G.; Yamashita, K. The Effects of the Organic–Inorganic Interactions on the Thermal Transport Properties of CH 3 NH 3 PbI 3. *Nano Lett.* 2016, *16* (4), 2749–2753. https://doi.org/10.1021/acs.nanolett.6b00457.

(10) Ferreira, A. C.; Létoublon, A.; Paofai, S.; Raymond, S.; Ecolivet, C.; Rufflé, B.; Cordier, S.; Katan, C.; Saidaminov, M. I.; Zhumekenov, A. A.; Bakr, O. M.; Even, J.; Bourges, P. Elastic Softness of Hybrid Lead Halide Perovskites. *Phys. Rev. Lett.*

2018, *121* (8), 085502. https://doi.org/10.1103/PhysRevLett.121.085502.

(11) Chen, G.; Neagu, M. Thermal Conductivity and Heat Transfer in Superlattices. *Appl. Phys. Lett.* 1997, *71* (19), 2761–2763. https://doi.org/10.1063/1.120126.

(12) Chen, G. Size and Interface Effects on Thermal Conductivity of Superlattices and Periodic Thin-Film Structures. *J. Heat Transfer* 1997, *119* (2), 220. https://doi.org/10.1115/1.2824212.

(13) Chen, G. Thermal Conductivity and Ballistic-Phonon Transport in the Cross-Plane Direction of Superlattices. *Phys. Rev. B* 1998, *57* (23), 14958–14973. https://doi.org/10.1103/PhysRevB.57.14958.

(14) Simkin, M. V; Mahan, G. D. Minimum Thermal Conductivity of Superlattices. *Phys. Rev. Lett.* 2000, *84* (5), 927–930. https://doi.org/10.1103/PhysRevLett.84.927.

(15) Maldovan, M. Phonon Wave Interference and Thermal Bandgap Materials. *Nat. Mater.* 2015, *14* (7), 667–674. https://doi.org/10.1038/nmat4308.

(16) Giri, A.; Braun, J. L.; Hopkins, P. E. Effect of Crystalline/Amorphous Interfaces on Thermal Transport across Confined Thin Films and Superlattices. *J. Appl. Phys.* 2016, *119* (23), 235305. https://doi.org/10.1063/1.4953683.

(17) Guo, P.; Stoumpos, C. C.; Mao, L.; Sadasivam, S.; Ketterson, J. B.; Darancet, P.; Kanatzidis, M. G.; Schaller, R. D. Cross-Plane Coherent Acoustic Phonons in Two-Dimensional Organic-Inorganic Hybrid Perovskites. https://doi.org/10.1038/s41467-018-04429-9.

(18) Ravichandran, J.; Yadav, A. K.; Cheaito, R.; Rossen, P. B.; Soukiassian, A.; Suresha, S. J.; Duda, J. C.; Foley, B. M.; Lee, C.-H.; Zhu, Y.; Lichtenberger, A. W.; Moore, J. E.; Muller, D. A.; Schlom, D. G.; Hopkins, P. E.; Majumdar, A.; Ramesh, R.; Zurbuchen, M. A. Crossover from Incoherent to Coherent Phonon Scattering in Epitaxial Oxide Superlattices. *Nat. Mater.* 2014, *13* (2), 168–172. https://doi.org/10.1038/nmat3826.

(19) Luckyanova, M. N. Coherent Phonon Heat Conduction in Superlattices. *Science.* 2012, 936–939. https://doi.org/10.1126/science.1225549.

(20) Yang, B.; Chen, G. Partially Coherent Phonon Heat Conduction in Superlattices. *Phys. Rev. B* 2003, *67* (19), 195311. https://doi.org/10.1103/PhysRevB.67.195311.

(21) Schmidt, A. J.; Cheaito, R.; Chiesa, M. A Frequency-Domain Thermoreflectance Method for the Characterization of Thermal Properties. *Rev. Sci. Instrum.* 2009, *80*, 3–8. https://doi.org/10.1063/1.3212673.

(22) Majumdar, S.; Sierra-Suarez, J. a.; Schiffres, S. N.; Ong, W.-L.; Higgs, C. F.; McGaughey, A. J. H.; Malen, J. a. Vibrational Mismatch of Metal Leads Controls Thermal Conductance of Self-Assembled Monolayer Junctions. *Nano Lett.* 2015, *15* (5), 2985–2991. https://doi.org/10.1021/nl504844d.

(23) Ong, W.; Rupich, S. M.; Talapin, D. V; McGaughey, A. J. H.; Malen, J. a. Surface Chemistry Mediates Thermal Transport in Three-Dimensional Nanocrystal Arrays. *Nat. Mater.* 2013, *12* (5), 410–415. https://doi.org/10.1038/nmat3596.

(24) Losego, M. D.; Grady, M. E.; Sottos, N. R.; Cahill, D. G.; Braun, P. V. Effects of Chemical Bonding on Heat Transport across Interfaces. *Nat. Mater.* 2012, *11* (6), 502–506. https://doi.org/10.1038/nmat3303.

(25) Cahill, D. G. Analysis of Heat Flow in Layered Structures for Time-Domain Thermoreflectance. *Rev. Sci. Instrum.* 2004, *75* (12), 5119–5122. https://doi.org/10.1063/1.1819431.

(26) Johnson, J. A.; Maznev, A. A.; Cuffe, J.; Eliason, J. K.; Minnich, A. J.; Kehoe, T.; Sotomayor Torres, C. M.; Chen, G.; Nelson, K. A. Direct Measurement of Room-Temperature Nondiffusive Thermal Transport Over Micron Distances in a Silicon Membrane. https://doi.org/10.1103/PhysRevLett.110.025901.

(27) Wang, R. Y.; Segalman, R. A.; Majumdar, A. Room Temperature Thermal Conductance of Alkanedithiol Self-Assembled Monolayers. *Appl. Phys. Lett.* 2006, *89* (17), 173113. https://doi.org/10.1063/1.2358856.

(28) Wang, Z.; Carter, J. A.; Lagutchev, A.; Koh, Y. K.; Seong, N.-H.; Cahill, D. G.; Dlott, D. D. Ultrafast Flash Thermal Conductance of Molecular Chains. *Science.* 2007, *317* (5839), 787–790. https://doi.org/10.1126/science.1145220.

(29) DelRio, F. W.; Jaye, C.; Fischer, D. A.; Cook, R. F. Elastic and Adhesive Properties of Alkanethiol Self-Assembled Monolayers on Gold. *Appl. Phys. Lett.* 2009, *94* (13), 131909. https://doi.org/10.1063/1.3111440.

(30) Lee, E. M. Y.; Mork, A. J.; Willard, A. P.; Tisdale, W. A. Including Surface Ligand Effects in Continuum Elastic Models of Nanocrystal Vibrations. *J. Chem. Phys.* 2017, *147* (4), 044711. https://doi.org/10.1063/1.4995439.

Chapter 5 – Direct Observation of Composite Vibrational Modes in 2D Lead Halide Perovskites via Low Frequency Raman Spectroscopy

The basis of this chapter has been submitted as:

N. S. Dahod, A. France-Lanord, W. Paritmongkol, J. C. Grossman, W. A. Tisdale, “On the Low Frequency Raman Spectrum of Layered Two-Dimensional Lead-Iodide Perovskites”

5.1 Introduction

The low frequency vibrational spectrum of these materials, which informs on the phonons supported by the crystal, provides useful fundamental insight into a variety of important phenomena relevant for device engineering. For example, with respect to bulk $MAPbI_3$, Raman spectroscopy is utilized to help identify localized crystallographic transformations or degradation pathways, particularly those that couple with the electronic behavior of the material[1]. Additionally, this technique provides critical corroborating details for analysis of various particle-phonon scattering processes (e.g. electron-phonon, phonon-phonon, spin-phonon), such as the energies and lifetimes of relevant optically active phonon modes[2,3]. These mechanisms are essential to developing quantitative models for energy transport in devices that incorporate these materials. This utility can be extended to include experimental verification of theoretical calculations of important relationships such as the phonon dispersion and vibrational density of states, typically through techniques such as density functional theory or molecular dynamics simulation[4–8]. Finally, for hybrid organic-inorganic materials, wherein phases of incongruous elastic properties commingle, Raman spectroscopy can help elucidate the vibrational overlap between the constituent phases. Since the inorganic component of perovskites like $MAPbI_3$ are so much heavier than the organic components these coupled inorganic-organic phonon modes are only observed at low frequencies (<150 cm^{-1}).

For bulk lead halide perovskites, the observed low-frequency Raman spectrum has been found to be particularly sensitive to the crystal structure of the material[4,6,8]. In particular, for higher temperature phases in which the translational and rotational freedom of the A-site cation is unlocked, a broad central (0 cm^{-1}) peak is observed and ascribed to the local

polar fluctuations of this cation[6]. At lower temperatures, particularly in the orthorhombic crystal phase, for which the cation is largely immobilized, well-resolved features are obtained, although in many cases these features remain dynamically broadened by local inhomogeneities in cation positioning. Nonetheless, density functional theory calculations verify that the low frequency phonon modes arise due to both lead-halide cage modes (octahedral distortions) and associated coupled movement of the organic cation.[4,7]

Layered perovskite-type compounds (sometimes called low-dimensional networked perovskites or n=1 2D LHPs), another material system analogous to 2D LHPs in which single atomic layers of BX_6 octahedra are separated by an organic sublayer have also been investigated preliminarily with Raman spectroscopy.[9–12] As for bulk perovskites, these compounds exhibit low frequency Raman-active phonon modes that are attributed to octahedral twists and distortions, which are coupled to the motions of the molecules within the organic subphase. These modes, as for bulk perovskites, are also dynamically broadened by molecular motion of the organic subphase.

In this chapter we discuss the low frequency Raman spectrum of various PbI 2D LHPs, as a function of A-site cation (MA, FA), octahedral layer thickness (n=2-4), and organic spacer chain length (butyl-, pentyl-, hexyl-). Using Density Functional Theory (DFT) calculations under the harmonic approximation for n=2 BA:MAPbI we assign several LO/TO phonon modes between 30-100 cm^{-1}, the eigendisplacements of which are analogous to that observed previously for octahedral twists/distortions in bulk MAPbI. Additionally, we suggest that further low frequency modes below this band (< 30 cm^{-1}) may be zone-folded longitudinal acoustic phonons corresponding to the periodicity of the entire layered

structure. We validate this tentative assignment in the context of all inorganic superlattices using the Rytov elastic continuum model for zone-folded dispersion in layered structures. Our results are consistent across the various 2D LHPs studied herein, with energetic shifts of optical phonons corresponding to microscopic structural differences between materials and energetic shifts of acoustic phonons according to changes in the periodicity and elastic properties of the perovskite/organic subphases.

5.2 Results & Discussion

5.2.1 Identification of Modes in the Low Frequency Raman Spectrum of n=2 BA:MAPbI

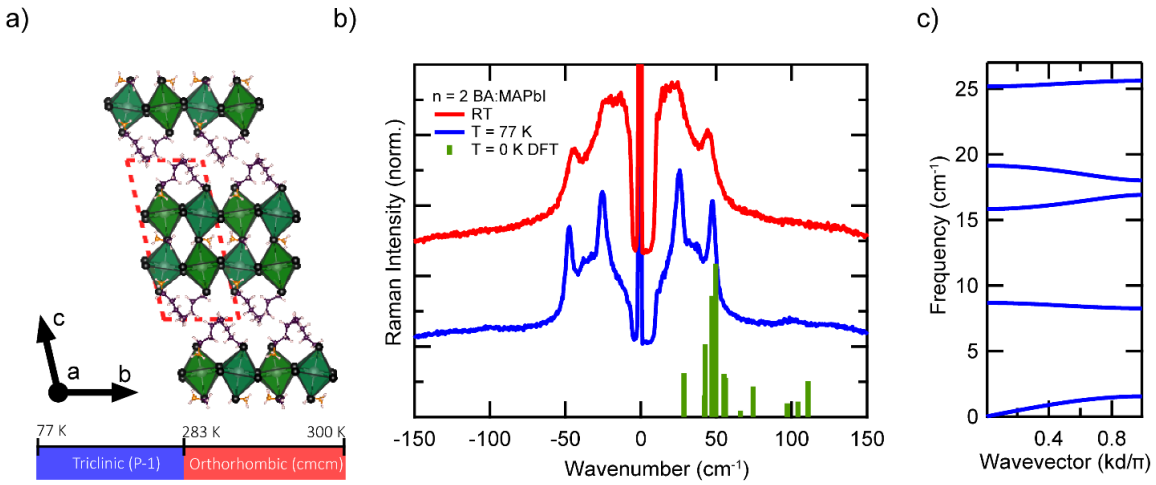

Figure 5.1. a) Space filling model extracted from single crystal X-ray diffraction for triclinic crystal structure of n = 2 BA:MAPbI and phase bar showing structural transitions and approximate transition temperatures. The red dotted line traces a single unit cell. b) Low frequency Raman spectrum at room temperature (red) and 77 K (blue). Raman frequencies and activities predicted from DFT calculations (green). c) Calculated dispersion for folded Brillouin zone from the Rytov model.

The measured Raman spectrum of n=2 BA:MAPbI perovskite crystals is shown in Figure 5.1b. At room temperature, the observed spectrum is dominated by a large peak centered at 0 cm^{-1}. Analogous to the higher temperature Raman spectra of bulk MAPbI3 perovskite, this central peak likely arises due to the presence of local polar fluctuations of the organic cations (both the A-site cations and the longer chain spacers). Specifically, interactions between the cations and the inorganic lattice, due to translation/rotation of the former, over a range of time scales (~0.3-3 ps for MA cations in MAPbI3) fast relative to the lifetimes of the Raman-active phonons leads to a broad peak in the frequency domain centered at 0 cm^{-1}.[6,13] While it is not immediately discernable which cation contributes more to the central peak observed, it is well established that at room temperature both components exhibit significant dynamic disorder.[14] Although the crystal structure of the 2D LHP is orthorhombic owing to the larger periodicity inherent in the material, the inorganic sub-lattice closely approximates that of cubic MAPbI3, leaving a cavity large enough for the MA cation to rotate. Additionally, both x-ray diffraction measurements and thermal analysis certify that the BA molecules in the organic subphase behave, analogous to self-assembled monolayers, as liquid molecules bound to a two dimensional surface. Although virtually all Raman features disappear beneath this central peak at room temperature, one mode at ~44 cm^{-1} remains visible.

In order to reduce the central peak and study the low frequency vibrational spectrum of the material, data was collected at 77 K, which is far below the freezing point of the organic subphase. At these temperatures, the crystal structure differs somewhat from that at room temperature. The 2D LHP as a whole is characterized by a lower symmetry triclinic

structure (Figure 5.1a), owing to the contraction of the organic subphase during freezing and a distortion of the inorganic sub-lattice in response. At this temperature, several phonon modes between 20-100 cm^{-1} become visible. In addition to these modes, however, the MA cation still exhibits some dynamic disorder and thus the central peak is still present in this spectrum.

First principles lattice-dynamics calculations were performed under the harmonic approximation, using the experimentally determined triclinic crystal structure as an input, in order to determine the vibrational modes of the material, the Raman intensity corresponding to each mode, and the real-space vector displacements within the crystal corresponding to each mode (see Methods section). The brightest Raman-active modes determined in this fashion were then utilized to assign the experimentally obtained spectrum at 77 K. As the calculations were performed at 0 K under the harmonic approximation, small shifts (of about 4-5 cm^{-1}) between the calculated and experimental frequencies was expected. The harmonic approximation does not consider anharmonic bond expansion at non-zero temperatures, which leads to said shifts.

We separate our discussion of the observed/calculated modes into three distinct bands: those above 50 cm^{-1}, those between 30-50 cm^{-1}, and those below 30 cm^{-1}. Above 50 cm^{-1}, one distinct mode is observed at 100 ±1 cm^{-1}. While this frequency is likely still too low for the observation of isolated vibrations within the aliphatic chains of the organic subphase, the coupling of molecular modes to inorganic vibrations in bulk $MAPbI_3$ leads to Raman active vibrations in this region.[4] Density functional theory calculations of n=2 BA:MAPbI suggest that this is indeed the case for these layered crystals as well. Experimentally, this

peak appears with relatively low intensity, in agreement with the low calculated activity of the mode, and large FWHM as a result of inhomogeneous broadening with respect to the MA cation.

Between 30-50 cm^{-1}, several Raman-active modes corresponding to octahedral twists/distortions are observed experimentally. In particular, a sharp mode at 47.5 ±0.1 cm^{-1} can be clearly resolved in addition to several overlapping peaks between 30-40 cm^{-1}. While these modes are appreciably sharper than those observed at higher frequency, they are well fit by Gaussian lineshapes, suggesting significant inhomogeneous broadening remains. This broadening could be the result of either strain-induced deformation of the inorganic lattice or a distribution of equilibrium positions with respect to the MA cation, both of which are observed via X-ray diffraction measurements.

Below 30 cm^{-1}, one prominent Raman-active vibrational mode is observed experimentally for the n=2 BA:MAPbI 2D LHPs. Interestingly, there are no corresponding bright Raman modes calculated from DFT. The energy of this mode is comparable to that observed for an octahedral twist (TO) mode in bulk cubic $MAPbI_3$, but the equivalent vibrational mode is not observed with significant Raman activity in our calculations. Our calculations do, however, reveal one mode in the vicinity of that measured experimentally, but with much lower intensity than observed. We suggest that if this calculated mode contributes to the peak observed experimentally, then it does so at a comparable intensity to the peak observed at 100 cm^{-1}. Such a peak would likely not be distinguishable atop the growing background produced by the central peak at low wavenumbers, hence we suggest an alternative vibrational mode may be responsible for this feature.

While density functional theory calculations provide deep insight into the phonon dispersion within the first Brillouin zone as determined by the crystallographic unit cell, it cannot provide insights into the effect of periodicities comparable to or longer than this. For most crystals this is largely irrelevant as no such periodicities exist, but for periodic nanostructures such as 2D all-inorganic superlattices this difference is critical to understanding the low frequency phonon dispersion (and Raman spectrum as a result). The longer cross-plane periodicity (d) introduced by the stacking of materials with differing elastic properties atop one another can lead to phonon dispersion corresponding to the "mini" Brillouin zone (with wavevector less than π/d). Within this mini Brillouin zone acoustic phonon branches are "zone-folded" and even form mini gaps in their dispersion for wave vectors that satisfy the Bragg condition. This phenomenon is analogous to the formation of electronic bandgaps for an electron in a periodic potential well (described by the Kronig-Penney model).

Additionally, because these zone-folded acoustic modes have non-zero frequency at the zone center they are optically active and can be probed with Raman spectroscopy. Such phonons are well established for various all-inorganic superlattices[15–19] and have even been observed in some organic-inorganic layered materials[20]. Finally, the longitudinal zone-folded acoustic modes for those cases wherein the interface between layers is sharp and the dispersion can be approximated as linear near the zone center can be well represented with a simple continuum model (very similar in derivation to the Kronig-Penney model) first given by Rytov:

$$cos(kd) = cos\left(\frac{\omega d_1}{v_1}\right) cos\left(\frac{\omega d_2}{v_2}\right) - \frac{1+\kappa^2}{2\kappa} sin\left(\frac{\omega d_1}{v_1}\right) sin\left(\frac{\omega d_2}{v_2}\right), \quad \kappa = \frac{\rho_1 v_1}{\rho_2 v_2}, \quad \text{(Eq. 5.1)}$$

where k is wavevector, ω is frequency, $v_{1,2}$ are sound velocities, $d_{1,2}$ are layer thicknesses, and $\rho_{1,2}$ are mass densities within each phase.

As discussed in the previous chapter, in many ways 2D LHPs exemplify an ideal superlattice, as they consist of atomically abrupt interfaces, virtually no crystalline heterogeneities (as evidenced by their well-established octahedral thickness purity), and very long-range order stemming from their growth as single crystals[14]. Importantly, though, 2D LHPs involve a significant mismatch in the elastic properties of the organic and inorganic subphases. Coherent longitudinal acoustic phonons near 0 cm^{-1} (optically inactive) have actually been observed for this variant of 2D LHPs using stimulated Brillouin scattering, although whether or not these materials exhibit zone-folding has not been discussed.[21] As a result, we suggest the use of the Rytov model for phonon dispersion within the mini Brillouin zone to describe the longitudinal acoustic (LA) phonons inherent to 2D LHPs.

Using bulk values for the sound velocity and density in the inorganic sub-lattice and those measured for SAMs and bulk liquids for the organic subphase, in addition to layer thicknesses as calculated by single crystal X-ray diffraction we calculate the zone-folded phonon dispersion for n=2 BA:MAPbI (Figure 5.1c). Unsurprisingly, owing to the low sound velocities of both subphases this dispersion is characterized by largely dispersionless branches. Additionally, the large mismatch between the acoustic impedances of the

subphases (directly calculated via κ as ~25.1) opens the calculated band gaps appreciably from those calculated for all inorganic superlattices.[16] This calculation reveals an optically active zone-folded LA phonon mode at 25.2 cm^{-1}, in excellent agreement with that observed experimentally. Thus, we tentatively assign the prominent peak at 25.2 cm^{-1} as a zone-folded LA phonon of the superlattice. It should be noted that we do not expect any higher frequency zone-folded modes to be present in our spectra, as such modes would extend beyond the first Brillouin zone of the 2D LHP. Additionally, although the Rytov dispersion suggests further zone-folded LA modes at lower frequencies, these modes are likely hidden by a combination of the optical filter used to suppress the Rayleigh line (onset at ~20 cm^{-1}) and the increasingly high intensity contribution of the central peak at lower wavenumbers. As we will show briefly, for 2D LHPs with a less influential central peak, we can resolve even these zone-folded LA phonons.

5.2.2 Altering the A-site Cation and Corroboration of Zone-Folded Acoustic Vibrations

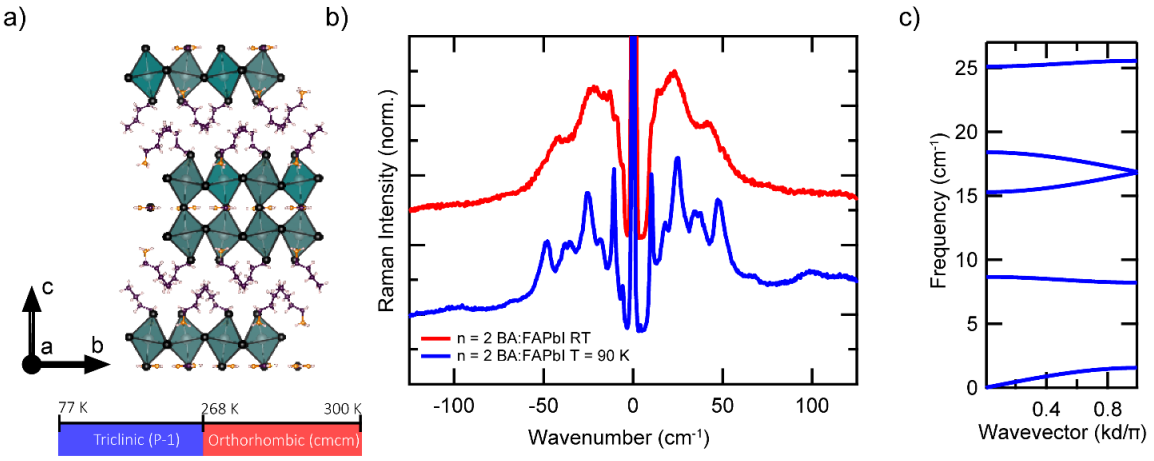

Figure 5.2. a) Space filling model extracted from single crystal X-ray diffraction for triclinic crystal structure of n = 2 BA:FAPbI and phase bar showing structural transitions and approximate transition temperatures. b) Low frequency Raman spectrum at room temperature (red) and 90 K (blue). c) Calculated dispersion for folded Brillouin zone from the Rytov model.

In order to further investigate the nature of the modes assigned above, we vary the identity of the A-site cation in the 2D LHP from MA to the larger formamidinium (FA). As for bulk lead halide perovskites, this substitution does not appreciably change the crystal symmetry. At room temperature, the organic subphase is disordered and the space group is orthorhombic. Similarly, below the 2D melting point of the organic subphase the symmetry is reduced to a triclinic P-1 cell, with ordered and oriented organic molecular chains (Figure 5.2a). One key difference between the 2D LHPs arises from the relative stiffness of the FAPbI inorganic sublattice as compared to that of MAPbI. Perovskites utilizing the large FA cation in the A-site are appreciably less stiff (lower elastic modulus) than analogous perovskites with smaller central cations.[22] This is likely because the large FA cation, which is essentially as large a cation as can be sustained by the octahedral network (quantified by a near unity Goldschmidt tolerance factor), stretches the size of the

unit cell. The longer bond lengths correspond to weaker elastic stiffness and consequently a lower sound velocity for effectively the same material density.[22,23]

Owing to their structural similarity, the room temperature low-frequency Raman spectrum of n=2 BA:FAPbI is almost identical to that acquired for n=2 BA:MAPbI (Figure 5.2b). At cryogenic temperatures, analogous peaks above 25 cm^{-1} are observed and likely correspond to the same eigendisplacements calculated for the n=2 BA:MAPbI 2D LHP above. The zone-folded LA mode, however, actually red-shifts slightly to 24.8 ±0.2 cm^{-1} from that measured for n=2 BA:MAPbI. This slight shift intuitively stems from the lower sound velocity of the FAPbI sub-lattice, a relationship that is well represented by the Rytov model, which predicts a decrease in the zone-folded LA mode by ~0.1 cm^{-1} (Figure 5.2c). The characteristic frequency of the inorganic medium, given by v_1/d_1 in Eq. 5.1, is directly proportional to the sound velocity of the material for roughly equivalent slab thicknesses. Additionally, and somewhat surprisingly, several lower frequency phonon modes are observed between 10-25 cm^{-1}. The phonon energy of these modes are all consistent with the phonon dispersion given by the Rytov model for n=2 BA:FAPbI, thus we tentatively assign all of these modes as zone-folded LA phonons as well. This agreement over several different branches of the Rytov dispersion further validates our incorporation of said model into our analysis. We attribute the appearance of these additional peaks in the FA spectrum to a decrease in the dynamic disorder exhibited by the larger, likely sterically limited, FA cation. This consequentially decreases the intensity of the central peak below 20 cm^{-1} where the optical filter begins attenuating the Raman signal, allowing for the resolution of features previously unobserved.

5.2.3 Independent Tuning of Acoustic/Optical Modes via Inorganic Layer Thickness

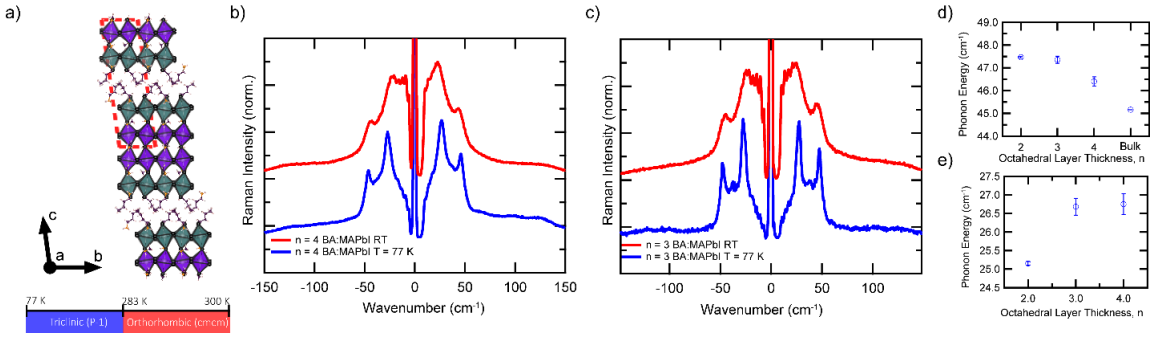

Figure 5.3. a) Space filling model extracted from single crystal X-ray diffraction for triclinic crystal structure of n = 4 BA:MAPbI and phase bar showing structural transitions and approximate transition temperatures for both n = 3 and n=4 BA:MAPbI. External octahedra are highlighted in teal while internal octahedra are highlighted in purple. The red dotted line traces a single unit cell. b) Low frequency Raman spectrum of n=4 BA:MAPbI at room temperature (red) and 77 K (blue). c) Low frequency Raman spectrum of n=3 BA:MAPbI at room temperature (red) and 77 K (blue). d) Optical phonon energy as a function of octahedral layer thickness. Bulk value is obtained from Ref. 4. e) z-f LA phonon energy as a function of octahedral layer thickness.

Increasing the PbI octahedral layer thickness, n, does not significantly impact the overall symmetry of the 2D LHP. Both n=3 and n=4 2D LHPs retain orthorhombic space groups at high temperature and low symmetry triclinic cells below the freezing point of the organic subphase (Figure 5.3a). Consequently, at all temperatures and n-values the Raman spectra remain qualitatively the same (Figure 5.3b, c). One subtle distinction arises from the presence of PbI octahedra with differing local symmetry for higher values of n. Specifically, although for n=2 all octahedra interact with the ammonium ions from both the organic spacer and MA, higher n 2D LHPs have additional “internal” octahedra that only engage in hydrogen bonding with MA. For these internal octahedra, the local environment is identical to that of bulk $MAPbI_3$. External octahedra, on the other hand, are categorized by

axial bond-length asymmetry, wherein the axial Pb-I bond lengths are distorted significantly from the values for bulk Pb-I. Since the optical phonons assigned for bulk $MAPbI_3$ previously, as well as their analogs assigned for n=2 BA:MAPbI above, are twists and distortions of presumably identical octahedra, it is expected that asymmetry therein would lead to slight changes in the phonon energies. Indeed, at cryogenic temperatures we observe slight red shifting of the prominent optical cage mode as n is increased (Figure 5.3d). This is to say, as the relative quantity of internal octahedra is increased the phonon energy shifts towards its bulk value (45 cm^{-1}).[4]

Changing the inorganic slab thickness alters the periodicity and the characteristic frequency within the Rytov model, and thus should lead to some variation of the zone-folded LA Raman features from those observed for n=2. As for the n=2 2D LHPs discussed above, higher n 2D LHPs also appear to support such zone-folded LA modes, although at increasing values of n it should be noted that as for the optical mode discussed above, the higher frequency optical modes (such as that analogous to the bulk $MAPbI_3$ observed near 26 cm^{-1}) will likely soften and begin to overlap the LA phonons. At high enough n-values, the periodicity of the 2D LHP will be too large relative to the wavelength of the phonons, and they will likely cease to be observed. This, naturally, is another expression of the tendency towards bulk properties of a nanomaterial as its characteristic size is increased relative to the relevant characteristic length of confinement. The increase in period thickness for n=3&4 BA:MAPbI leads to a reduction of the characteristic frequency, which is large enough to yield an increase in the number of branches within the mini-Brillouin zone. This additional branch intersects with the zone center at values comparable to those observed experimentally (Figure 5.3e). Interestingly, for n=3, two branches intersect the zone center at frequencies within the linewidth of the feature we have assigned as a zone-

folded acoustic phonon, implying that this feature is potentially a doublet. Observing this experimentally herein is unlikely given the inhomogeneous broadening apparent in all observed Raman features for 2D LHPs with MA A-site cations.

5.2.4 Preservation of Composite Vibrational Spectra for Different Organic Spacers

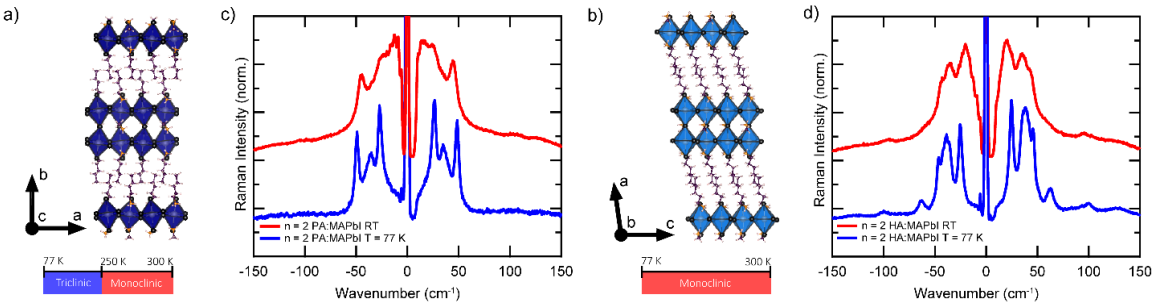

Figure 5.4. a) Space filling model extracted from single crystal X-ray diffraction for triclinic crystal structure of n = 2 PA:MAPbI and phase bar showing structural transitions and approximate transition temperatures. b) Low frequency Raman spectrum at room temperature (red) and 77 K (blue). c) Space filling model extracted from single crystal X-ray diffraction for monoclinic crystal structure of n = 2 HA:MAPbI and phase bar showing temperature invariance of crystal structure. d) Low frequency Raman spectrum at room temperature (red) and 77 K (blue).

In addition to varying the perovskite sublattice, we also synthesized 2D LHPs insulated with various organic spacer molecules. Specifically, we varied the alkyl chain length of the organic subphase from a four carbon chain (above) to five and six carbon chain alkylamines. At cryogenic temperatures (well below the freezing point of the hexyl and pentyl amine subphases), the crystal structures vary slightly from those observed for the 2D LHPs that utilize BA as an organic spacer. Rather than a triclinic space group, the hexylammonium-spaced 2D LHPs are described by monoclinic unit cells at 77 K. Additionally, since these unit

cells contain many more atoms than for triclinic n=2 BA:MAPbI, it was infeasible to carry out DFT calculations for these materials. Since the optical modes we observe in our Raman measurements are primarily inorganic perovskite cage modes, however, and given the qualitative similarity between our results for all 2D LHPs, we hypothesize that the modes we observe are analogs of those assigned above for n=2 BA:MAPbI. Interestingly, the relative intensity of the cage modes between 25-45 cm^{-1} increases significantly with the symmetry of the crystal structure, a trend which qualitatively matches that observed for bulk lead halide perovskites via DFT calculations. [4] This suggests that the increased symmetry leads to less splitting of phonon modes and thus higher Raman intensity.

Altering the chemical composition of the organic subphase naturally impacts the zone-folded LA phonons as well, which are observed for both PA and HA 2D LHPs studied herein. Changing the chain length of the organic spacer alters the density, period thickness, and the sound speed within this medium, all of which influence the phonon dispersion as modeled by Eq. 5.1. The changes in density are relatively minute and do not appreciably alter the calculated dispersion within the mini-Brillouin zone. The increases in sound velocity and period thickness, on the other hand, both compete in influencing the characteristic frequency (v_2/d_2) of the organic subphase and consequently affect the expected frequency of the LA phonons. As a result, although increasing the organic chain length from 4 to 5 carbons increases the period thickness, it also leads to a much larger increase in the sound velocity through the organic medium, hence an increase in the measured frequency of the LA mode is both calculated and observed. Further increasing the chain length to 6 carbons continues to increase the chain length but does not lead to as significant of an increase in the sound velocity, and so the measured frequency actually decreases. This agreement corroborates both our assignment of these modes as coherent

LA vibrations of the 2D LHP superlattice and also the efficacy of the Rytov model in describing the phonon dispersion that gives rise to them. It also highlights the manner in which the vibrational and structural properties of the organic subphase can uniquely control the vibrational properties of these materials without simultaneously influencing the optical properties.

5.2.5 Temperature Evolution of Raman Modes for 2D LHPs

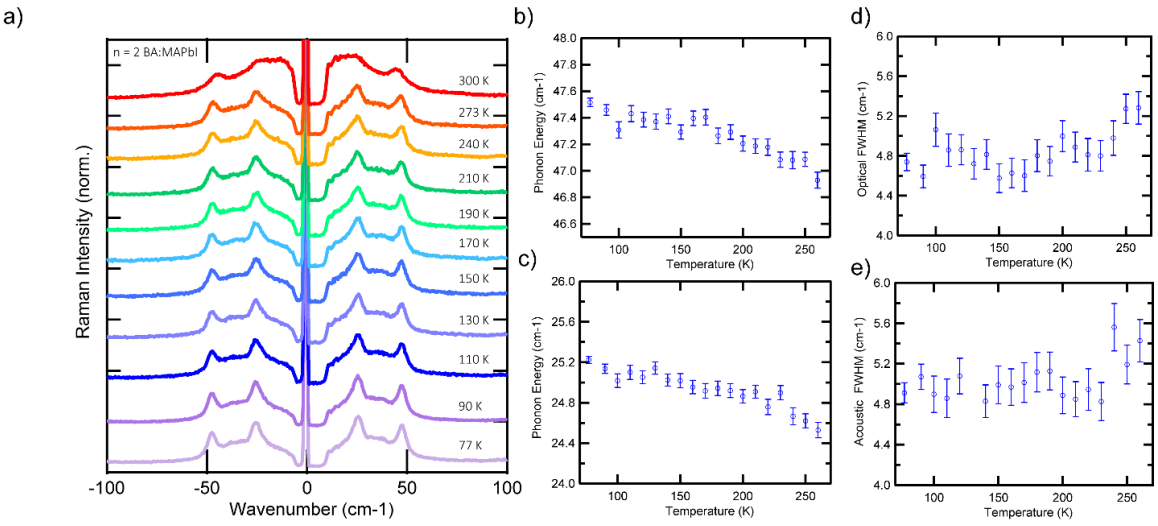

Figure 5.5. a) Low frequency Raman spectrum of n=2 BA:MAPbI at various temperatures between room temperature and 77 K. b) Phonon mode softening for primary optical mode. c) Phonon mode softening for zf-LA mode. d) Temperature dependence of FWHM for primary optical mode. e) Temperature dependence of FWHM for zf-LA mode.

Across the melting transition of the organic subphase, the phonon energies soften discontinuously and the linewidth increases dramatically; this occurs in concert with the effects of a larger central peak in the high temperature phase. Across solid-solid phase transitions, such as that observed for n=2 PA:MAPbI between 200 K and 250 K, pronounced

mode softening occurs gradually over the temperature range associated with the transition. As observed for the synthetically-controlled structural changes discussed above, in each of these cases the deviation in phonon energy is likely the result of changes in the symmetry and bond lengths of the atoms associated with said transitions.

In addition to the pronounced spectral changes observed across phase transitions within the various 2D LHPs, we also observe temperature-dependent phonon energy and linewidth shifts in the absence of such transformations (Figure 5.5). Each phonon mode discussed above exhibits the same trend, phonon mode-softening (red shift) as the temperature of the lattice is increased, along with a slight inflation of the measured peak linewidth. Mode softening with increasing temperature is a widely reported phenomenon, typically attributed to anharmonic lattice characteristics such as thermal expansion. Thermal expansion is observed via powder x-ray diffraction for 2D LHPs, and the lengthening of each bond in the lattice naturally leads to a lower force constant for each phonon mode in the Raman spectrum, hence a lower measured frequency. Within the Rytov model for the zone-folded LA phonons, this same behavior is captured via changes in the density and elastic parameters of the lattice.

The increase in linewidth as a function of temperature is somewhat unexpected, given the energy of the phonon modes studied herein are all well below k_BT. Far below k_BT, the decay of phonons into lower energy phonons ceases to become temperature dependent, and as seen for inorganic semiconductor quantum dots with organic ligands the Raman linewidth also ceases to vary as a function of temperature.[24] Lead halide perovskites, however, exhibit a significant degree of homogeneous broadening owing to the multitude of degrees of freedom available to the organic cations employed, the extent of which is temperature

dependent.[4] At higher temperatures increasing degrees of freedom for cation rotation are unlocked, leading to a wider continuum of energies distributed throughout the lattice, and thus a broader observed Raman mode. It should be reiterated, though, that our observed Raman modes are all best fit by Gaussian lineshapes, implying that inhomogeneous broadening due to the variable orientation of the different organic cations is largely responsible for the measured peak width. In the absence of a phase transition such as those described above, this broadening should not be temperature dependent.

5.3 Conclusions

In summary, we have probed the low frequency Raman spectrum of various PbI 2D LHPs, as a function of A-site cation (MA, FA), octahedral layer thickness (n=2-4), and organic spacer chain length (butyl-, pentyl-, hexyl-). We observe a broad central peak, similar to that observed for bulk perovskites, likely due to anharmonic fluctuations in the positions of the organic cations. We see that the influence of this peak decreases below the freezing point of the organic subphase, at which temperatures several sharp Raman features are distinguished. Using Density Functional Theory calculations under the harmonic approximation for n=2 BA:MAPbI we assign several LO/TO phonon modes between 30-100 cm^{-1}, the eigendisplacements of which are analogous to that observed previously for octahedral twists/distortions in bulk MAPbI. Additionally, we suggest that further low frequency modes below this band (< 30 cm^{-1}) may be zone-folded longitudinal acoustic phonons corresponding to the periodicity of the entire layered structure. We produce this tentative assignment in the context of all inorganic superlattices, and correspondingly use the Rytov elastic continuum model for zone-folded dispersion in layered structures to quantify this analogy. Our results are consistent across the various 2D LHPs studied herein, with peak shifts in optical phoons corresponding to microscopic structural differences between materials and peak shifts in acoustic phonons according to changes in the periodicity and elastic properties of the perovskite/organic subphases.

On one hand, our results indicate the similarity between 2D LHPs and their bulk counterparts, as all optical modes observed are analogs of bulk phonons, with minimal changes resulting from the additional organic cation and nanostructured length scale. This supports the hypothesis that 2D LHPs are truly hybrid materials in which the organic spacer

subphase, much like the A-site cation, does not fundamentally alter the dispersion relation of the PbI inorganic cages. Instead, the vibrational density of states for 2D LHPs more closely resembles the sum of each of these phases, as has been observed for other organic-inorganic hybrid nanomaterials.[25]

Our observation of ostensibly coherent acoustic phonons, on the other hand, suggests that although 2D LHPs are analogous to their bulk counterparts in many ways they may be capable of supporting acoustic phonons not accessible to MAPbI. These phonons may prove important for understanding a variety of phenomena related to heat transport in these nanomaterials. For instance, as has been observed for inorganic superlattices that exhibit zf-LA phonons, thermal transport in these systems may proceed by wave-like phonon transport through which these long wavelength phonons scatter off of one another without regard for the organic-inorganic interfaces that usually limit hybrid organic-inorganic nanostructured semiconductors.[26]

5.4 Methods

5.4.1 Low-Frequency Raman Spectroscopy

Raman spectra were collected using a home-built instrument described in a previous publication. Spectra were obtained in a backscattered geometry through an inverted Nikon microscope (60x, 0.6 NA objective). A 785 nm narrow-band excitation source was filtered from undesirable amplified spontaneous emission using a series of cleanup filters (laser and filters from Ondax). The Rayleigh line was minimized by passing the collected signal through a set of volume holographic grating notch filters (from Ondax) before being dispersed in a 0.5 m focal length spectrograph (SP-2500, Princeton Instruments) using a 1200 g/mm and 750 nm blaze grating, and ultimately imaged on a cooled CCD camera (Princeton Instruments Pixis). Collected spectra were fit using the multipeak fitting package in Igor Pro 6.37. A sloping Gaussian background was used to approximate the central peak beyond the optical filter, and Gaussian lineshapes were found to best fit the Raman features present in all samples. For data collected at different temperatures, the fit from 77 K was used as an initial guess for subsequent fits at higher temperatures. Data was collected at several locations along a pristine crystal in order to assure reproducibility. Errors reported represent the 99% confidence interval for the fit parameters.

5.5 References

(1) Ledinský, M.; Löper, P.; Niesen, B.; Holovský, J.; Moon, S.-J.; Yum, J.-H.; De Wolf, S.; Fejfar, A.; Ballif, C. Raman Spectroscopy of Organic–Inorganic Halide Perovskites. *J. Phys. Chem. Lett.* 2015, *6* (3), 401–406. https://doi.org/10.1021/jz5026323.

(2) Iaru, C. M.; Geuchies, J. J.; Koenraad, P. M.; Vanmaekelbergh, D.; Silov, A. Y. Strong Carrier–Phonon Coupling in Lead Halide Perovskite Nanocrystals. *ACS Nano* 2017, *11* (11), 11024–11030. https://doi.org/10.1021/acsnano.7b05033.

(3) Straus, D. B.; Hurtado Parra, S.; Iotov, N.; Gebhardt, J.; Rappe, A. M.; Subotnik, J. E.; Kikkawa, J. M.; Kagan, C. R. Direct Observation of Electron–Phonon Coupling and Slow Vibrational Relaxation in Organic–Inorganic Hybrid Perovskites. *J. Am. Chem. Soc.* 2016, *138* (42), 13798–13801. https://doi.org/10.1021/jacs.6b08175.

(4) Leguy, A. M. A.; Goñi, A. R.; Frost, J. M.; Skelton, J.; Brivio, F.; Rodríguez-Martínez, X.; Weber, O. J.; Pallipurath, A.; Alonso, M. I.; Campoy-Quiles, M.; Weller, M. T.; Nelson, J.; Walsh, A.; Barnes, P. R. F. Dynamic Disorder, Phonon Lifetimes, and the Assignment of Modes to the Vibrational Spectra of Methylammonium Lead Halide Perovskites. *Phys. Chem. Chem. Phys.* 2016, *18* (39), 27051–27066. https://doi.org/10.1039/C6CP03474H.

(5) Quarti, C.; Grancini, G.; Mosconi, E.; Bruno, P.; Ball, J. M.; Lee, M. M.; Snaith, H. J.; Petrozza, A.; De Angelis, F. The Raman Spectrum of the CH 3 NH 3 PbI 3 Hybrid Perovskite: Interplay of Theory and Experiment. *J. Phys. Chem. Lett.* 2014, *5* (2), 279–284. https://doi.org/10.1021/jz402589q.

(6) Yaffe, O.; Guo, Y.; Tan, L. Z.; Egger, D. A.; Hull, T.; Stoumpos, C. C.; Zheng, F.; Heinz, T. F.; Kronik, L.; Kanatzidis, M. G.; Owen, J. S.; Rappe, A. M.; Pimenta, M. A.; Brus, L. E. Local Polar Fluctuations in Lead Halide Perovskite Crystals. *Phys. Rev. Lett.* 2017, *118* (13), 136001. https://doi.org/10.1103/PhysRevLett.118.136001.

(7) Brivio, F.; Frost, J. M.; Skelton, J. M.; Jackson, A. J.; Weber, O. J.; Weller, M. T.; Goñi, A. R.; Leguy, A. M. A.; Barnes, P. R. F.; Walsh, A. Lattice Dynamics and Vibrational Spectra of the Orthorhombic, Tetragonal, and Cubic Phases of Methylammonium Lead Iodide. *Phys. Rev. B* 2015, *92* (14), 144308. https://doi.org/10.1103/PhysRevB.92.144308.

(8) Ivanovska, T.; Quarti, C.; Grancini, G.; Petrozza, A.; De Angelis, F.; Milani, A.; Ruani, G. Vibrational Response of Methylammonium Lead Iodide: From Cation Dynamics to Phonon-Phonon Interactions. *ChemSusChem* 2016, *9* (20), 2994–3004. https://doi.org/10.1002/cssc.201600932.

(9) Abid, Y. X-Ray and Raman Studies of the Re-Entrant Phase and Phase Transitions in the Perovskite-Type Layer Compound Bis(n-Propylammonium) Lead Tetrabromide. *J. Phys. Condens. Matter* 1994, *6* (32), 6447–6454. https://doi.org/10.1088/0953-8984/6/32/007.

(10) Couzi, M.; Daoud, A.; Perret, R. Low-Frequency Raman Spectra and Phase Transitions in Perovskite-Type Layer Compounds. (CH3NH3)2MnCl4 and (CH3NH3)CdCl4. *Phys. Status Solidi* 1977, *41* (1), 271–282. https://doi.org/10.1002/pssa.2210410133.

(11) Preda, N.; Mihut, L.; Baibarac, M.; Baltog, I.; Lefrant, S. A Distinctive Signature in the Raman and Photoluminescence Spectra of Intercalated PbI 2. *J. Phys. Condens. Matter* 2006, *18* (39), 8899–8912. https://doi.org/10.1088/0953-8984/18/39/020.

(12) Warren, R. F.; Liang, W. Y. Raman Spectroscopy of New Lead Iodide Intercalation Compounds. *J. Phys. Condens. Matter* 1993, *5* (35), 6407–6418. https://doi.org/10.1088/0953-8984/5/35/006.

(13) Bakulin, A. A.; Selig, O.; Bakker, H. J.; Rezus, Y. L. A.; Müller, C.; Glaser, T.; Lovrincic, R.; Sun, Z.; Chen, Z.; Walsh, A.; Frost, J. M.; Jansen, T. L. C. Real-Time Observation of Organic Cation Reorientation in Methylammonium Lead Iodide Perovskites. *J. Phys. Chem. Lett.* 2015, *6* (18), 3663–3669. https://doi.org/10.1021/acs.jpclett.5b01555.

(14) Stoumpos, C. C.; Cao, D. H.; Clark, D. J.; Young, J.; Rondinelli, J. M.; Jang, J. I.; Hupp, J. T.; Kanatzidis, M. G. Ruddlesden-Popper Hybrid Lead Iodide Perovskite 2D Homologous Semiconductors. *Chem. Mater.* 2016, *28* (8), 2852–2867. https://doi.org/10.1021/acs.chemmater.6b00847.

(15) Barker, A. S.; Merz, J. L.; Gossard, A. C. Study of Zone-Folding Effects on Phonons in Alternating Monolayers of GaAs-AlAs. *Phys. Rev. B* 1978, *17* (8), 3181–3196. https://doi.org/10.1103/PhysRevB.17.3181.

(16) Colvard, C.; Merlin, R.; Klein, M. V.; Gossard, A. C. Observation of Folded Acoustic Phonons in a Semiconductor Superlattice. *Phys. Rev. Lett.* 1980, *45* (4), 298–301. https://doi.org/10.1103/PhysRevLett.45.298.

(17) Colvard, C.; Gant, T. A.; Klein, M. V.; Merlin, R.; Fischer, R.; Morkoc, H.; Gossard, A. C. Folded Acoustic and Quantized Optic Phonons in (GaAl)As Superlattices. *Phys. Rev. B* 1985, *31* (4), 2080–2091. https://doi.org/10.1103/PhysRevB.31.2080.

(18) Bartels, A.; Dekorsy, T.; Kurz, H.; Köhler, K. Coherent Zone-Folded Longitudinal Acoustic Phonons in Semiconductor Superlattices: Excitation and Detection. *Phys. Rev. Lett.* 1999, *82* (5), 1044–1047. https://doi.org/10.1103/PhysRevLett.82.1044.

(19) Ibáñez, J.; Rapaport, A.; Boney, C.; Oliva, R.; Cuscó, R.; Bensaoula, A.; Artús, L. Raman Scattering by Folded Acoustic Phonons in InGaN/GaN Superlattices. *J. Raman Spectrosc.* 2012, *43* (2), 237–240. https://doi.org/10.1002/jrs.3028.

(20) Schneider, D.; Liaqat, F.; El Boudouti, E. H.; El Hassouani, Y.; Djafari-Rouhani, B.; Tremel, W.; Butt, H.-J.; Fytas, G. Engineering the Hypersonic Phononic Band Gap of Hybrid Bragg Stacks. *Nano Lett.* 2012, *12* (6), 3101–3108. https://doi.org/10.1021/nl300982d.

(21) Guo, P.; Stoumpos, C. C.; Mao, L.; Sadasivam, S.; Ketterson, J. B.; Darancet, P.; Kanatzidis, M. G.; Schaller, R. D. Cross-Plane Coherent Acoustic Phonons in Two-Dimensional Organic-Inorganic Hybrid Perovskites. https://doi.org/10.1038/s41467-018-04429-9.

(22) Ferreira, A. C.; Létoublon, A.; Paofai, S.; Raymond, S.; Ecolivet, C.; Rufflé, B.; Cordier, S.; Katan, C.; Saidaminov, M. I.; Zhumekenov, A. A.; Bakr, O. M.; Even, J.; Bourges, P. Elastic Softness of Hybrid Lead Halide Perovskites. *Phys. Rev. Lett.* 2018, *121* (8), 085502. https://doi.org/10.1103/PhysRevLett.121.085502.

(23) Fu, M.; Tamarat, P.; Trebbia, J.-B.; Bodnarchuk, M. I.; Kovalenko, M. V; Even, J.; Lounis, B. Unraveling Exciton–phonon Coupling in Individual FAPbI3 Nanocrystals Emitting Near-Infrared Single Photons. *Nat. Commun.* 2018, *9* (1), 3318. https://doi.org/10.1038/s41467-018-05876-0.

(24) Mork, A. J.; Lee, E. M. Y.; Tisdale, W. A. Temperature Dependence of Acoustic Vibrations of CdSe and CdSe–CdS Core–shell Nanocrystals Measured by Low-Frequency Raman Spectroscopy. *Phys. Chem. Chem. Phys.* 2016, *18* (41), 28797–28801. https://doi.org/10.1039/C6CP05683K.

(25) Ong, W.; Rupich, S. M.; Talapin, D. V; McGaughey, A. J. H.; Malen, J. a. Surface Chemistry Mediates Thermal Transport in Three-Dimensional Nanocrystal Arrays. *Nat. Mater.* 2013, *12* (5), 410–415. https://doi.org/10.1038/nmat3596.

(26) Yang, B.; Chen, G. Partially Coherent Phonon Heat Conduction in Superlattices. *Phys. Rev. B* 2003, *67* (19), 195311. https://doi.org/10.1103/PhysRevB.67.195311.

Chapter 6 – Outlook

Every major advance in the capabilities of optical and electronic devices has come with the aid of a clear understanding of how to mitigate the additional thermal stress associated with enhanced performance. Modern computers and smartphones are all packed tightly with electronics that would overheat and cease to function if not for many creative cooling solutions. Solar cells only absorb a small percentage of solar energy, converting much of the rest to waste heat that would quickly destroy the cell if not for efficient thermal energy dissipation within the device architecture. Additionally, thermal energy harvesting technologies such as thermoelectrics can leverage excess environmental heat to produce usable energy. All of this engineering, however, is deeply rooted in the answers to fundamental questions about how the active materials used transport heat. The scope of this dissertation has been thus to answer the first level of such questions for a particularly inviting next generation semiconductor, two dimensional layered lead halide perovskites (2D LHPs). In this pursuit, we have found that even though these materials are composed of nanostructured phases only a unit cell or a single molecule in length, they behave in a manner that can be well represented exclusively using knowledge of their bulk properties and well-established composite theories heretofore scarcely used in hybrid materials. We have shown how this knowledge allows for the prediction of near room temperature phase changes within isolated phases, which can potentially store heat during device operation. We have also shown how this knowledge can be leveraged to control which particle-like phonon scattering pathways contribute to thermal conductivity, setting new bounds on the thermal conductivity of these materials. Finally, we display how further control over these pathways may be possible via the wave-like transport of coherent phonons.

Future work must seek to test the bounds of the novel properties discussed herein. Novel organic spacer chemistries, specifically that have increased heat capacities and sound velocities relative to those studied herein, must be intelligently designed and incorporated into 2D LHPs to test the limits of thermal conductivity placed on the particle-like transport of phonons in lead bromide 2D LHP. The thermal transport behavior of lead iodide 2D LHPs, which ostensibly support coherent longitudinal acoustic phonons that may be capable of transporting phonons across hybrid interfaces free from scattering must be catalogued, potentially using the metrology strategies explored herein. Since the organic phase transitions characterized herein can be tuned to appear at a variety of temperatures with minimal effect on the optical properties of the perovskite layers, device design for thermal actuation or thermal energy storage is suggested.

Additionally, the surprisingly effective composite representation of these materials must be further probed. For instance, this dissertation focused exclusively on cross-plane thermal transport, wherein the interface resistances within the composite picture are in series and thus correspond to the lowest possible for a system exhibiting ballistic transport. These materials, however, are extremely anisotropic, as can be readily seen by their structure as multilayered sheets. Thus, in-plane transport may be well predicted using an analogous model wherein thermal transport is governed as though by resistors in parallel. As in electronic transport, such transport would correspond to the highest possible conductivity. An investigation into this behavior would allow engineers to recreate the well-known Wiener bounds on the conductivity tensor. Such insight would create a conductivity map that could be used to intelligently engineer future devices with far enhanced facility. Additionally, this investigation may well find that the ballistic transport that dominates transport in the cross-plane direction is not exhibited in the in-plane direction. Instead, in this direction the subphases may exhibit the anharmonic phonon-

phonon scattering pathways that limit their bulk conductivities so significantly. Such insight would also be exceedingly interesting, as this would serve to suggest that the dominant transport pathways are actually directionally-dependent, even though the observed anisotropy may not be terribly significant.

Science is by its very nature perpetually unfinished. It is the author's sincere hope that the intrepid reader that makes it this far has been inspired by some portion of this text, and engages in the pursuit of designing their own solutions to the problems that face our world, from the atoms up.

Appendix A

A.1 PbBr 2D LHP Synthesis

Crystals of bromide 2D LHPs were synthesized using a previously published cooling-induced crystallization method[1]. Briefly, a solution of $PbBr_2$ was prepared by dissolving PbO (99.9+%, (trace metal basis) <10 microns, powder, ACROS Organic) in concentrated aqueous HBr solution (ACS reagent, 48%, MilliporeSigma) under reflux at 130 °C for 15 minutes. The solution was then allowed to cool to room temperature before a small volume of organic spacer (alkaneamine, L) was added and a white precipitate of *n* = 1 L-PbBr formed. For the syntheses of *n* = 1 2D LHPs, this solution containing the white precipitate of *n* = 1 L-PbBr was heated on a hot plate set at 130 °C until clear. After that, the clear solution was allowed to cool slowly inside a thermos filled with hot sand at 110 °C to induce crystallization. After a day, crystals of bromide 2D LHPs were collected by suction filtration and dried under reduced pressure for at least 12 hours. For the syntheses of *n* = 2 and 3 2D LHPs, the solution containing the white precipitate of *n* = 1 L-PbBr was mixed with a solution of MABr in concentrated aqueous HBr before the final heating step.

A.2 Photoluminescence Measurements of Bromide 2D LHPs

In order to confirm that the crystals grown were indeed composed of periodic atomically thin layers of perovskite and organic molecular junctions, photoluminescence spectroscopy was utilized to confirm appropriate quantum confinement given the perovskite quantum well thickness via appearance of an excitonic emission peak (Figure A.1). For n=1 PbBr 2D LHPs, this peak is located at ~410 nm, whereas for n=2,3 PbBr 2D

LHPs the thicker perovskite layers correspond to weaker quantum confinement and excitonic emission at ~445 nm and ~465 nm, respectively. The inflated linewidth of the n=1 2D LHPs in Figure A.1b are likely due to reabsorption of the excitonic emission. The re-absorbed light is emitted at lower energies (higher wavelengths), leading to the broader observed linewidth of the 2D LHPs. This is facilitated by the very small Stokes shift in n=1 2D LHPs and has been reported on elsewhere.[2]

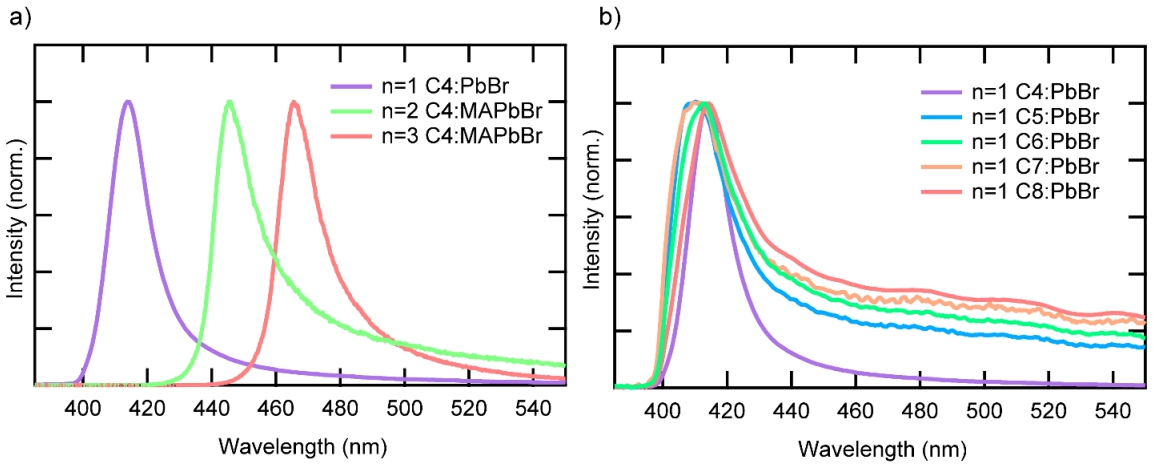

Figure A.1. Summary of representative PL for PbBr 2D LHPs. a) PL for 2D LHPs at various inorganic sheet (octahedral layer) thicknesses. b) PL for n= 1 2D LHPs with various chain length organic spacer subphases (Cx alkylammonium spacer ions).

Photoluminescence spectra of bromide 2D LHPs were collected by a home-built photoluminescence set up. The output of a 365 nm fiber-coupled LED (Thorlabs, M365FP1) was used as an excitation source and was cleaned by a 390 nm short-pass filter (Semrock, FF01-390/SP-25) before exciting a sample. The emission from a sample was filtered by a 400 nm long-pass filter (Thorlabs, FEL0400) to remove any residual excitation light before being measured by a fiber-coupled spectrometer (Avantes, AvaSpec-ULS2048XL).

A.3 Powder X-Ray Diffraction Measurements of PbBr 2D LHPs

The long-range order present in the crystals, as well as the retention of the perovskite unit cell within the inorganic sublayer was confirmed with powder X-ray diffraction. These results are readily compared with those corresponding to solved crystal structures of other Ruddlesden-Popper 2D LHPs in the literature, confirming synthesis of pure material and allowing for analysis of structural parameters such as the material density and the organic/inorganic period thicknesses, both of which are readily obtained from analysis of a proposed crystal structure.[1,3,4] Representative powder XRD patterns are shown below in Figure A.2.

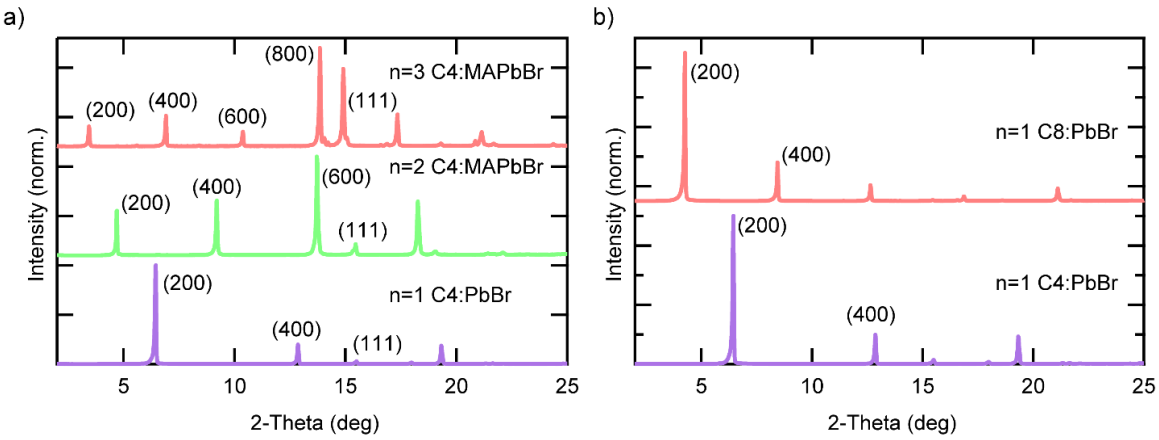

Figure A.2. Powder X-ray diffraction for structural confirmation. a) Powder XRD for n=1-3 C4:MAPbBr 2D LHPs showing structural confirmation between our materials and those established elsewhere.[1,4] b) Representative powder XRD for n=1 PbBr 2D LHPs with varying organic spacer length, showing structural similarity between our materials and those established elsewhere[1,3]. The consistent decrease in 2-theta for a given peak as a function of increasing spacer length corresponds to the increasing periodicity of the multilayer. The lack of pronounced shift in inorganic (non (h00) planes) suggests the inorganic sublattice is unchanged and well approximated by the bulk unit cell.

Powder X-ray diffraction data was taken using a PANalytical X'Pert Pro MPD X-ray diffractometer (Cu Kα radiation, λ = 1.54184 Å) with High-Speed Bragg-Brentano Optics. A

0.04 rad soller slit, a 1° anti-scatter slit, a 10 mm mask and a programmable divergence slit with an illuminated length of 6 mm were used in the incident beam path. The diffracted beam optics included a 0.04 rad soller slit, a Ni Filter and an automatic receiving slit. The detector was an ultrafast X'Celerator RTMS detector. The angular step in 2θ was 0.04°.

A.4 FDTR Data Fitting and Parameter Extraction for PbBr 2D LHPs

For consistency with previously reported material thermal conductivities, we utilize the same heat transfer model for analysis posed originally by Cahill, and used ubiquitously since then with respect to FDTR measurements of effective thermal conductivities[5–8]. Many other models have been posed as potentially superior in directly capturing nonequilibrium transport behavior evident in FDTR experiments without the use of an effective thermal conductivity, but such models typically apply to much higher heating frequencies and with respect to far more conductive samples, and so fall outside the scope of this particular report.[9,10] In order to extract an effective thermal conductivity of a macroscopic solid such as a 2D lead halide perovskite crystal, Fourier's law and thus the Cahill model remain sufficient. This model was fit to the experimentally measured phase response (phase lag vs. frequency) using a nonlinear least squares Levenberg-Marquardt algorithm. During fitting, the laser spot size was allowed to vary within experimental error and the thermal conductivity was allowed to vary by an order of magnitude from an initial guess. The uncertainty of the measurement was determined by evaluating the absolute change in measured thermal conductivity for the maximum variance of the spot size within the resolution of the CCD. Typical uncertainties are ~ 10 %, in line with other FDTR measurements previously reported.[11,12] Several representative measurements/fits are shown below in Figures A.3.

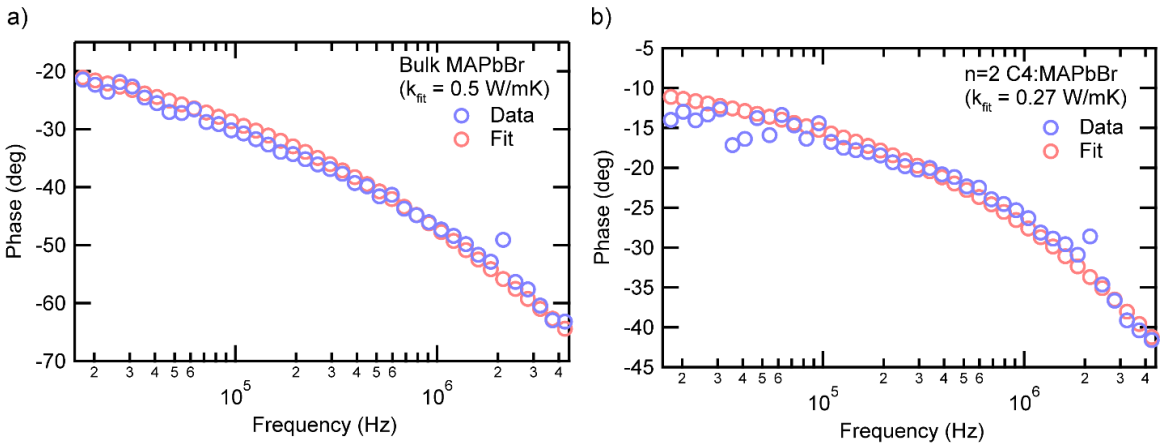

Figure A.3. Representative data and numerical fits for a single crystal of bulk MAPbBr and a 2D LHP crystal. The value for thermal conductivity of bulk MAPbBr is in excellent agreement with those previously reported.[12]

A.5 Measurement of Relevant System Parameters

Since an FDTR measurement is sensitive to a variety of system parameters and materials properties, it is important to separately measure all of these parameters except for the parameter of interest, the sample thermal conductivity. The spot size is measured as described in Ch. 3. For the transducer thickness/properties, the following approach was used.

The thermal conductivity and volumetric heat capacity of the Au transducer were 314 W/mK and 2500 kJ/m^3, as reported elsewhere.[11,12] To measure the thickness of the gold transducer, stylus profilometry was used. First, a reference gold-coated glass film from the same deposition as the samples of interest was scratched using a razor. Then, a Bruker DXT stylus profilometer was used to measure the thickness of the film via a line-scan across this scratch. A representative line-scan is shown in Figure A.4.

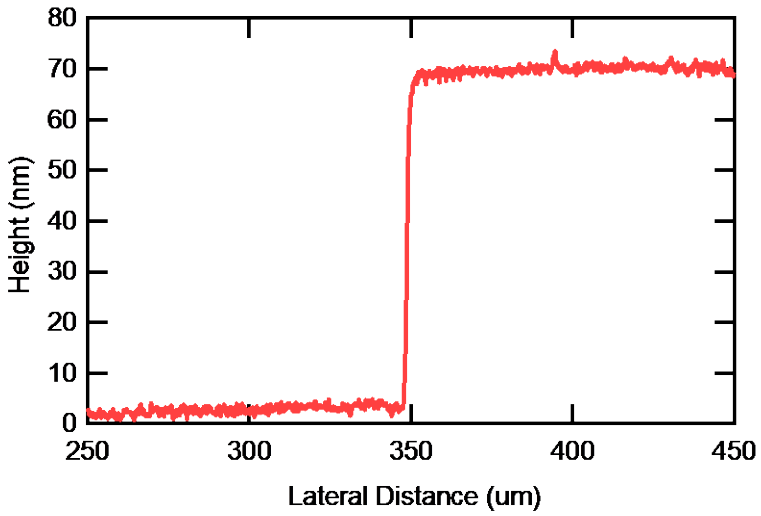

Figure A.4. A representative profilometry line-scan used to measure the film thickness of a transducer film. The thickness of this Au film was measured to be 67 ±1 nm. Typical films range from 60-150 nm depending on the deposition settings used.

A.6 Estimation of the Mass Density of 2D LHPs

Although differential scanning calorimetry measurements provide reliable measurements of the specific heat capacity, the heat transfer model for FDTR requires knowledge of the volumetric heat capacity (product of the specific heat capacity and the mass density) of a sample. For 2D LHPs, since the generic crystal structure is fairly well established this is simple to estimate even when the precise structural solution is not available. Within the inorganic (perovskite) subphase, the bond lengths and angles are well approximated by that of the pseudocubic bulk unit cell. Thus, the density within this layer is effectively that of the bulk MAPbBr perovskite. This is the case even for n=1 perovskites without a proper methylammonium cation as the spacer binding group is still an ammonium ion. This estimation is consistent with the assumption that the structure/vibrational spectrum of the inorganic subphase is unchanged from that established for bulk MAPbBr. Within the

organic subphase, the period thickness is easily extracted by subtracting the periodicity as determined via x-ray diffraction measurements by the inorganic subphase thickness. As has been established elsewhere, these thicknesses are consistent across 2D LHPs with different compositions of the inorganic subphase.[1,3] As a result, we can confirm our measurement of the organic subphase with those made for n=1 PbI 2D LHPs precisely measured via single-crystal XRD previously by Billing et al.[13,14]. Knowing the cubic unit cell of the inorganic subphase, octahedral layer thickness, and organic subphase period thickness, the orthorhombic unit cell of PbBr 2D LHPs is readily approximated. Dividing the molecular weight of the 2D LHP as expected from its chemical formula from the volume of this unit cell then directly approximates the mass density of the perovskite. Figure A.5 below lists the results of these estimates for the PbBr 2D LHPs studied herein.

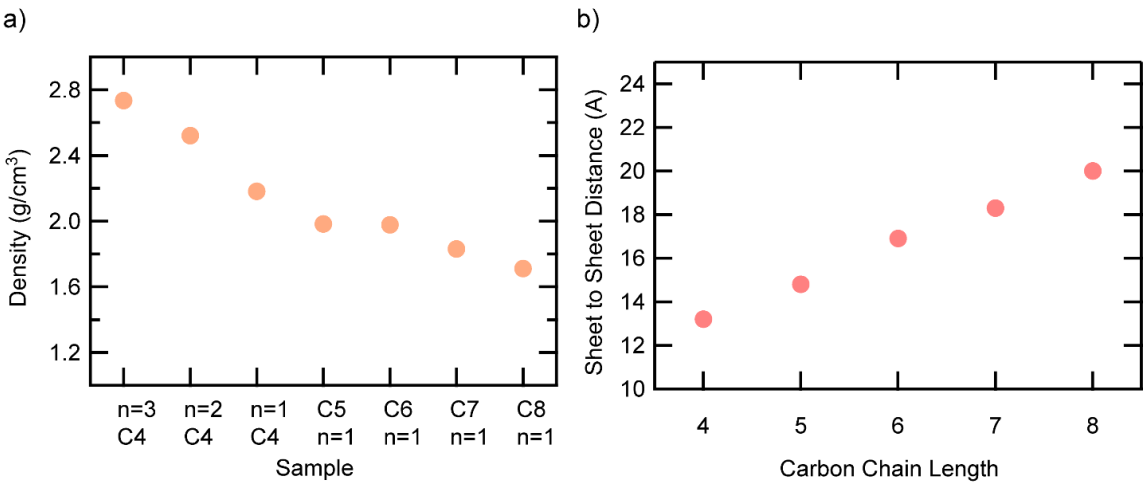

Figure A.5. a) Estimated mass density of PbBr 2D LHPs b) PbBr 2D LHP periodicities

A.7 Parameters Used for Composite Models

In order to determine the thermal conductivity of the PbBr 2D LHPs using the models proposed in the main text, several materials parameters need to be known. Specifically, the period thicknesses, component heat capacities, and component sound velocities are the necessary inputs. The first of these is measured/estimated using XRD as described in the previous section. The heat capacity and sound speed of bulk MAPbBr perovskite (380 J/kgK and 1717 m/s) as measured elsewhere and herein was used for the inorganic subphase.[15] The heat capacity of bulk alkanes were used to approximate the heat capacity within the organic subphase, a reasonable assumption because the organic molecules are known to exhibit significant dynamic disorder (liquid-like motions) at measurement temperatures and have densities comparable to their bulk liquid counterparts.[1,4] The sound speed for ballistic phonon transport across the molecular junctions that comprise the organic subphase has been studied extensively for surface-bound alkyl chains, in systems such as self-assembled monolayers and semiconductor nanocrystals.[16–18] Across all of these measurements, the values for the sound velocity of such phonons are consistent and show essentially linearly proportional sound velocity with increasing alkyl chain length. We use a linear interpolation of the measurements made by Li et al. as an input for calculation of the sound velocity within the organic subphase.[16]

A.8 References

(1) Paritmongkol, W.; Dahod, N. S.; Mao, N.; Zheng, S.-L.; Tisdale, W. A. Synthetic Variation and Structural Trends in Layered Two-Dimensional Alkylammonium Lead Halide Perovskites. *Chemrxiv* 2019. https://doi.org/10.26434/chemrxiv.7942628.

(2) Gong, X.; Voznyy, O.; Jain, A.; Liu, W.; Sabatini, R.; Piontkowski, Z.; Walters, G.; Bappi, G.; Nokhrin, S.; Bushuyev, O.; Yuan, M.; Comin, R.; McCamant, D.; Kelley, S. O.; Sargent, E. H. Electron–phonon Interaction in Efficient Perovskite Blue Emitters. *Nat. Mater.* 2018, *17* (6), 550–556. https://doi.org/10.1038/s41563-018-0081-x.

(3) Weidman, M. C.; Seitz, M.; Stranks, S. D.; Tisdale, W. A. Highly Tunable Colloidal Perovskite Nanoplatelets through Variable Cation, Metal, and Halide Composition. *ACS Nano* 2016, *10* (8), 7830–7839. https://doi.org/10.1021/acsnano.6b03496.

(4) Stoumpos, C. C.; Cao, D. H.; Clark, D. J.; Young, J.; Rondinelli, J. M.; Jang, J. I.; Hupp, J. T.; Kanatzidis, M. G. Ruddlesden-Popper Hybrid Lead Iodide Perovskite 2D Homologous Semiconductors. *Chem. Mater.* 2016, *28* (8), 2852–2867. https://doi.org/10.1021/acs.chemmater.6b00847.

(5) Cahill, D. G. Analysis of Heat Flow in Layered Structures for Time-Domain Thermoreflectance. *Rev. Sci. Instrum.* 2004, *75* (12), 5119–5122. https://doi.org/10.1063/1.1819431.

(6) Schmidt, A. J.; Chen, X.; Chen, G. Pulse Accumulation, Radial Heat Conduction, and Anisotropic Thermal Conductivity in Pump-Probe Transient Thermoreflectance. *Rev. Sci. Instrum.* 2008, *79* (11), 114902. https://doi.org/10.1063/1.3006335.

(7) Yang, J.; Maragliano, C.; Schmidt, A. J. Thermal Property Microscopy with Frequency Domain Thermoreflectance. *Rev. Sci. Instrum.* 2013, *84* (May 2015). https://doi.org/10.1063/1.4824143.

(8) Schmidt, A. J.; Cheaito, R.; Chiesa, M. A Frequency-Domain Thermoreflectance Method for the Characterization of Thermal Properties. *Rev. Sci. Instrum.* 2009, *80*, 3–8. https://doi.org/10.1063/1.3212673.

(9) Wilson, R. B.; Cahill, D. G. Anisotropic Failure of Fourier Theory in Time-Domain Thermoreflectance Experiments. *Nat. Commun.* 2014, *5*, 5075. https://doi.org/10.1038/ncomms6075.

(10) Regner, K. T.; McGaughey, a. J. H.; Malen, J. a. Analytical Interpretation of Nondiffusive Phonon Transport in Thermoreflectance Thermal Conductivity Measurements. *Phys. Rev. B* 2014, *90*, 064302. https://doi.org/10.1103/PhysRevB.90.064302.

(11) Ong, W.; Rupich, S. M.; Talapin, D. V; McGaughey, A. J. H.; Malen, J. a. Surface Chemistry Mediates Thermal Transport in Three-Dimensional Nanocrystal Arrays. *Nat. Mater.* 2013, *12* (5), 410–415. https://doi.org/10.1038/nmat3596.

(12) Elbaz, G. A.; Ong, W.-L.; Doud, E. A.; Kim, P.; Paley, D. W.; Roy, X.; Malen, J. A. Phonon Speed, Not Scattering, Differentiates Thermal Transport in Lead Halide Perovskites. *Nano Lett.* 2017, *17* (9), 5734–5739. https://doi.org/10.1021/acs.nanolett.7b02696.

(13) Billing, D. G.; Lemmerer, A. Synthesis, Characterization and Phase Transitions in the Inorganic–organic Layered Perovskite-Type Hybrids [(CnH2n+1NH3)2PbI4], n = 4, 5 and 6. *Acta Crystallogr. Sect. B Struct. Sci.* 2007, *63* (5), 735–747. https://doi.org/10.1107/S0108768107031758.

(14) Billing, D. G.; Lemmerer, A. Synthesis, Characterization and Phase Transitions of the Inorganic-Organic Layered Perovskite-Type Hybrids [(CnH2n+1NH 3)2PbI4] (n = 12, 14, 16 and 18). *New J. Chem.* 2008, *32* (10), 1736–1746. https://doi.org/10.1039/b805417g.

(15) Knop, O.; Wasylishen, R. E.; White, M. A.; Cameron, T. S.; Oort, M. J. M. Van. Alkylammonium Lead Halides. Part 2. CH 3 NH 3 PbX 3 (X = Cl, Br, I) Perovskites: Cuboctahedral Halide Cages with Isotropic Cation Reorientation. *Can. J. Chem.* 1990, *68* (3), 412–422. https://doi.org/10.1139/v90-063.

(16) Lee, E. M. Y.; Mork, A. J.; Willard, A. P.; Tisdale, W. A. Including Surface Ligand Effects in Continuum Elastic Models of Nanocrystal Vibrations. *J. Chem. Phys.* 2017, *147* (4), 044711. https://doi.org/10.1063/1.4995439.

(17) Wang, Z.; Carter, J. A.; Lagutchev, A.; Koh, Y. K.; Seong, N.-H.; Cahill, D. G.; Dlott, D. D. Ultrafast Flash Thermal Conductance of Molecular Chains. *Science.* 2007, *317* (5839), 787–790. https://doi.org/10.1126/science.1145220.

(18) DelRio, F. W.; Jaye, C.; Fischer, D. A.; Cook, R. F. Elastic and Adhesive Properties of Alkanethiol Self-Assembled Monolayers on Gold. *Appl. Phys. Lett.* 2009, *94* (13), 131909. https://doi.org/10.1063/1.3111440.

List of Publications

1. Nabeel S. Dahod, Watcharaphol Paritmongkol, William A. Tisdale. "The Role of Diffuse Interfacial Phonon Scattering in Thermal Transport for Layered Two-Dimensional Lead Bromide Perovskites" *In Preparation*

2. Nabeel S. Dahod, Arthur France-Lanord, Watcharaphol Paritmongkol, Jeffrey C. Grossman, William A. Tisdale. "On The Low Frequency Raman Spectrum of Layered Two-Dimensional Lead-Iodide Perovskites" *In Preparation*

3. Nabeel S. Dahod, Watcharaphol Paritmongkol, Alexia Stollmann, Charles Settens, Shao-Liang Zheng, William A. Tisdale. "Melting Transitions of the Organic Subphase in Layered Two-Dimensional Halide Perovskites" *In Preparation*

4. Watcharaphol Paritmongkol, Nabeel S. Dahod, Nannan Mao, Shao-Liang Zheng, William A. Tisdale. "Synthetic Variation and Structural Trends in Layered Two-Dimensional Alkylammonium Lead Halide Perovskites" *In Preparation*

5. Rachel H. Gilmore, Yun Liu, Wenbi Shcherbakov-Wu, Nabeel S. Dahod, Elizabeth M.Y. Lee, Mark C. Weidman, Huashan Li, Joel Jean, Vladimir Bulovic, Adam P. Willard, Jeffrey C. Grossman, William A. Tisdale. "Epitaxial Dimers and Carrier De-Trapping Kinetics in PbS Quantum Dot Solids" *ChemArxiv* (2019)

6. Aaron J. Goodman, Nabeel S. Dahod, and William A. Tisdale. "Ultrafast Charge Transfer at a Quantum Dot/2D Materials Interface Probed by Second Harmonic Generation" *The Journal of Physical Chemistry Letters* (2018).

7. Jacob T. Held, Katharine I. Hunter, Nabeel S. Dahod, Benjamin L. Greenberg, Danielle Reifsnyder Hickey, William A. Tisdale, Uwe R. Kortshagen, K. Andre Mkhoyan. "Obtaining structural parameters from STEM-EDX maps of core/shell nanocrystals for optoelectronics" *ACS Applied Nano Materials* (2018).

8. Jolene Mork, Elizabeth M.Y. Lee, Nabeel S. Dahod, Adam P. Willard, William A. Tisdale. "Modulation of low-frequency acoustic vibrations in semiconductor nanocrystals through choice of surface ligand" *The Journal of Physical Chemistry Letters* (2016).

9. Daniel N. Congreve, Mark C. Weidman, Michael Seitz, Watcharaphol Paritmongkol, Nabeel S. Dahod, William A. Tisdale. "Tunable light-emitting diodes utilizing quantum-confined layered perovskite emitters" ACS Photonics (2017).